Effects of the Nab Spectrometer on the Measurement of the Electron-Antineutrino Correlation Parameter *a*

A Dissertation Presented for the

Doctor of Philosophy

Degree

The University of Tennessee, Knoxville

Elizabeth Mae Scott

May 2020

To my dad, the Kirk to my Scotty.

Acknowledgements

This work would not be possible without the community of people who have helped me throughout my time in graduate school. Thanks to Rick Huffstetler, Joshua Bell, and Alvin Peak II for all of the machining and quick turn-arounds. Thanks to Gary Hamm, Dan Varnell, Scott Helus, and Doug Bruce for lending me both of the laser trackers and providing all the metrology support I could want. Thank you to Nadia Fomin for being a wonderful mentor and support network. Thank you to Geoff Greene for being the kind of advisor that I hope to be some day- a supportive and engaging teacher who always pushes me to be a better communicator and to have fun with my work. Thank you to my friends for reminding me to enjoy my life. Thank you to my family for encouraging me since the day I first wondered how the universe worked. And finally, thank you to my soon-to-be husband, Ramil. You are my universal constant.

Life, with its rules, its obligations, and its freedoms, is like a sonnet: You're given the form, but you have to write the sonnet yourself. What you say is completely up to you.

- Madeline L'Engle, A Wrinkle in Time

Abstract

The Nab experiment aims to measure the neutron beta decay electron-neutrino correlation coefficient a and the Fierz interference term b. Measurement of a to a relative uncertainty of 10^{-3} provides a determination of λ, the ratio of axial to vector coupling constant, at roughly the same precision level as the vector coupling determined from the superallowed decays. A measurement of b with an uncertainty of 3×10^{-3} would provide a sensitive test of physics beyond the Standard Model. In Nab, the parameter a is extracted from the electron energy and proton time of flight (TOF) using an asymmetric magnetic spectrometer and two large-area highly pixelated Si detectors. To reach the goal of 10^{-3} relative uncertainty in a, Nab requires a detailed understanding of its possible systematic effects. The proton momentum is measured via time of flight (TOF), triggered by the detection of an electron and the largest systematic uncertainty comes from the proton path length in the magnetic field. The TOF only measures the momentum along the field lines; cyclotron motion perpendicular of the proton is not directly observable. The spectrometer field is designed to adiabatically align the proton momentum along the field lines, such that this uncertainty is limited to 10^{-4}. However, correcting for the path length requires a detailed mapping and analytic expansion of the magnetic field. My research focuses on the design, construction, and application of

the mapping system, fitting the field data using Modified Bessel Function expansion, and using said expansion to create a numerically calculated spectrometer response function for an independent extraction of a.

Contents

List of Tables

List of Figures

Chapter 1

An Introduction to Neutron Beta Decay

1.1 The Discovery of the Neutron and its Decay

The existence of the neutron was first posited by Ernest Rutherford during his Bakerian lecture for the Royal Society in 1920. [41]. The difference in atomic mass and atomic number for nuclei suggested that some heavy, electrically neutral particle was bound within the nucleus. Rutherford suggested that this particle might be a tightly bound electron and proton. In 1930, Walther Bothe and Herbert Becker found that light elements such as beryllium (Be), boron (B), fluorine (F) and lithium (Li), bombarded by energetic alpha particles, would produce a neutral, penetrating radiation. In early 1932, Iréne and Frédéric Joliot-Curie found that this radiation incident on a hydrogen rich material emitted protons. Though Curie and Bothe thought this was gamma radiation, James Chadwick repeated the experiment with a detailed analysis of the energy and momentum conservation and determined that the interaction could only be explained via a heavy neutral particle, the neutron, with a mass between 1.005 and 1.008 atomic mass units. Thus, the neutron was "discovered" in 1932, and had its first mass determination in 1934 by Chadwick and Maurice Goldhaber [7]. Significantly, this mass was greater than the sum of the electron and proton masses, indicating that it was energetically possible for a neutron to decay into an electron and a proton.

Concurrently, the continuous beta spectrum observed from radioactive decay proved troublesome. Gamma and α decay emitted discrete energy radiation, and the continuous spectrum suggested a violation of energy conservation. In 1930, Pauli suggested a solution in which a third particle was present in the decay [37]. A more precise measurement of the neutron mass in 1935 confirmed that it was greater than the proton plus electron mass, thereby rejecting the model of a bound electron and proton [8].

In 1934, Enrico Fermi published his theory of β decay, which was the first attempt at describing the weak nuclear interaction. His four fermion interaction was analogous to the theory of the emission of light quanta from excited nuclei, and treated as a purely vector current [58, 39].

$$\mathscr{L}_E = eJ^E_\mu A^\mu = e(\bar{u}_p \gamma_\mu u_p)A^\mu \rightarrow \mathscr{L}_{Fermi} = G_F(\bar{u}_p \gamma_\mu u_n)(\bar{u}_e \gamma^\mu u_\nu) \tag{1.1}$$

This model of weak interactions dominated until the discovery of parity violation by Lee and Yang [28].

Even with Fermi's theory of β decay, the first observation of neutron beta decay did not occur until the 1940s, when the Graphite Reactor was built at the Oak Ridge National Lab

O_i	Type of Transformation	Parity
$O_S = 1$	Scalar	Even
$O_V = \gamma_\mu$	Vector	Odd
$O_T = \sigma_{\mu\nu} \equiv \frac{i}{2}(\gamma_\mu\gamma_\nu - \gamma_\nu\gamma_\mu)$	Tensor	Odd
$O_A = \gamma_5\gamma_\mu$	Axial-Vector	Even
$O_P = \gamma_5$	Pseudoscalar	Odd

Table 1.1: Dirac Bilinear Covariant Fields

in Oak Ridge, Tennessee with the purpose of producing plutonium. A side benefit of the reactor was the high flux of neutrons. It was on a beam of these neutrons that Arthur Snell first observed free neutron decay [46]. At about the same time, John Robson independently observed neutron decay at the NRX reactor in Chalk River, Canada. Since Snell's observation could only estimate the neutron lifetime due to detector efficiency uncertainties, Robson's lifetime measurement is considered the first measurement of the neutron lifetime [40, 54].

1.2 Building to Neutron Decay with V-A Theory

The pure vector current description of the weak interaction was soon generalized to include the scalar (S), pseudoscalar (P), tensor (T), vector (V), and axial-vector (A) interactions, all of which are covariant under Lorentz transformations. The generalized Hamiltonian is written as

$$H_{int} = \sum_i \frac{G_i}{2}(\bar{u}_p O_i u_n)(\bar{u}_e O^i u_\nu) + \text{Hermitian Conjugate} \tag{1.2}$$

where the O_i represents the bilinear covariant fields as seen in Table 1.1 and G_i is the interaction strength. These cover all first order interactions available for a weak transition.

After generalizing the weak interaction into these terms, restrictions could be applied from observed nuclear decays. Two types of decays had been observed thus far; Fermi transitions, $\Delta J = 0$, allowed by scalar and vector currents, and Gamow-Teller transitions, $\Delta J = 1$, allowed by tensor and axial-vector currents. In the non-relativistic limit, appropriate for the nucleons, pseudoscalar terms vanished. The existence of both decays suggested that the weak interaction consisted of one V or S term and one T or A term. Significantly, both Fermi and Gamow-Teller transitions preserved parity.

In 1956, Lee and Yang proposed that parity was not conserved in weak interactions. This was confirmed by the Wu experiment, wherein the beta emission of the ^{60}Co Gamow-Teller transition to ^{60}Ni showed dependence on nuclear polarization, violating parity. This immediately suggested that the form of the weak interaction Hamiltonian was incorrect; since it consisted of a product of bilinear covariant fields, the total Hamiltonian would be a scalar, and thus symmetric under parity. To compensate for this, a pseudoscalar term was added, as it is parity odd, as seen in Equation 1.3 and Equation 1.4.

$$(\bar{u}_p O_i u_n)(\bar{u}_e O^i u_\nu) + (\bar{u}_p O_i u_n)(\bar{u}_e O^i C_i \gamma_5 u_\nu) = (\bar{u}_p O_i u_n)(\bar{u}_e O^i (1 + C_i \gamma_5) u_\nu) \tag{1.3}$$

$$H_{int} = \sum_i \frac{G_i}{2} (\bar{u}_p O_i u_n)(\bar{u}_e O^i (1 + C_i \gamma_5) u_\nu) + \text{Hermitian Conjugate} \tag{1.4}$$

The final piece came from an analysis of the neutrino spinors. The bilinear covariant fields arise from the Dirac equation (Equation 1.5) and suggested solutions in terms of Dirac spinors.

$$(i\gamma^{\mu}\partial_{\mu} - m)\psi = 0 \tag{1.5}$$

An important feature of Dirac spinors is the behavior of the four components. For massive particles in the nonrelativistic limit, wherein $p << m, E$, the four component spinor reduces to two components, such as in Equation 1.6 for a spin up particle with momentum $\vec{p} = (p_x, p_y, p_z)$. In solutions for massive particles, positive energy solutions reduce to the first two components, while negative energy solutions reduce to the final two components.

$$u = \begin{pmatrix} \sqrt{E+m} \\ 0 \\ p_z/\sqrt{E+m} \\ (p_x + ip_y)/\sqrt{E+m} \end{pmatrix} \tag{1.6}$$

In contrast, the relativistic neutrinos retain all four components. However, it can be shown that the zero mass of the neutrino decouples the upper and lower spinor solutions, with the upper being purely right handed and the lower being purely left handed.

$$P_R = \frac{1+\gamma_5}{2}, \quad P_L = \frac{1-\gamma_5}{2} \tag{1.7}$$

Additionally, the projection operators in Equation 1.7 extract the left handed and right handed components of the spinor. An experiment showing that electrons were left-handed, [16], then led to the conclusion that if the neutrino were left-handed, the weak interaction consisted of V and A currents, and if it were right-handed, it consisted of S and T currents.

After the left-handedness of the neutrino was shown, [17], the Hamiltonian for the hadronic weak interaction could be written in the V-A form, as follows:

$$H_w = \frac{G_V}{2}[\bar{u}_p \gamma_\mu u_n][\bar{u}_e \gamma^\mu (1-\gamma_5) u_\nu] + \frac{G_A}{2}[\bar{u}_p \gamma_5 u_n][\bar{u}_e \gamma^\mu (1-\gamma_5) u_\nu] + \text{H.C.} \tag{1.8}$$

$$H_w = \frac{1}{\sqrt{2}}[\bar{u}_p \gamma_\mu (G_V - G_A \gamma_5) u_n][\bar{u}_e \gamma^\mu (1-\gamma_5) u_\nu] + \text{H.C.} \tag{1.9}$$

where the H.C. terms are the hermitian conjugates.

Since neutron beta decay is a semi-leptonic interaction and party to effects from spectator quarks, the coupling constants G_V and G_A can be rewritten in terms of $\lambda = \frac{G_A}{G_V}$, G_F (the Fermi constant), and V_{ud}, the element of the Cabibbo-Kobayashi-Maskawa quark mixing matrix responsible for up-down quark mixing.

$$H_w = \frac{G_F V_{ud}}{\sqrt{2}}[\bar{u}_p \gamma_\mu (1 - \lambda \gamma_5) u_n][\bar{u}_e \gamma^\mu (1-\gamma_5) u_\nu] + \text{H.C.} \tag{1.10}$$

1.3 Testing the Standard Model via Neutron Beta Decay

Assuming a V-A form for the weak interaction, one can use observations of weak decays to measure the strength of the vector and axial-vector currents, G_A and G_V. In semi-leptonic and hadronic weak interactions, such as Equation 1.10, the presence of spectator quarks gives access to V_{ud}, an element of the Cabibbo-Kobayashi-Maskawa (CKM) matrix, Equation 1.11. This matrix describes the 3 generation flavor mixing of quark states when moving between the mass and weak eigenstates and the matrix is unitary within the Standard Model due to weak universality. These matrix elements are not calculable and must be experimentally measured [3].

$$\begin{pmatrix} d' \\ s' \\ b' \end{pmatrix} = \begin{pmatrix} V_{ud} & V_{us} & V_{ub} \\ V_{cd} & V_{cs} & V_{cb} \\ V_{td} & V_{ts} & V_{tb} \end{pmatrix} \begin{pmatrix} d \\ s \\ b \end{pmatrix} \tag{1.11}$$

Due to the unitarity requirement, the CKM matrix provides a way to test for beyond the Standard Model (BSM) physics. If precise measurements of the matrix elements break unitarity, it could be due to non V-A interactions or a violation of universality. One such test of unitarity is square of sums of the top row, which with current matrix element values is

$$\Delta = 1 - |V_{ud}|^2 - |V_{us}|^2 - |V_{ub}|^2 = (32 \pm 14) \times 10^{-4} \tag{1.12}$$

$$d' \approx V_{ud} d \tag{1.13}$$

The element V_{ud} has the highest contribution to unitarity, therefore improving its experimental uncertainty is a straightforward test for BSM physics.

1.3.1 V_{ud} from Superallowed Decay

Currently, the highest precision for V_{ud} comes from the measurement of superallowed nuclear decays. These decays are purely vector transitions, wherein a nucleus decays between nuclear analog states of spin parity and isospin ($J^\pi = 0^+$ and $T = 0$). The strength of these transitions can be calculated from the ft values, which can be found from the transition energy, Q_{EC}, the half-life $t_{1/2}$, and the branching ratio, R. This transition strength is inversely proportional to the square of the Fermi matrix element of the transition.

$$f_L(Z', Q)t_{1/2} = \frac{log_e(2)2\pi^3 h^7}{g^2 m_e^5 c^4 |M_{if}^L|^2} \tag{1.14}$$

Including the radiative corrections, this transition strength can be written as

$$\mathscr{F}t \equiv ft(1+\delta'_R)(1+\delta_{NS}-\delta_C) = \frac{K}{2G_V^2(1+\Delta_R^V)} \tag{1.15}$$

where δ'_R, δ_{NS} and δ_C are transition dependent radiative corrections. The constants are combined into $K = 8120.2776(9) \times 10^{-10} GeV^{-4} s$ and Δ_R^V is the transition-independent part of the radiative corrections. The vector coupling strength G_V is extracted from these measurements, and then the up-down quark mixing matrix can be found from $V_{ud} = G_V/G_F$, where G_F is known from leptonic muon decay [21].

1.3.2 V_{ud} from Neutron Beta decay

To extract V_{ud} from neutron beta decay, consider again Equation 1.10. Using Fermi's golden rule, the neutron decay rate can be calculated as

$$\Gamma = \frac{1}{\tau_n} = \frac{f^R m_e^5 c^4}{2\pi^3 \hbar^7}\left(|G_V|^2 + 3|G_A|^2\right) = \frac{f^R m_e^5 c^4}{2\pi^3 \hbar^7}|V_{ud}|^2 G_F^2\left(1+3|\lambda|^2\right) \tag{1.16}$$

where Γ is the neutron decay rate, τ_n is the neutron lifetime, f_R is a phase space term corrected for the Fermi function, m_e is the mass of the electron, V_{ud} is the Cabibbo-Kobayashi-Maskawa matrix element for up-down quark mixing, G_F is the Fermi constant, and λ is the ratio of the axial-vector to vector coupling constants. V_{ud} can be calculated by measuring λ and the lifetime, τ_n, for neutron beta decay.

To measure λ, a more phenomenological description of the triple differential decay rate is used. This is given by a parametrization in terms of the electron and anti-neutrino product energies as seen in Equation 1.17. This was initially shown by J.D. Jackson in his paper, *Possible Tests of Time Reversal Invariance in Beta Decay.* [24]

$$\frac{dw}{dE_e d\Omega_e d\Omega_\nu} \propto p_e E_e (E_0 - E_e)^2 \left[1 + a\frac{\overrightarrow{p_e} \cdot \overrightarrow{p_\nu}}{E_e E_\nu} + b\frac{m_e}{E_e} + \langle \overrightarrow{\sigma_n} \rangle \cdot \left(A\frac{\overrightarrow{p_e}}{E_e} + B\frac{\overrightarrow{p_\nu}}{E_\nu} + ... \right) \right] \tag{1.17}$$

In this expansion, the parameters, a, b, A, B, etc., are called correlation coefficients and $\langle \overrightarrow{\sigma_n} \rangle$ is the average neutron polarization. These can be experimentally measured by observing neutron decay and measuring the daughter product energies and momenta. The derivation of this parametrization additionally gives relationships between the correlation coefficients and λ, providing an avenue for experimental testing of the Standard Model using neutron beta decay.

$$a = \frac{1 - |\lambda|^2}{1 + 3|\lambda|^2}, \quad A = -2\frac{|\lambda|^2 + |\lambda|}{1 + 3|\lambda|^2}, \quad B = 2\frac{|\lambda|^2 - |\lambda|}{1 + 3|\lambda|^2} \tag{1.18}$$

Equation 1.18 demonstrates the connection between a phenomenological measurement and the ratio of vector and axial vector coupling strengths. Equation 1.19 indicates that a and A are the most sensitive of these coupling constants for a $\lambda \approx 1.27$.

$$\frac{\partial a}{\partial \lambda} = \frac{-8\lambda}{(1+3\lambda^2)^2} \approx 0.30 \quad \frac{\partial A}{\partial \lambda} = 2\frac{(\lambda-1)(3\lambda+1)}{(1+3\lambda^2)^2} \approx 0.37 \quad \frac{\partial B}{\partial \lambda} = 2\frac{(\lambda+1)(3\lambda-1)}{(1+3\lambda^2)^2} \approx 0.076 \tag{1.19}$$

The advantage of using neutron beta decay is that it is free of nuclear corrections. As can be seen in Figure 1.2, the main sources of uncertainty for superallowed decays are the radiative corrections. For neutron decay, the experimental uncertainty is the largest source. If the experimental uncertainty of neutron beta decay experiments were reduced, they would become competitive with the superallowed decays. As a note, though pion beta decays have the lowest theoretical uncertainties and would also be competitive if the experimental uncertainty were reduced, the majority of the systematics come from the small branching ratio ($\approx 10^{-8}$) of the pion beta decay, which has yet to be precisely determined.

1.3.3 Current status of V_{ud}

There is currently a great deal of tension between the various methods of determining V_{ud}. To start, the highest precision measurement of λ comes from the spin-electron asymmetry, A, described as

$$\Gamma \propto 1 + \beta P A \cos\theta \tag{1.20}$$

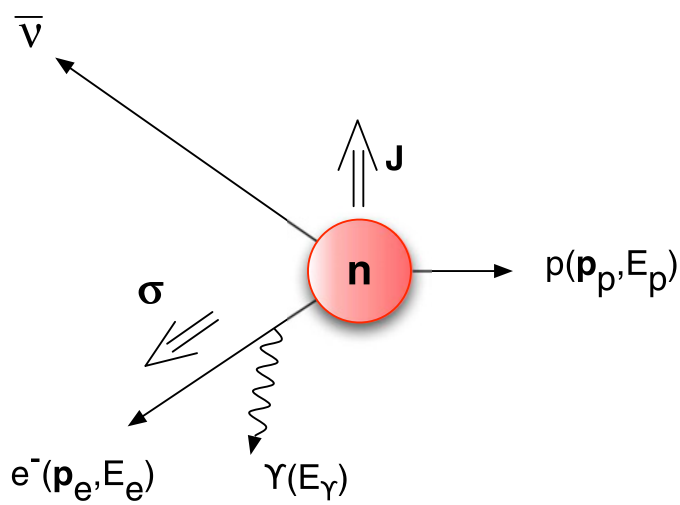

Figure 1.1: A graphic that displays the observables present in neutron beta decay [36]. Though the emitted electron does have a spin, it is difficult to detect. Similarly, the γ from radiative decay is not often high enough energy to be detected.

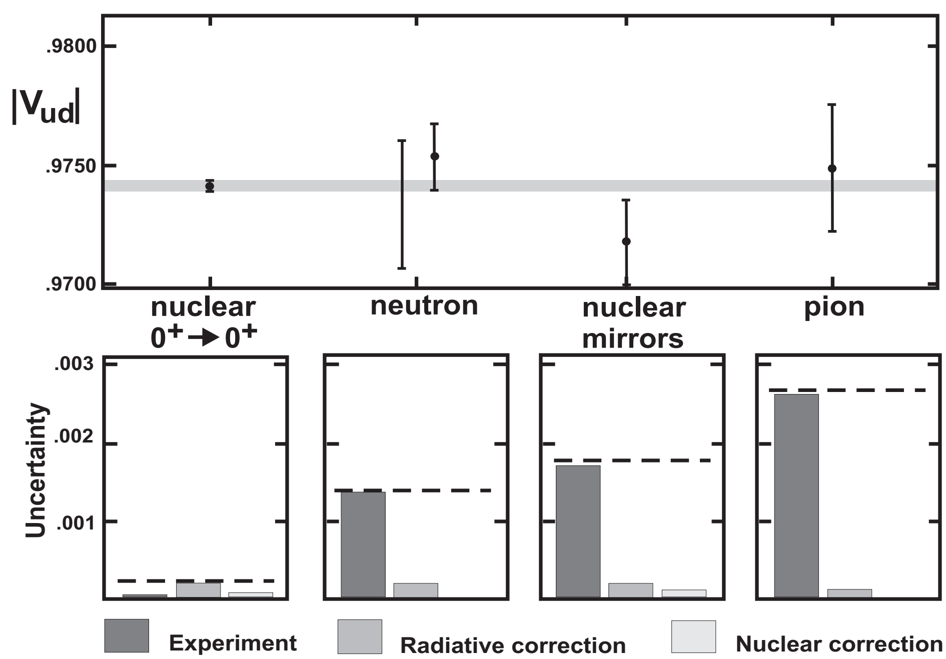

Figure 1.2: Comparison of uncertainty sources for various methods of measuring V_{ud} [21]. Nuclear superallowed decays have the lowest experimental uncertainty. If the experimental systematics can be improved for neutron decay, it would become a competitive measurement of V_{ud} as it does not require nuclear corrections.

where β is the ratio of the velocity to the speed of light and P is the neutron polarization. By measuring the electron counting rate asymmetry as a function of polarization, A can be extracted. The current best measurement comes from the UCNA experiment [6]. In this experiment, neutrons (UCNs) were produced by a 800 MeV pulsed proton beam incident on a tungsten spallation target. The spallated neutrons were moderated by cold polyethylene and down scattered by solid deuterium to become ultracold neutrons (UCN) with energies on the scale of neVs. The UCN were guided through a peak 7 T field that filtered the low-field spin state and an adiabatic spin flipper used to alternate the UCN spin states. The UCN were then ported to a 1 T holding field in a solenoid spectrometer which held the neutron spins aligned with the magnetic field. The emitted decay electrons then were guided by the field to two opposing electron detectors, see Figure 1.3. This resulted a beta asymmetry value of $A = -0.12015(34)_{stat}(63)_{sys}$[38].

The measurements with the highest precision thus far for neutron beta decay experiments come from A, but there is a significant discrepancy between results before and after 2002 (see Figure 1.4). It has been suggested this difference is related to the improvement of the systematic uncertainty for the measurement of neutron polarization between the two sets of experiments [38]. This change in A has shifted the value of λ, as can be seen in Figure 1.6.

Furthermore, recent changes in the electron energy independent radiative corrections, Δ_R^V, have drawn tension between the 0^+ to 0^+ nuclear decays and the unitarity of the CKM matrix. The previous accepted value of $\Delta_R^V = 0.02361(38)$ [32], has been shifted in a new analysis using a dispersive treatment of the inner radiative corrections, giving $\Delta_R^V = 0.02467(22)$ [45]. This shift is significant, as the inner radiative corrections are used to calculate V_{ud} in both nuclear and neutron decays.

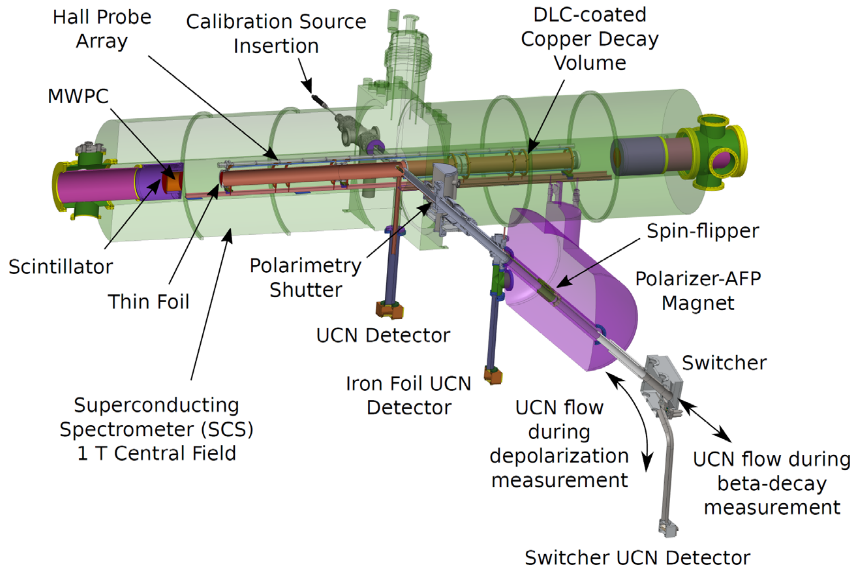

Figure 1.3: Set up for the UCNA experiment [38]. The Ultracold Neutrons are polarized by the Polarizer-AFP magnet, then guided to a decay volume within the superconducting spectrometer holding field (1 T). Decay electrons are guided to opposing electron detectors to measure the beta asymmetry.

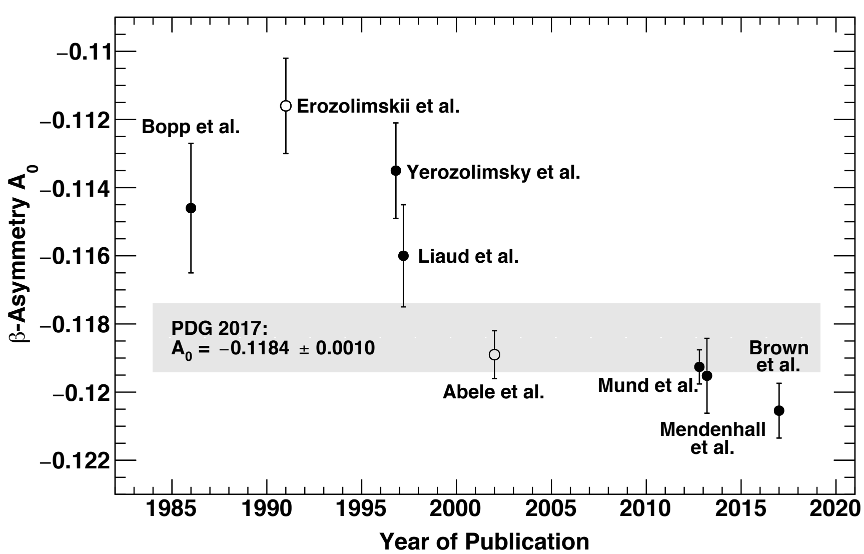

Figure 1.4: β Asymmetry for A over time [6]. A significant shift in A occurred with the improvement of the neutron polarization measurement post 2002.

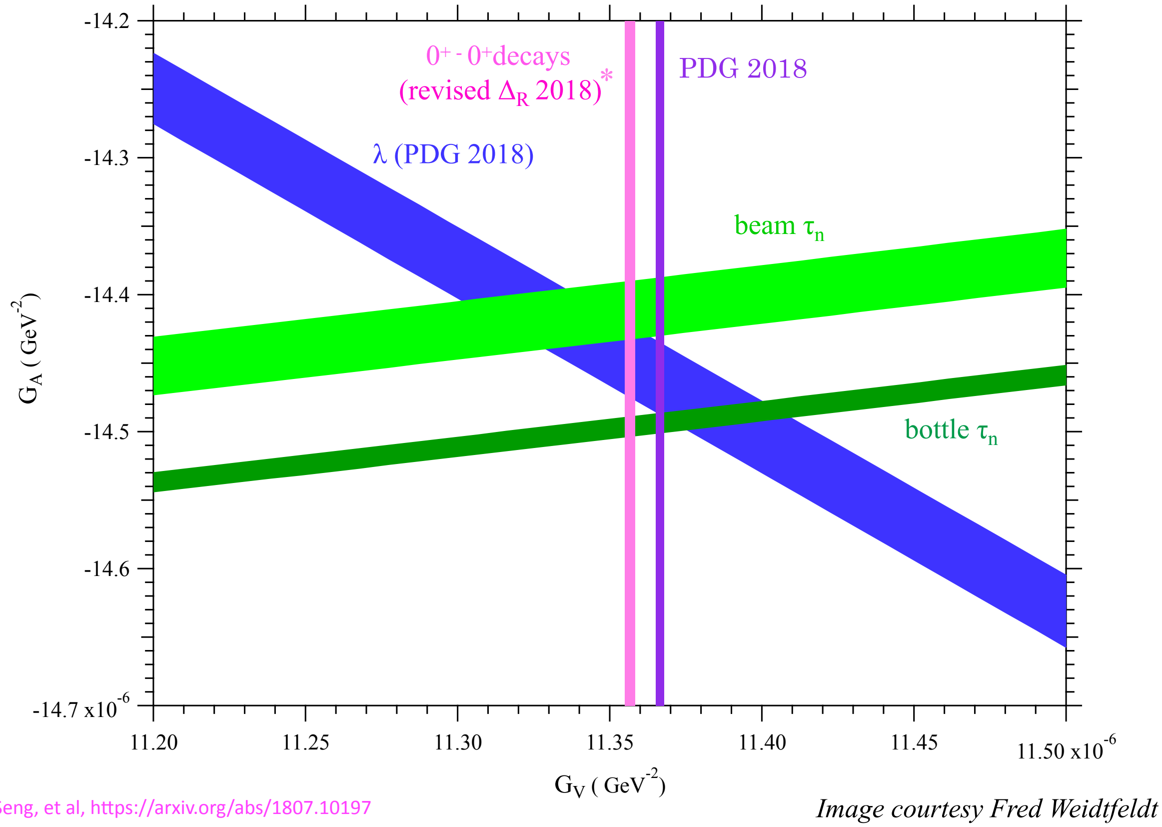

Figure 1.5: Plot showing relationship boundaries between G_V and G_A from various measurements [47, 45]. In this, λ is from the PDG 2018 average. Both results for the neutron lifetime (beam vs. bottle) are shown. While the PDG 2018 value of G_V agrees with unitarity, the recent update in radiative corrections has shifted the value away from unitarity.

$$|V_{ud}|^2 = \frac{2984.43s}{\mathscr{F}t(1+\Delta_R^V)} \quad \text{and} \quad |V_{ud}|^2 = \frac{5099.34s}{\tau_n(1+3\lambda^2)(1+\Delta_R^V)} \tag{1.21}$$

If the G_V-G_A relationship is plotted for 0^+ to 0^+ nuclear decays, τ_n from neutron decay and λ from electron asymmetry, as in Figure 1.5, one can see that the nuclear decays have shifted from CKM unitarity.

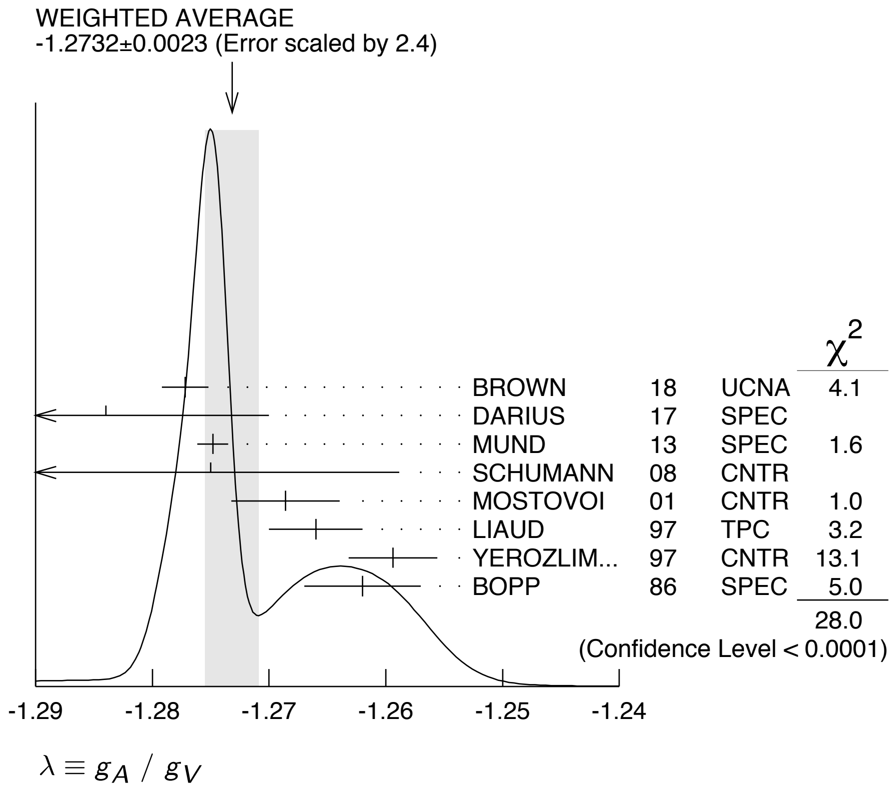

Figure 1.6: Plot of PDG accepted values for λ [47]. The shift in post 2002 A measurements is shown as a shift in λ.

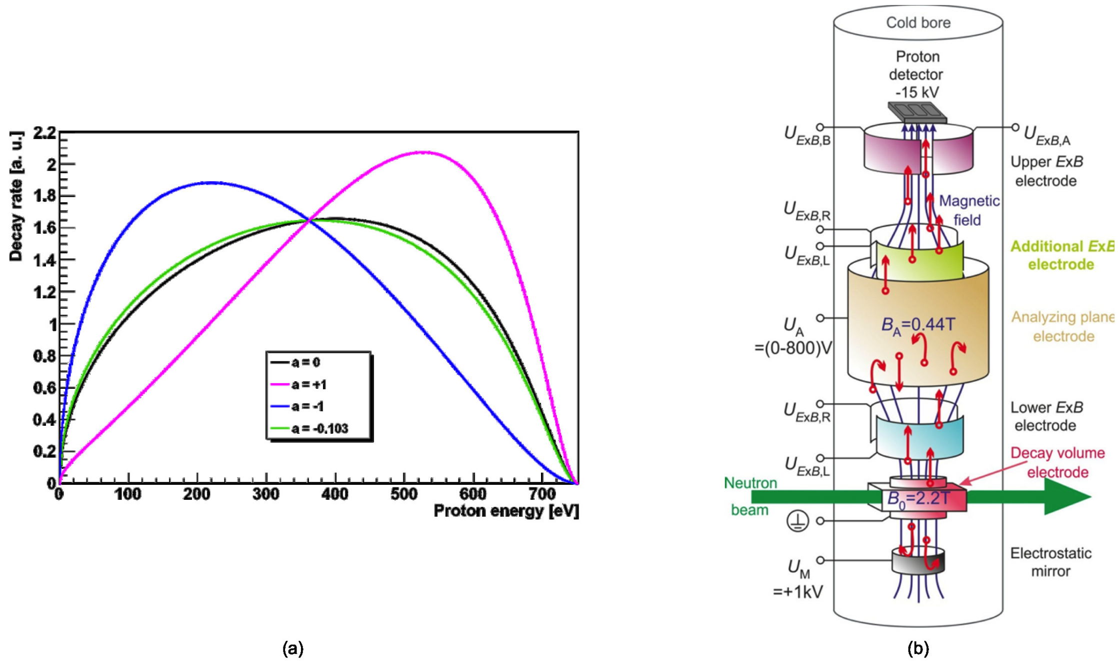

Figure 1.7: A plot showing the changes in the proton energy spectrum with different values of a and a schematic of the aSPECT experimental design. The protons produced by neutron decay are guided via a collimating magnetic field to a proton detector. Rejected protons are removed via a drifting $E \times B$ electrode [31].

The combination of the behavior of the electron asymmetry measurements and the unitarity of the nuclear decays is the motivation behind exploring a; this correlation parameter has a similar sensitivity to λ and does not require a polarization measurement, making it an independent check of V_{ud} from neutron beta decay. However, this type of measurement requires a precise measurement of the proton energy spectrum from beta decay, which has an endpoint energy of 751 eV; this has historically limited the precision of these experiments.

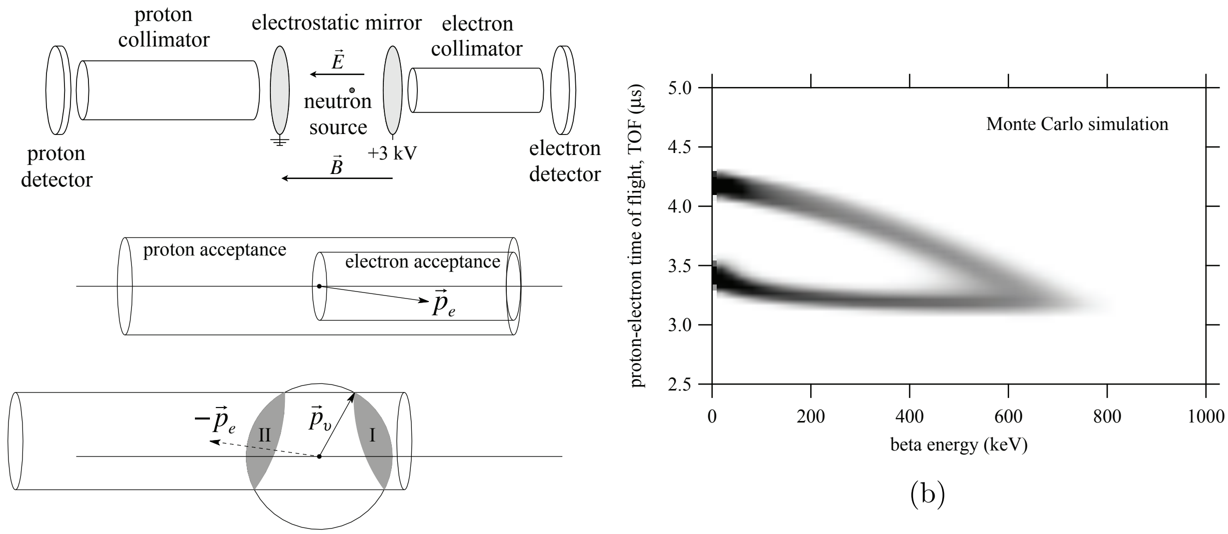

(b)

(a)

Figure 1.8: a) Diagram of the aCORN experimental method, showing the regions in which the antineutrino energies are calculated, I and II. b) A simulated "wishbone" asymmetry plot of the time of flight versus the beta energy [53].

There are three important experiments attempting to measure a: aSPECT, aCORN, and Nab. The first, aSPECT, extracted a from the shape of the proton energy spectrum, which relates to a as

$$W_p(T) \propto g_1(T) + a \cdot g_2(T) \tag{1.22}$$

Here $g_1(T)$ and $g_2(T)$ are functions of the proton kinetic energy. As can be seen in Figure 1.7, aSPECT uses a carefully designed spectrometer to collimate and guide protons from the neutron decay to a detector. a is extracted from the proton energy spectrum. This analysis is underway and is expected to determine a to 0.3% [31].

The most recent value of a has been determined by aCORN, an experiment performed at the National Institute of Standards and Technology. aCORN measures a as an asymmetry of the coincidence detection of electrons and protons from decay. The electron and proton decay products are guided to their respective detectors, as seen in Figure 1.8a. All protons are detected due to the presence of an electrostatic mirror, while only electrons with an axial momentum toward the electron detector are measured. The time of flight between the electron and protons are measured, giving a "virtual" antineutrino detection. This creates an asymmetry between long and short time of flight measurements that can be seen in Figure 1.8b, from which a can be extracted. aCORN has recently released a result of $a = 0.109 \pm 0.003_{stat} \pm 0.0028_{sys}$ [53, 36]. This is currently the best precision measurement of a. The Nab experiment, as discussed in the next chapter, aims to measure a to 0.1% uncertainty via a proton time of flight measurement.

Chapter 2

The Nab Experiment: Theory and Method

2.1 Theoretical Approach

The goal of Nab is to measure the electron-antineutrino correlation coefficient a to a relative precision of 10^{-3} and a place a limit on the Fierz interference term at 10^{-3}. As discussed previously, these terms come from the parametrized triple differential decay rate of a neutron written in terms of the electron and antineutrino momenta and energies as seen in Equation 1.17 [24].

The first step in Nab is to use a beam of unpolarized neutrons to eliminate the contribution of the spin correlated terms. Furthermore, the Fierz interference term, b, is equal to zero in the V-A theory. Limits on b from superallowed Fermi decay have given limits of $b_F = 0.0008 \pm 0.0028$ [51], so for determining a to 10^{-3}, the term can be set to zero.

$$\Gamma = f(E_e)\left[1 + a\frac{\vec{p_e}\cdot\vec{p_\nu}}{E_e E_\nu}\right] = f(E_e)\left[1 + a\beta_e cos\theta_{e\nu}\right] \tag{2.1}$$

where a is now proportional to the slope of the proton yield as a function of the cosine angle between the electron and antineutrino momenta.

A direct measurement of the antineutrino energies is impractical due to the low probability of interaction for antineutrinos. Instead, Nab makes use of momentum conservation. The Fundamental Physics Neutron Beam (FNPB) provides a beam of cold neutrons ($1 - 10\,\text{Å}$). Since the kinetic energy of the neutron is then negligible compared to the daughter particle kinetic energies, the neutron can be assumed to be at rest. Thus the total energy available to the decay is equivalent to the mass difference of the proton and neutron, that it

$$Q = M_n - M_p = 939.565\,\mathrm{MeV/c^2} - 938.272\,\mathrm{MeV/c^2} = 1.29333MeV/c^2 \tag{2.2}$$

This leftover energy can be separated into the kinetic energy of the daughter products and energy needed to produce the electron mass. The conservation of momentum, illustrated by the momentum triangle in Figure 2.1, indicates that the antineutrino energy can be found via knowledge of the Q value and by measuring the electron energy and proton momentum.

Furthermore, using conservation of energy and noting that the electron is relativistic, the maximum possible kinetic energy for the electron can be written as

$$p^2_{emax} = [(Q - M_e c^2)^2 + 2M_e c^2(Q - M_e c^2)]/c^2 = 1.412MeV^2/c^2 \tag{2.3}$$

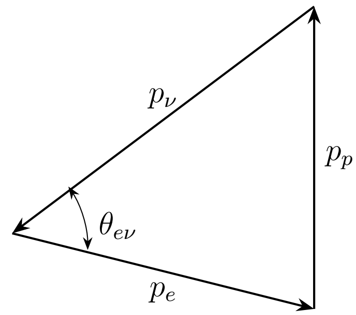

Figure 2.1: Momentum triangle for beta decay

with an endpoint energy of 782 keV. Meanwhile the proton has a maximum momentum when $p_{pmax} = p_e + p_\nu$. This means that the maximum proton energy comes from the case when the electron has most of the energy, and the proton and antineutrino are moving in the opposite direction, giving a maximum kinetic energy of 0.752 keV.

The phase space of the proton momentum versus the electron energy, as seen in Figure 2.2, is found using conservation of momentum

$$\vec{p_p} \cdot \vec{p_p} = p_e^2 + p_e p_\nu \cos\theta_{e\nu} + p_\nu^2 \tag{2.4}$$

and rewriting the squared proton momentum in terms of the electron energy and proton and electron masses. It follows that the yield spectrum of the proton momentum is

$$P_p(p_p^2) = \begin{cases} 1 + a\beta_e \frac{p_p^2 + p_e^2 + p_\nu^2}{2p_e p_\nu} & for \left| \frac{p_p^2 + p_e^2 + p_\nu^2}{2p_e p_\nu} \right| < 1 \\ 0 & \text{otherwise} \end{cases} \tag{2.5}$$

By measuring the electron energies, proton momenta, and calculating the antineutrino energy from the decay Q value, one can extract a from the yield spectrum of proton

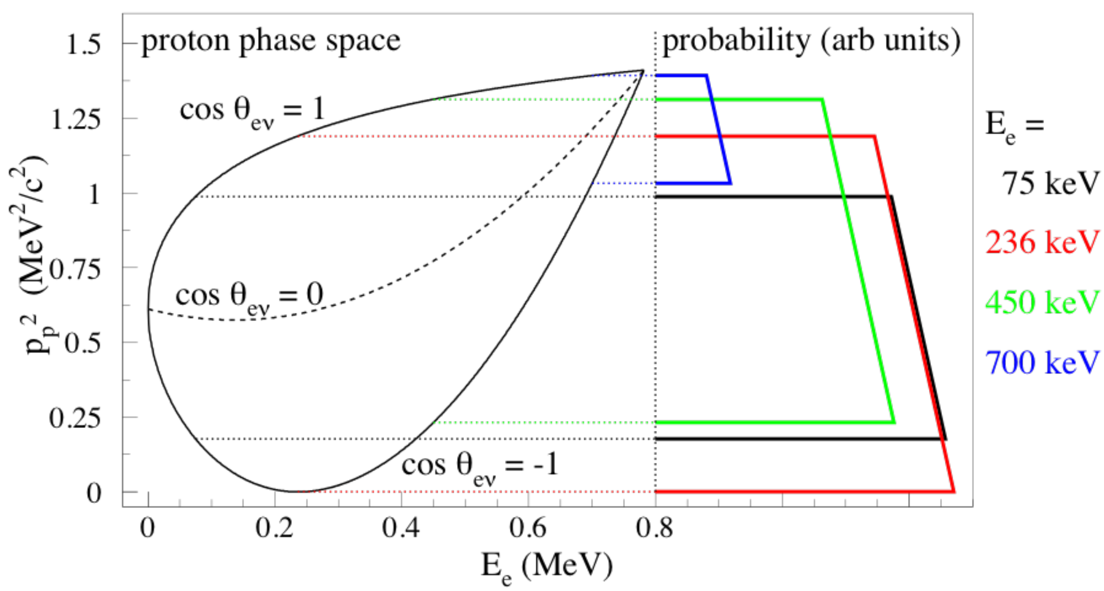

Figure 2.2: Phase space diagram for neutron beta decay [1]. The teardrop shape describes the accepted phase space of electron energies and proton momenta squared ranging from $\cos\theta_{ev} = 1$ to $\cos\theta_{ev} = -1$. At constant electron energy, this produces a trapezoidal yield spectrum for the proton momenta squared.

momenta at different electron energy cuts. Each cut of electron energy provides a separate determination of a, thereby reducing the uncertainty due to electron energy measurements.

2.2 Physical Implementation

The Nab experiment will run on the Fundamental Neutron Physics Beam Line (FNPB) at the Spallation Neutron Source at Oak Ridge National Lab, which emits pulses of cold neutrons at 60 Hz. This beam of neutrons is guided through a system of collimators, shielding, and a *spin flipper*, see subsection 2.2.1, to pass through a volume in which neutron decays are observed. As will be discussed in chapter 3, the expected decay rate is 2000 Hz; it is important to optimize the number of decays observed.

To do this, Nab uses a large superconducting cyrogenic magnetic spectrometer, subsection 2.2.3, to guide the charged daughter particles of the decays to two pixelated silicon detectors. These detectors, subsection 2.2.2, measure the deposited electron energy and the proton momentum. Instead, the relativistic electron is detected first and acts as a t_0 for a time of flight measurement of the proton. This is then converted to a proton momentum using knowledge of the proton flight path length.

2.2.1 Measuring Neutron Polarization

Previous measurements of a, i.e. aCORN at the NIST Center for Neutron Research, have found evidence of trace amounts of polarization that arise from the reflection of neutrons off of nickel in the beam guides [53]. However, there is no reason to expect the neutrons from the FNPB are polarized, as the beam uses multilayer supermirror guides. Recent tests of the polarization of these guides have not shown measurable polarization, but this remains a concern. Polarization of the neutron beam leads to contributions from the spin correlated terms in Equation 1.17, thereby increasing uncertainty in the measurement. The guides used for the FNPB, discussed in chapter 3, are nonmagnetic supermirrors and less likely to contribute significant polarization, but a check must be performed.

In Nab, this is done using a *spin flipper* - a device that uses adiabatic fast passage to reverse the neutron spin orientation and perform polarization measurements on the beam. A static monotonic holding field, B_0, is applied along the beam path to polarize the spins, and a perpendicular rotating field,$\vec{B_1}$, with an angular frequency of ω is applied perpendicularly to B_0, such that

$$\vec{B}_{lab} = B_0(z)\hat{z} + B_1(z)[\cos(\omega t)\hat{x} + \sin(\omega t)\hat{y}] \tag{2.6}$$

When the field is viewed from the frame of a rotating field,

$$\vec{B}_{rot} = \left(B_0(z) + \frac{\omega}{\gamma}\right)\hat{z} + B_1(z)\hat{x}_{rot} \tag{2.7}$$

it is clear that the B_0 holding field vanishes when rotating at the Larmor frequency, $\omega_L = -\gamma B_0$, leaving a static B_1 magnetic field. The neutron spin in this frame will seem to precess solely about B_1. If the field does not change rapidly, the dot product of the spin angular momentum $\vec{S}$ and the magnetic field $\vec{B}$ is an adiabatic invariant and the spin will follow the magnetic field. The angle between the field and the z axis in this frame will follow

$$\tan\theta = \frac{B_1(z)}{B_0(z) + \frac{\omega}{\gamma}} \tag{2.8}$$

The B_0 is monotonically decreasing and designed such that there will be some point along the neutron path where the RF frequency equals the Larmor frequency. The $\tan\theta$ will change sign as it passes through this point, indicating a full 180° rotation. Any neutron that passes fully through this field will have a complete *spin flip*.

To test the polarization of the beam line via the spin flipper, the beam must first be polarized. A cell filled with ^{3}He gas and Rubidium is polarized using Spin Exchange Optical Pumping (SEOP), where the cell is heated in an oven and the Rb is polarized via a circularly polarized laser. Collisions between the Rb and the ^{3}He result in spin-exchange, where the electron polarization of the Rb is transferred to the ^{3}H nuclei. The cell is placed at the beginning of the beam, before the spin flipper. The polarized ^{3}He preferentially absorbs neutrons with antiparallel spins, thereby filtering the polarization of the beam to the parallel spin.

Once the beam is filtered to a known polarization, the spin flipper is used to flip the neutron spins. A second polarized ^{3}He cell is placed after the spin flipper to analyze the polarization via absorption. First, two measurements will be made with the polarized ^{3}He cell, with both spin orientations. Then, this is compared to the transmission and polarization found with an unpolarized ^{3}He cell. By comparing the transmission of the beam through the polarized and unpolarized cells, a measurement of the original beam polarization can be made.

As previously stated, there is no expectation that the FNPB will have a measurable polarization. However, in the event that some amount of polarization is detected, this system additionally allows for a correction. The experiment can run while using the spin flipper to alternate between two polarizations of the beam. The results average to zero spin polarization, thereby negating the additional polarization terms in Equation 1.17.

2.2.2 The Pixelated Silicon Detectors

As mentioned, the protons and electrons from decays that occur in the fiducial volume are guided by the magnetic field to two opposing segmented silicon detectors. With energies ranging up to 782 keV, beta decay electrons have sufficient energy to pass pass through the deadlayer of current silicon detector technologies and be resolved. However, the proton maximum kinetic energy is only 751 eV; this is not enough energy to pass through the deadlayer of the detector, let alone be detected above the noise threshold. A 30 kV potential difference is applied to the detectors to accelerate the protons to pass through the deadlayer. However, the energy resolution at this range is still unsatisfactory. Instead, the proton momentum is determined from its time of flight. In this coincidence measurement, a proton should be seen 13- 50 μs after the corresponding electron. The proton trajectories will follow the magnetic field, and precisely measuring this path length and the time of flight from decay to detection gives a precise measurement of the proton momentum.

This gives the detectors for Nab a number of requirements. Due to the challenge of detecting low energy protons, the detector must have both low noise and a thin entrance window. However, the detector itself must be thick enough to fully stop the higher energy

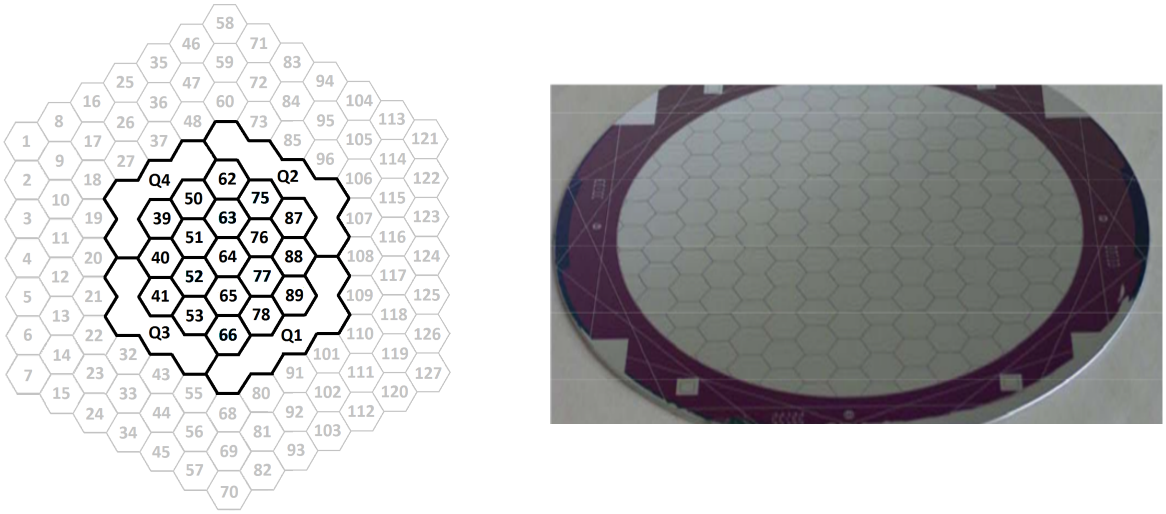

Figure 2.3: 127 hexagonal pixel design for the Si detectors [5] . The pixelation of the detector surface allows for a larger detector as well as pixel tracking for coincident signals.

electrons with a thin enough dead layer to limit backscattering. The active surface area must be large enough to collect the total decay rate and allow for the spectrometer magnetic field to expand. The detector must have fast and stable timing, enough to distinguish and order backscattering events and properly measure the proton time of flight.

Nab solves this with two pixelated n-type on n-type design silicon detectors manufactured by Micron Semiconductor Ltd. These consist of 127 hexagonal pixels with an area of $70\,\mathrm{mm}^2$. The pixelation allows better position tracking of both decay and backscattering events. The pixels are 1.5 to 2 mm thick and the full active area has a diameter of 11.5 cm. The detectors have been characterized with a noise threshold of 6 keV and an energy resolution of 3 keV, and have been demonstrated to detect protons with energies as low as 15 keV. [5]

2.2.3 Design of the Nab Spectrometer

The two observables in Nab are the electron energy and the proton momentum, which is determined from the proton time of flight. However this measurement is meaningless without a detailed understanding of the proton flight path, which is governed by the magnetic and electric fields present. The Nab spectrometer has been carefully designed with this in mind.

The time of flight measurement has a heavy influence on the magnetic field design requirements. While direction of the particle momentum is irrelevant in a direct energy measurement, a time of flight measurement only detects the component of the momentum aligned to the magnetic field lines, $p_\parallel$. To get around this, the Nab spectrometer field makes use of of the first adiabatic invariant,

$$\mu = \frac{p_\perp^2}{2m_p B} = \frac{T\sin^2\theta}{B} = \text{constant} \tag{2.9}$$

where θ is the opening angle between the momentum vector and field line. This proportional relationship between $\sin^2\theta$ and the magnetic field strength allows the alignment of the momentum to be controlled by changing the field strength. By decreasing the field strength, the momentum can be *longitudinalized* along the field lines such that $p_\parallel \approx p_{total}$. Since a magnetic field does no work, this process occurs without reducing or changing the total kinetic energy T.

$$\sin^2\theta_2 = \frac{B_2\sin^2\theta_1}{B_1} \tag{2.10}$$

In an ideal magnetic field, this decrease in field strength would be enough to longitudinalize all particles within $0 \leq \theta \leq \pi/2$. However, restrictions on space limit the length of the magnet. With a non-infinite path, charged particles at angles near $\theta \approx \pi/2$ will not fully longitudinalize before reaching the detector, creating a delayed signal that can create background in the coincidence detection.

To reduce this background, a magnetic mirror is used to filter these "shallow" protons. Using the first adiabatic invariant, it follows that an increase in field strength from B_0 to B_1 where $B_1 > B_0$ increases the $\sin\theta_2$. If θ_2 increases past $\pi/2$, the proton flips direction. Therefore, inserting an increase in field will accept only protons within

$$\cos\theta_0 \geq \sqrt{1 - \frac{B_0}{B_F}} \tag{2.11}$$

Any protons with initial angle in this range can then be longitudinalized by a following decrease in field.

Using this technique, the Nab spectrometer field is designed to have a large field peak after the decay volume and then a decrease in field strength between the filter peak and the detector. To reduce the uncertainty due to the time it takes to filter and longitudinalize the proton momentum, a long low field time of flight region follows this decrease in field strength. Finally, the field increases again at the detector surface to constrain the field lines to the detector surface area. The full designed field can be seen in Figure 2.4.

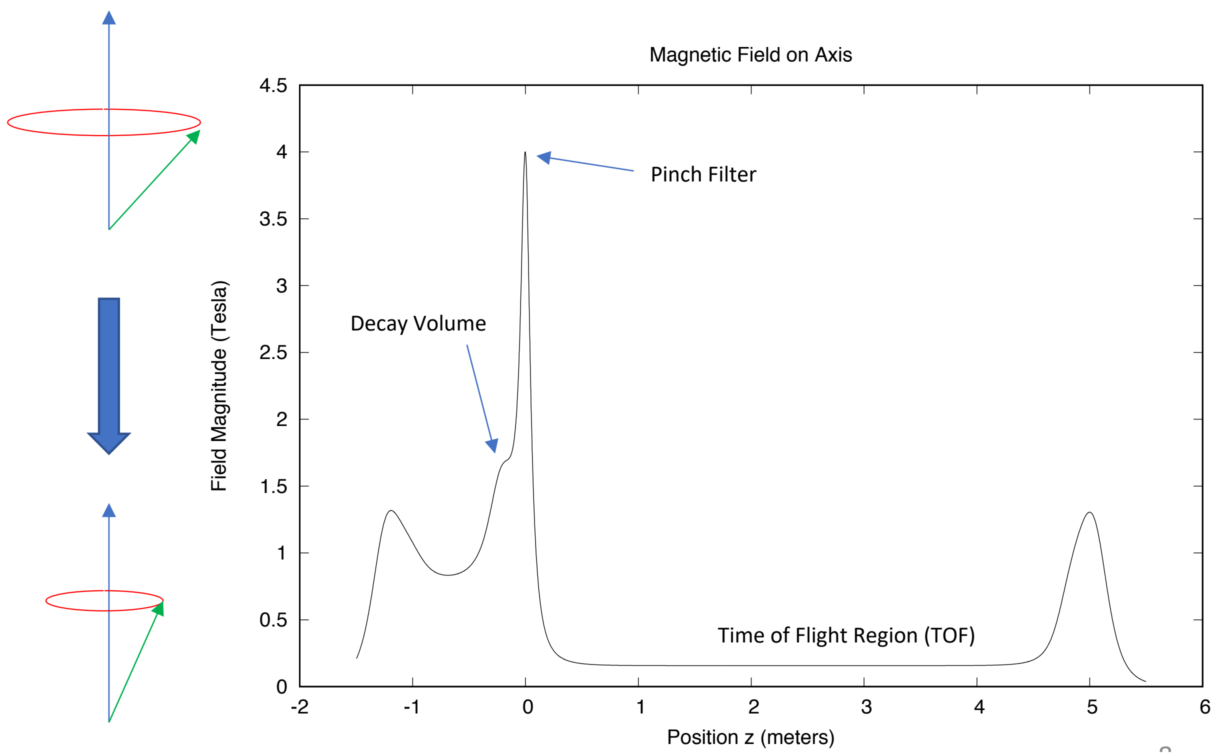

Figure 2.4: The magnetic field design on axis, showing the filter feature and time of flight region. This design longitudinalizes the proton momenta along the magnetic field lines.

2.2.4 Connecting Proton Momentum and Time of Flight

The relationship between the observed proton time of flight and the initial decay proton momentum is a major source of systematic uncertainty. The time of flight can be described as

$$t_p^2 = \frac{m_p^2 L^2}{p_\parallel^2} \tag{2.12}$$

where $p_\parallel$ is the momentum aligned with the magnetic field, L is the path length, and m_p is the mass of the proton. The two main sources of uncertainty are the proton path length, which varies over the decay volume, and the amount by which the proton is longitudinalized along the magnetic field.

Both the proton path length and the degree of longitudinalization are dependent on the magnetic fields and electric potentials experienced by the protons. First, the measured proton energy only has the component parallel to the field lines (or perpendicular to the detector surface). Using the first adiabatic invariant discussed previously, the parallel kinetic energy can be written as a function of the magnetic field and the electric potential along the proton path.

$$T_\parallel = T_0 - e(V(l) - V_0) - T_0 \frac{B(l)}{B_0} \sin^2\theta_0 \tag{2.13}$$

Rewriting this in terms of proton momentum and applying it to Equation 2.12 gives

$$t_p^2 = \frac{m_p^2}{p_0^2} \left[\int \frac{dl}{\sqrt{1 - \frac{e(V(l)-V_0)}{T_0} - \frac{B(l)}{B_0}\sin^2\theta_0}} \right]^2 \tag{2.14}$$

where p_0 is the initial proton momentum, T_0 is the initial proton kinetic energy, B_0 is the initial magnetic field at decay, V_0 is the initial electric potential at decay, and θ_0 is the initial angle between the proton momentum and the field line. This allows the time of flight to be separated as

$$\frac{1}{t_p^2} = \frac{p_0^2}{m_p^2 L_{eff}^2}, \quad L_{eff} = \int \frac{dl}{\sqrt{1 - \frac{e(V(l)-V_0)}{T_0} - \frac{B(l)}{B_0}\sin^2\theta_0}} \tag{2.15}$$

where L_{eff} is the effective path length of the proton. This can be rewritten as $r = \frac{1}{L_{eff}^2}$ such that the inverse time of flight is a product of two independent random variables, p_0^2 and r. The probability density function of the inverse time of flight can now be written in terms of the p_0^2 spectrum and the r spectrum, $f_r(r)$.

$$\frac{1}{t_p^2} = \frac{p_0^2}{m_p^2 L^2} = p_0^2 r \tag{2.16}$$

$$f_{1/t_p^2}(1/t_p^2) = \int f_{1/t_p^2, p_0^2}(p_0^2 r, p_0^2)dp_0^2 = \int f_{p_0^2}(p_0^2) f_r(r)\frac{1}{p_0^2}dp_0^2 \tag{2.17}$$

The $f_{p_0^2}(p_0^2)$ density is given by Equation 2.5, while the $f_r(r)\frac{1}{p_0^2}$ term is the spectrometer response function. If the integral over p_0^2 is rewritten in terms of r, the inverse time of flight spectrum can be written as

$$p_0^2 = \frac{1}{rt_p^2} \quad dp_0^2 = -\frac{1}{t_p^2 r^2} dr = -\frac{p_0^2}{r} dr \tag{2.18}$$

$$f_{1/t_p^2}(1/t_p^2) = -\int_{r_{max}}^{r_{min}} (1 + aB_e \frac{1}{rt_p^2} + aC_e) f_r(r) \frac{1}{r} dr \tag{2.19}$$

$$f_{1/t_p^2}(1/t_p^2) = \left[\int_{r_{min}}^{r_{max}} f_r(r) \frac{1}{r} dr - aC_e \int_{r_{min}}^{r_{max}} f_r(r) \frac{1}{r} dr \right] + a \left[B_e \int_{r_{min}}^{r_{max}} f_r(r) \frac{1}{r^2} dr \right] \frac{1}{t_p^2} \tag{2.20}$$

which is a linear function with a slope proportional to a. This can be extracted by a correction of B_e from electron energy and $\int f_r(r) \frac{1}{r^2} dr$ from the spectrometer response function.

To estimate the required uncertainty for the spectrometer response function, a can be rewritten in terms of the slope of the inverse time of flight yield, such that

$$a = \left[C_e \int f_r(r) \frac{1}{r^2} dr \right]^{-1} \frac{d}{d(1/t_p^2)} f_{1/t_p^2}(1/t_p^2) \tag{2.21}$$

$$\frac{\delta a}{|a|} \approx \frac{\delta C_e}{|C_e|} + \frac{\delta[\int f_r(r) \frac{1}{r^2} dr]}{|\int f_r(r) \frac{1}{r^2} dr|} + \frac{\delta[\frac{d}{d(1/t_p^2)} f_{1/t_p^2}(1/t_p^2)]}{|\frac{d}{d(1/t_p^2)} f_{1/t_p^2}(1/t_p^2)|} \tag{2.22}$$

To measure a to a relative uncertainty of 10^{-3}, the integral over the spectrometer response must be known to about 10^{-3}.

2.2.5 Calculating the Spectrometer Response Function

There are two independent potential methods for calculating the spectrometer response function:

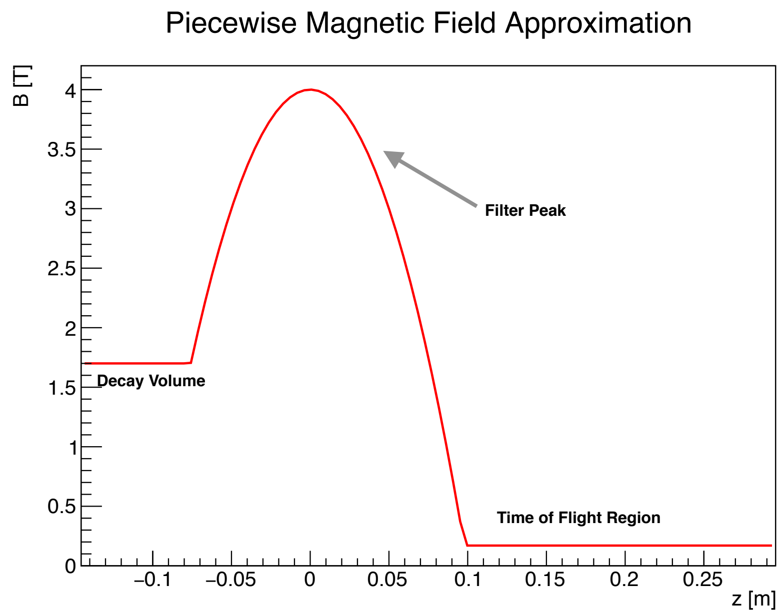

Figure 2.5: The spectrometer magnetic field "toy" approximation with $\alpha = 15\,\mathrm{m}^{-1}$, $B_0 = 1.7\,\mathrm{T}$, $B_F = 4\,\mathrm{T}$, and $B_{TOF} = 0.1\,\mathrm{T}$.

- **Method A:** The response function is found by modeling the spectrometer fields in GEANT4 code and performing a Monte Carlo sampling of $f_r(r)$.

- **Method B:** The response function $f_r(r)$ is calculated numerically using a fitted expansion of the spectrometer fields.

Method B was used to estimate the error budget for Nab using a simplistic "toy" model of the magnetic field. In this method, the field approximates the decay volume and time of flight regions as constant, and the filter region as a parabola, $B(z) = B_F(1 - \alpha^2 z^2)$ with some curvature α, where B_F is the peak field.

As a base approximation, the electric potential is constant, $V(l) = V_0$, and r is calculated piecewise over the magnetic field.

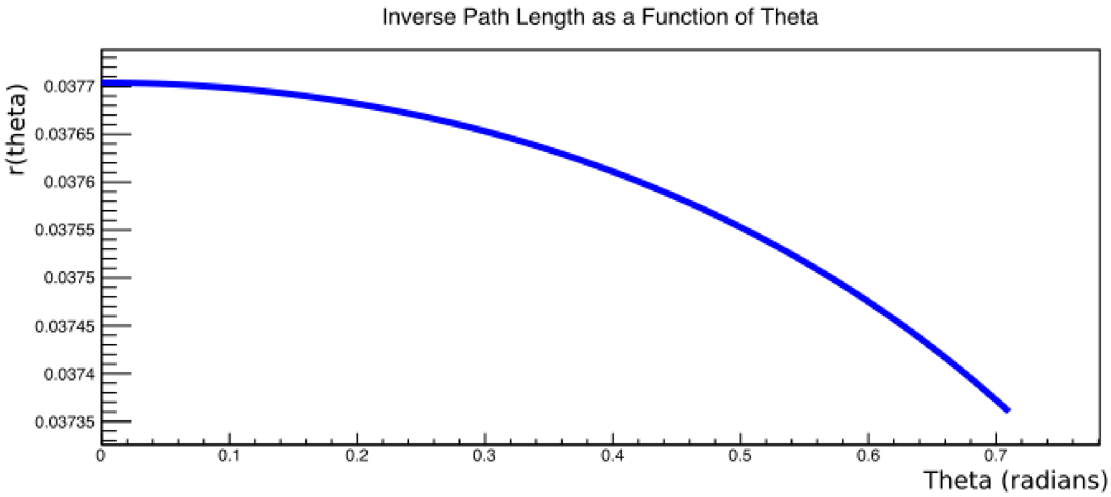

Figure 2.6: A plot of the $r(\theta)$ for the toy function with $\alpha = 15\,\mathrm{m}^{-1}$, $B_0 = 1.7\,\mathrm{T}$, $B_F = 4\,\mathrm{T}$, and $B_{TOF} = 0.1\,\mathrm{T}$.

$$r = \frac{1}{L^2} = \left[\int \frac{dl}{\sqrt{1 - \frac{e(V(l)-V_0)}{T_0} - \frac{B(l)}{B_0}\sin^2\theta_0}}\right]^{-2} = \left[\int \frac{dl}{\sqrt{1 - \frac{B(l)}{B_0}\sin^2\theta_0}}\right]^{-2} \tag{2.23}$$

$$r = \left[\int_{z_0}^{z_1} \frac{dl}{\sqrt{1-\sin^2\theta_0}} + \int_{z_1}^{z_2} \frac{dl}{\sqrt{1 - \frac{B_F(1-\alpha^2 z^2)}{B_0}\sin^2\theta_0}} + \int_{z_2}^{z_f} \frac{dl}{\sqrt{1 - \frac{B_{TOF}}{B_0}\sin^2\theta_0}}\right]^{-2} \tag{2.24}$$

where $z_1 = \frac{1}{\alpha}\sqrt{1 - \frac{B_0}{B_F}}$ and $z_2 = \frac{1}{\alpha}\sqrt{1 - \frac{B_{TOF}}{B_F}}$. This function is integrated numerically, and the resulting $r(\theta)$ function can be seen in Figure 2.6.

The response function can be calculated using this $r(\theta)$ and taking into account the probability density function of θ, which is not uniform. If the proton emits isotropically from the point of decay, then the probability of some $a \leq \theta \leq b$ with respect to the field line follows as

$$P_\Theta(a \leq \Theta \leq b) = \int_a^b \int_0^{2\pi} \sin\theta d\theta d\phi = \int_a^b 2\pi \sin\theta d\theta = 2\pi(\cos a - \cos b) \tag{2.25}$$

$$f_\Theta(\theta) \approx \sin\theta \tag{2.26}$$

Using this, the $r(\theta)$ distribution and the response function $\Phi(1/t_p^2, p_0^2)$ can be determined using a change of variables and calculated numerically. The response function calculated from the toy model can be seen in Figure 2.7a. The time of flight spectrum is found by integrating over the proton momentum spectrum and the response function, creating the smeared distribution seen in Figure 2.7b.

The systematic error budget for the Nab spectrometer was determined using this toy magnetic field. A time of flight spectrum was created using chosen values for a, α, $r_B = B_{TOF}/B_F$, and $r_{DV} = B_{DV}/B_F$, and fitted for a while varying α, r_B, and r_{DV}.

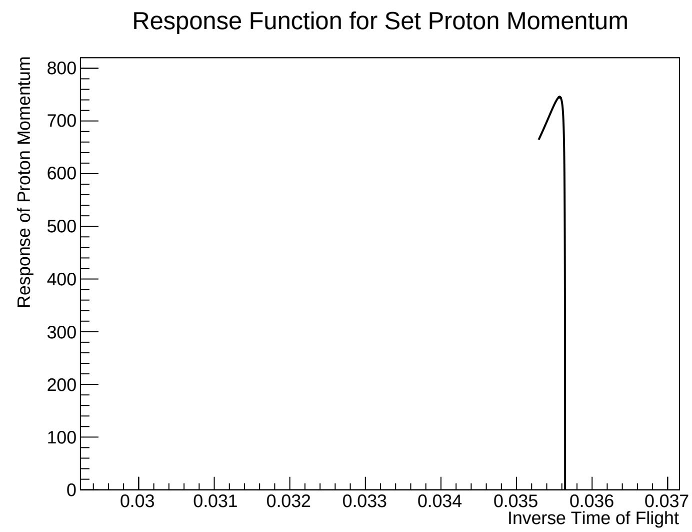

(a)

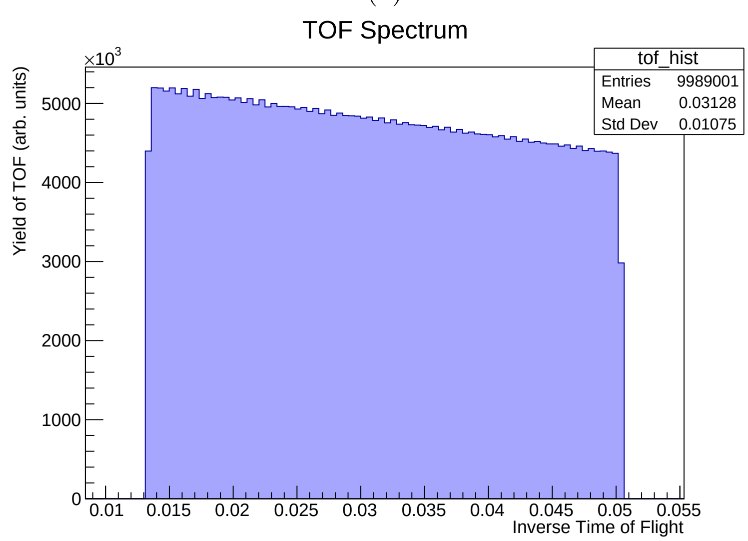

(b)

Figure 2.7: a) The response function of the "toy" spectrometer field. A perfect response function would be a delta function, but the magnetic field of the spectrometer widens the response. b) The $1/t_p^2$ spectrum is the p_0^2 spectrum "smeared" by the response function, but the inner slope is still linear and can have a extracted from it. $E_e = 0.5\,\mathrm{MeV}$

Experimental Parameter	Principle specification	$(\Delta a/a)_{syst}$
Magnetic Field:		
curvature at pinch	$\Delta\gamma/\gamma = 2\%$ with $\gamma = (d^2 B_z(z)/dz^2)/B_z(0)$	5.3×10^{-4}
ratio $r_B = B_{TOF}/B_F$	$(\Delta r_B)/r_B = 1\%$	2.2×10^{-4}
ratio $r_{B,DV} = B_{DV}/B_F$	$(\Delta r_{B,DV})/r_{B,DV} = 1\%$	1.8×10^{-4}
L_{TOF}**, length of TOF region**		(*)
U inhomogeneity:		
in decay / filter region	$\|U_F - U_{DV}\| < 10$ mV	5×10^{-4}
in TOF region	$\|U_F - U_{TOF}\| < 200$ mV	2.2×10^{-4}
Neutron beam:		
position	$\Delta\langle z_{DV}\rangle < 2$ mm	1.7×10^{-4}
profile (incl. edge effect)	slope at edges <10% / cm	2.5×10^{-4}
Doppler effect	analytical correction	small
unwanted beam polarization	$\Delta\langle P_n\rangle < 2 \cdot 10^{-9}$ torr (with spin flipper)	measure
Adiabaticity of proton motion		1×10^{-4}
Detector effects:		
E_e calibration	$\Delta E_e < 200$ eV	2×10^{-4}
proton trigger efficiency	$\Delta N_{tail}/N_{tail} \leq 1\%$ / cm	3.4×10^{-4}
TOF shift (det./electronics)	$\epsilon_p < 100$ ppm/keV	3×10^{-4}
Shape of E_e Response		4.4×10^{-4}
TOF in Acceleration Region	$r_{electrodes}$	3×10^{-4}
Electron TOF	analytic correction	small
BGD/accid. coinc's	(will subtract out of time coinc)	small
Residual gas	$P < 2 \cdot 10^{-9}$ torr	3.8×10^{-4}
Overall Quadrature Sum		1.2×10^{-3}

* Free fit parameter

Table 2.1: Nab Budget of Systematic Uncertainties

Chapter 3

Neutronics in Nab

In Nab, background radiation is a concern for two reasons. The first is the background in the detectors, which can interfere with the experimental signal. The other is personnel protection from radiation dose. Due to these issues, a comprehensive modeling and design of the radiation and shielding is necessary.

The electrons and protons are detected using two asymmetric pixelated Si detectors. While these detectors are used to detect both decay particles, they are limited by an energy resolution of 15 keV and cannot distinguish between different types of radiation. The decay protons have a maximum kinetic energy of 752 eV, well below the noise threshold of the detectors. To solve this, the protons are accelerated by a 30 kV potential, turning the momentum measurement into a time of flight measurement; the relativistic electron provides a t_0 for this measurement. Background radiation, such as gammas or stray neutrons, can deposit energies similar to those expected for electrons and protons and create false coincidences.

The probability of a false coincidence scales with the time-averaged reaction rate of background events. A time window of 10^{-5} seconds and a total singles rate of 10^3 Hz gives a false coincidence rate of 10^{-2} Hz. Accounting for geometric factors, a decay rate on the order of 10^3 Hz will have a signal around 200 Hz; keeping a one-to-one ratio of singles background events to the decay rate limits the systematic error to only 5×10^{-3} percent. The coincidence rate will be further suppressed by requiring that "true" coincidences be in adjacent or conjugate detector pixels.

The majority of the background radiation in Nab comes from the interaction of neutrons with materials along the beamline. The FNPB emits a neutron beam comprised of cold and fast neutrons with secondary gammas from neutron capture and has an approximate divergence of 3 degrees. Proper collimation of the beam is essential for limiting neutron capture on materials and any unavoidable sources of neutron or gamma radiation must be shielded with materials such as lead, borated polyethylene, and stainless steel.

Due to the complexity and statistics of this modeling, deterministic computational models are insufficient. Instead, Monte Carlo methods are employed to sample and model both beam behavior and particle interaction in materials. The initial beam behavior and collimation was modeled using McStas, a Monte Carlo ray-tracing program [29, 56, 55, 57]. By treating the sampled neutrons as rays that can reflect and transmit on materials, the shape and density of the neutron beam can be modeled. This was used to optimize the flux of neutrons in the decay volume and the collimation of the beam.

Interactions of the beam with materials were modeled using Monte Carlo N-Particle eXtended (MCNPX)[13], which contains an extensive material cross section library. The collimation and other beam line components were modeled in MCNPX and used to simulate the production of background radiation from the neutron beam interactions with materials. This allowed calculation of the background singles decay rate of gamma and neutron radiation and the dose rate seen external to the experiment.

3.1 The SNS and the Fundamental Physics Beam Line

At the Spallation Neutron Source at the Oak Ridge National Laboratory, neutrons are produced by a 1.4 MW pulsed proton beam targeted on a steel encased liquid mercury target. The 60 Hz pulse of the proton beam strikes the nuclei of the target at a high enough energy to effectively shatter the nucleus into fragments, a process known as *spallation*. Approximately 20-30 neutrons are produced per incident proton pulse on the mercury target. The emitted neutron energies average about 1 MeV, and must be moderated. An additional high energy fraction ranging up to 1 GeV dominates shielding needs for the target. The SNS has four moderators; three liquid hydrogen and one liquid water, in aluminum vessels and surrounded by a heavy-water cooled beryllium reflector. The FNPB views one of the liquid hydrogen moderators. The neutrons are initially slowed down by the hydrogen moderator and the beryllium reflector. During this process, neutrons leak out of the viewed face of the hydrogen moderator forming a beam of neutrons with useful energies from about 1- 100 meV. A plot of the moderated neutron source spectrum can be seen in Figure 3.1a.

The FNPB is split by two monochromator crystals into a $8.9\mathring{A}$ beamline and a polychromatic cold beam line. There are two neutron choppers currently placed along the beam used to select a range of neutron energies for the cold beam line when required. The upstream section of the guide is curved with a 117 m radius bend towards beam left

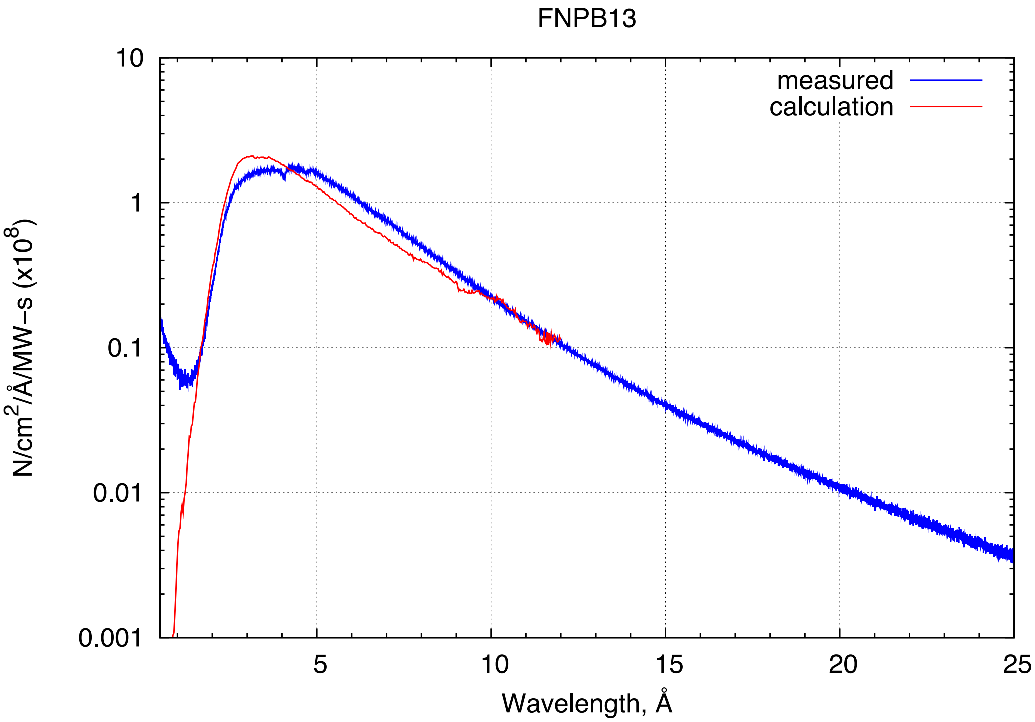

(a) A plot of the Spallation Neutron Source Intensity, calculation compared to measurement [15].

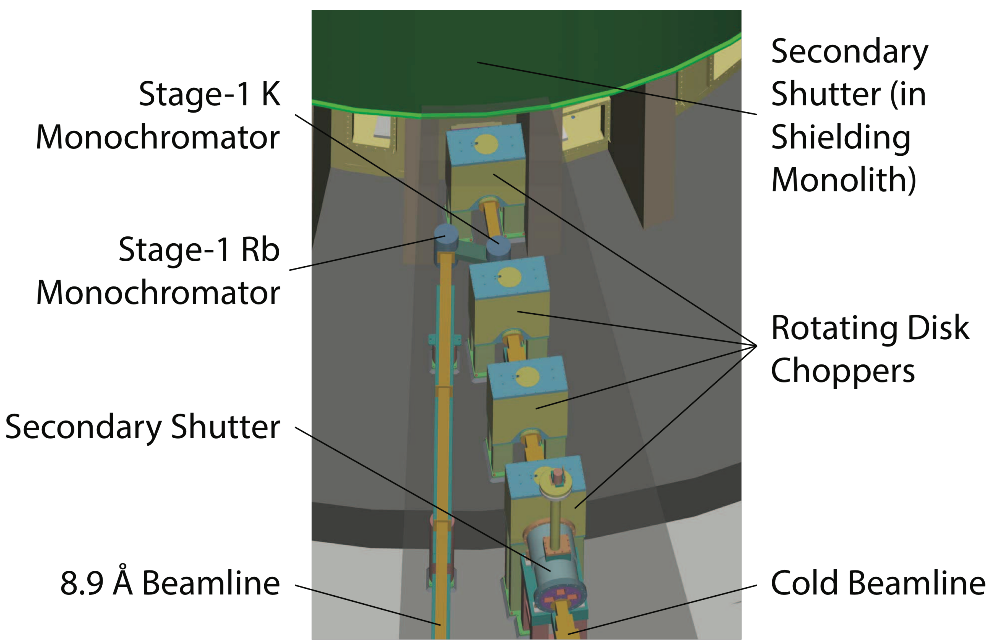

(b) Components of FNPB from the liquid hydrogen moderator to the cold beam line exit [15].

Figure 3.1

to minimize background from fast neutrons and gammas. The curvature of the beamline reduces the fast neutron and gamma background seen from the mercury target. The Nab experiment is placed on the cold neutron beamline and the full polychromatic spectrum is used to maximize statistics. The choppers and neutron guides were modeled in McStas when designing the beam line, and it is this model that is used for the basis of the Nab calculations in McStas.

McStas is a geometrical optics program that treats the beam as a source of neutron “rays”, which have energy and direction. This software is insufficient for modeling the material interactions of the beam as it does not include any information about the material cross sections. In constrast, MCNPX has a large cross section library and treats the beam as a source of particles. Though the majority of the beam consists of cold neutrons, there are also fast neutron and gamma components that come from the target. The full model of the FNPB source from the moderator was provided by the Neutronics team at the ORNL and has been validated by measurement [15]. This source model is divided into three source beams; the cold neutron beam, the fast neutron beam, and the gamma beam. The total radiation effects must come from modeling all three of these sources.

3.2 Modeling of the Nab Beam Line

To determine the electron-antineutrino correlation parameter for neutron beta decay, Nab must measure the electron energies and proton momenta from the decay as precisely as possible. However, the observable neutron decays occur in a cylindrical volume 8 cm in height and 3 cm in radius, determined by the size and shape of the superconducting magnet

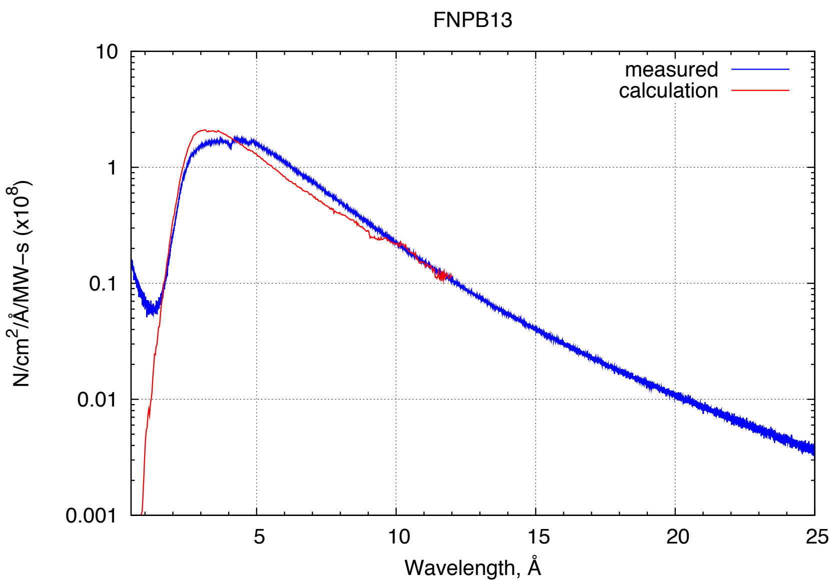

Figure 3.2: A plot of the beam intensity for the Fundamental Physics Beam Line compared to measurement [15].

spectrometer. Neutrons that do not decay in this fiducial volume are ultimately absorbed in some material and are a large source of potential background. Capture of a neutron on the materials used in the experiment results in isotropic emission of gammas or fast neutrons that can cause false coincidence events in the detectors. This can be mitigated by both reducing the neutron beam interaction with materials and proper shielding of any sources of radiation. The easiest way to reduce neutron interaction with materials is to reduce the beam size. Yet, Nab is a low statistics experiment and requires an optimization of the neutron decay rate, which requires a larger beam size. The goal of this study is to balance the beam line design between maximizing the decay rate and reducing the beam size.

Additionally, the beam must be sufficiently uniform to account for the "edge effect". When a neutron decays within the decay volume, the proton and electron products are directed toward the Si detectors via a magnetic field. Ideally, the particles would follow the field lines exactly. However, the gyration radius of a charged particle about a magnetic field line means that the horizontal displacement of the particle from the decay volume to the detector cannot be predicted, only averaged. Particles following field lines at the edge of the detector will have some probability of not being detected, while particles following field lines just outside of the detector will have some probability of displacing themselves into the detector. In a perfectly uniform beam, the average number of particles gyrating away from the detector would equal the number of particles gyrating into the detector, and the edge effect would be negligible. Otherwise, there is an error in the count rate of decays near the edge of the decay volume that is dependent on the gradient of the beam profile. A 10% gradient or less in intensity across the beam is sufficient for a 10^{-3} uncertainty in measuring a.

Initially a tapered guide was considered for the beam line. This structure is a neutron supermirror guide that optically focuses the beam. This has two major advantages - it increases the flux of the beam and it reduces the size of the beam without neutron capture on materials. However, the focusing nature of the guide increases the divergence of the beam and affects beam uniformity. As can be seen in Figure 3.3, the tapered guide induces a gradient in the beam profile greater than our requirement of 10%. Furthermore, while the tapered guide focuses the beam in the decay volume, the increased divergence expands the beam through the exit port and leads to sources of background from inside the magnet. Thus, the tapered guide design was summarily rejected.

Instead, the beam design focuses on collimation, where apertures of neutron absorbing material are used to trim the beam size. Neutrons close to the beam axis that pass through the opening of the collimator continue with the beam, while neutrons that are closer to the beam edges will be captured on the material. This sharpens the beam edges without compromising the intensity of the beam or its uniformity. One issue, however, is that any neutron capture inherently produces background radiation, including capture on materials in the collimators. Therefore, the collimators must be strategically placed where proper shielding can be implemented. In Nab, the collimators can be placed both outside of the magnet and within the magnet port channels leading to the decay volume. Though collimators in the magnet port channel are closer to the decay volume and can create a sharper beam, they are almost impossible to shield in direct line of sight of the detectors. Careful iteration of modeling the collimation in McStas and the detector backgrounds in MCNPX is important in creating an effective collimation and shielding design.

3.2.1 Decay Rate and Beam Profile Simulation

Since McStas uses ray-tracing to calculate neutron paths and includes the ability to calculate the behavior of neutron mirror guides, it gives a more accurate prediction of the neutron beam shape and intensity than MCNP. The probability of a neutron decaying within the fiducial volume is inversely proportional to the velocity as $\frac{1}{v}$. To account for this, the neutron flux intensity is binned by wavelength. A grid of virtual monitors placed across the decay volume in the simulation gives position binning. The flux is then normalized by the thermal neutron wavelength (1.8 Å) to get the capture flux, and then divided by the thermal neutron velocity (2200 m/s) and neutron lifetime (880.2 s) to get the decay rate density. Each tile has a volume scaled by the length of the center point along the beam that is used to calculate

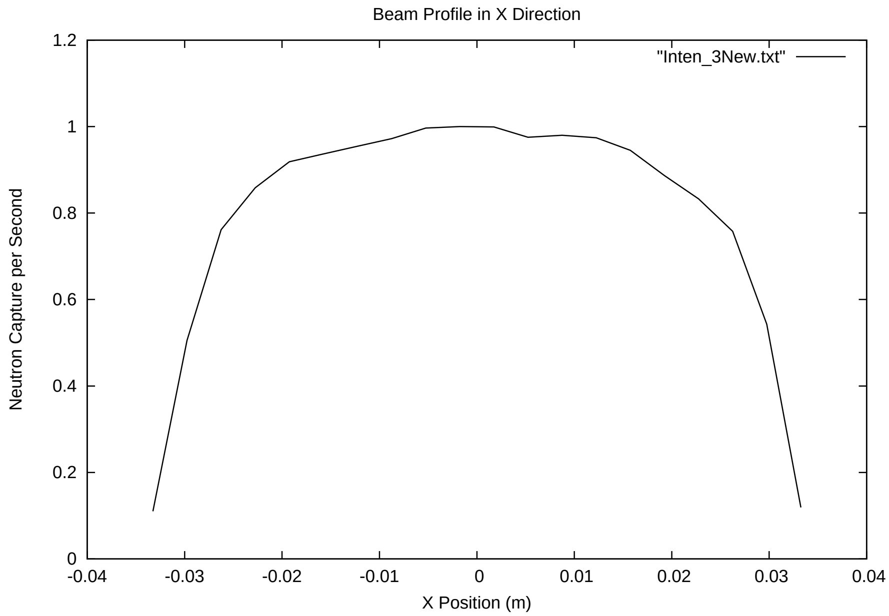

(a) Preliminary Profile

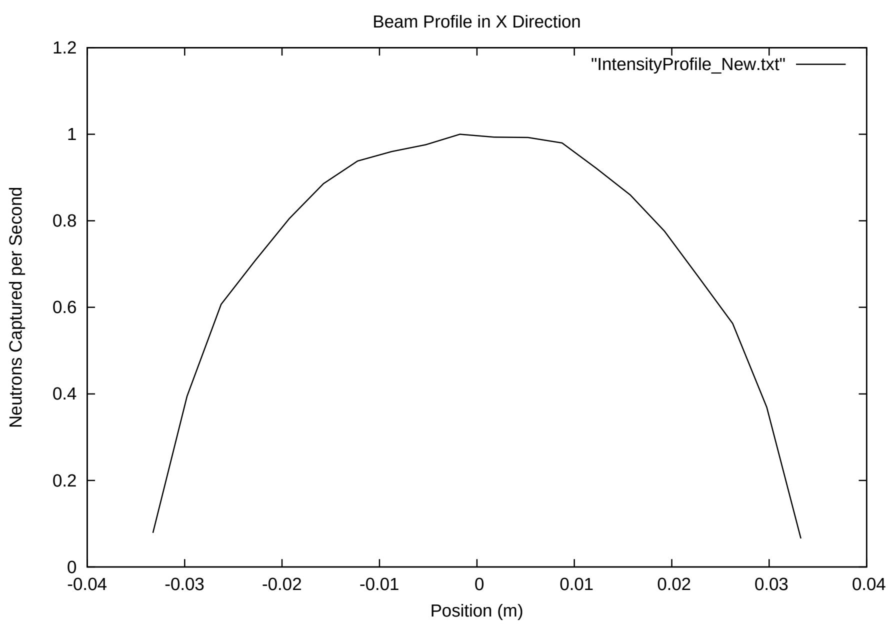

(b) Tapered Guide Profile

Figure 3.3: Normalized Beam Profiles. This shows the contrast between the tapered guide and a normal collimated beam. The focusing of the tapered guide creates a steeper beam edge.

the total decay rate per tile. Summing over the vertical bins gives the profile of the neutron beam, while summing over all bins will give the total decay rate.

3.2.2 Detector Backgrounds and Dose Rate Simulation

MCNPX is more appropriate for modeling material interactions with neutrons due to its large library of neutron scattering and capture reactions. For this model, the background rate is calculated by treating the Si detectors as cylindrical disks. The reaction rate of a photon or neutron is calculated by measuring the track length of the particle through the cell volume and multiplying it by the atomic density of the silicon and the cross section of the particle in the material. The resulting time-averaged singles reaction rate is binned from 30-780 keV, the energy range which would produce a false coincidence event.

This analysis of the detector backgrounds is additionally beneficial for studying general radiation safety limits. The SNS requires that non-radiation areas have doses of 0.25 mrem/hr or less in order to comply with the public annual dose limit of 100 mrem/year. The same calculations that are used to design shielding for the detectors are used to design general shielding for personnel safety, and the SNS constraints were a major part of the final design.

3.2.3 Geometry Modeling and Materials

An ideal neutron shield would absorb all neutrons with no secondary penetrating radiation, such as ^{3}He. However, ^{3}He is impractical to use in large amounts. Instead, compounds of boron or lithium 6 are commonly used for shielding neutron radiation and are the main

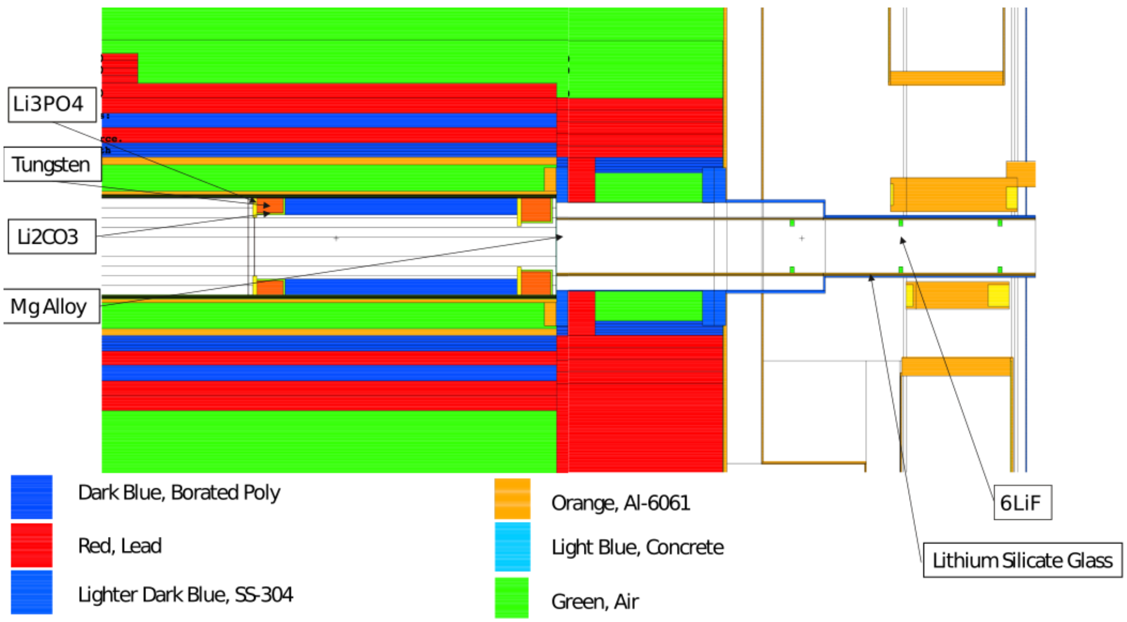

Figure 3.4: Nab Collimation and Shielding. The lithium collimators are backed by tungsten and borated polyethylene to shield gammas and fast neutrons along the beam. The surrounding shielding consists of alternating layers of lead and borated polyurethane.

neutron shielding materials used in Nab. For boron, the main thermal neutron capture reaction is $^{10}\mathrm{B}(n,\alpha)^{7}\mathrm{Li}^{*}$ which emits a 478 keV photon in 92% of captures. The majority of the boron in Nab is present in borated polyethylene, BPE. The hydrogen present in BPE moderates neutrons while the boron captures them. The main disadvantage of BPE is the presence of high energy gammas produced from the neutron capture in boron. In contrast, the lithium reaction, $^{6}\mathrm{Li}(n,\alpha)^{3}\mathrm{H}$, produces no gammas. It does, however, have a secondary reaction induced by the triton with a branching ratio of 10^{-4}, which produces fast neutrons up to 16 MeV. The collimators for the Nab beam are made of ^{6}Li compounds, such as Li_3PO_4, Li_2CO_3, and LiF.

For these reasons, lithium and boron compounds are used differently in shielding. Lithium compounds are best for initial shielding and collimation, as the absorption of neutrons in lithium is much more efficient and avoids producing gammas. This is important in areas that cannot be shielded by lead or stainless steel, such as the interior of the magnet. However, the production of secondary fast neutrons can create difficulties. Though this reaction is comparatively rare, the fast neutrons are emitted isotropically from the lithium and can capture on the surrounding material. Any collimation design must account for the dose and background rate due to these secondary neutrons.

The BPE is useful for additional shielding of the fast neutrons. For example, the small fraction of neutrons that make it past the lithium will either be moderated or captured by the BPE. The gammas produced by the capture can then be shielded with lead or stainless steel. A very effective method is to alternate layers of BPE and lead. The fast and thermal neutrons will be moderated or captured. The gammas produced from the neutron capture will be shielded by the lead, and the moderated neutrons will proceed to the next layer of

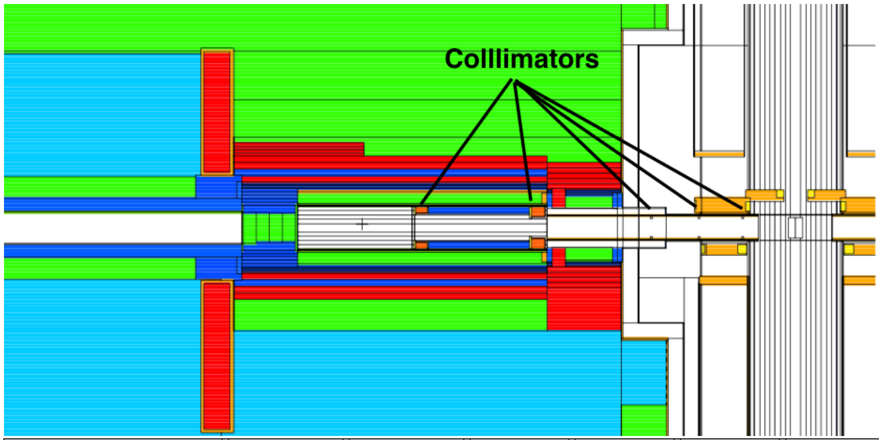

Collimator	C1	C2	E1	E2	E3	A1
Position (cm)	-148.0	-102.9	-55.8	-37.2	-20.2	place
Height (cm)	10	7	7	7	7	place
Width (cm)	8.4	6.4	6.4	5.4	5.4	place

Figure 3.5: The final collimation design. Three collimators are within the vacuum of the magnet and two are in the beam line before entering the magnet.

BPE where they are then captured. This is effective for gradual attenuation of the radiation if there is adequate space for the shielding.

3.3 Final Shielding and Collimation Results

The final collimation design consists of six collimators. Two of these are made of Li_3O_4P, which has a higher ^{6}Li number density in comparison to Li_2CO_3 which is suspended in a silicon based material. These are placed before the entrance window to the magnet and supported by a tungsten ring that acts as a collimator for any gammas from the neutron beam line. The rest of the collimators are within the magnet bore and under vacuum, which requires they be made of ^{6}LiF. The first three are before the decay volume and reduce the beam to a size of 7 cm in height and 6 cm in width with a decay rate of $\approx 2000\,$Hz, as can

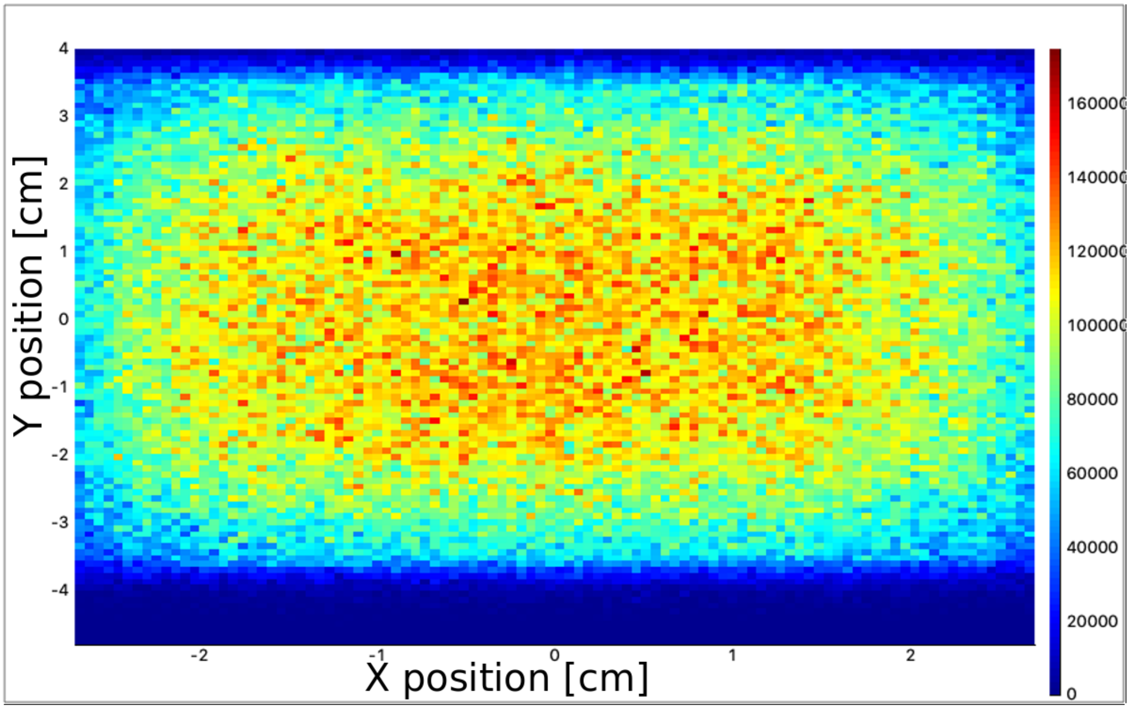

Figure 3.6: Beam Profile Intensity Plot. This is a cross section of the decay volume, showing an unnormalized position dependent intensity.

be seen in Figure 3.6. A final collimator is placed after the decay volume before the magnet exit window for the purpose of reducing the beam size as it exits the magnet.

The main sources of radiation are scattering from the collimators, from air before the spin flipper, and from the magnesium windows of the magnet vacuum. The initial neutron radiation is shielded first by a Li_2CO_3 layer lining the beam, then alternating stacks of borated polyethylene and lead outside of the beam. This is done to properly attenuate fast neutron radiation, as discussed in subsection 3.2.3. Beyond the sandwiched layers, blocks of lead are stacked around the windows and the air pocket to shield gammas. The roof of the experimental cave has a 1 m^2 hole in the shielding to accommodate the magnet. By

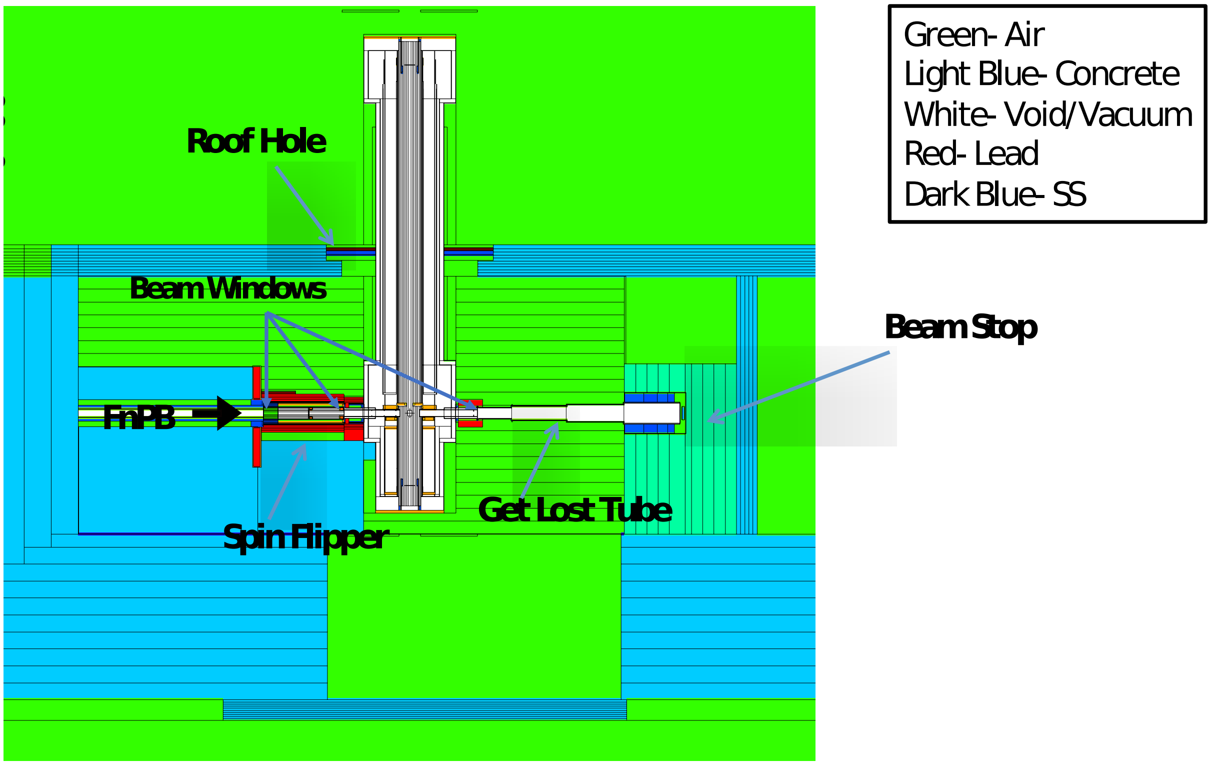

Figure 3.7: Current Nab Geometry. The FNPB emits neutrons along the horizontal axis. Decays are observed in the intersection between the beam and the spectrometer. Remaining neutrons are stopped in the beam stop, which is heavily shielded with concrete.

preemptively shielding the radiation immediately surrounding the beam, the dose in non-radiation worker areas has been kept under the required 0.25 mrem/hr limit. This can be seen in the contour plot in Figure 3.8.

The detectors see a total background singles rate of $\approx 2200\,\mathrm{Hz}$, which is on the order of a one-to-one ratio with the decay rate of $\approx 2000\,\mathrm{Hz}$. The background energies of concern are within the 30-752 keV window, which reduces the final background singles rate to $\approx 2150 Hz$. This can be seen in Figure 3.9.

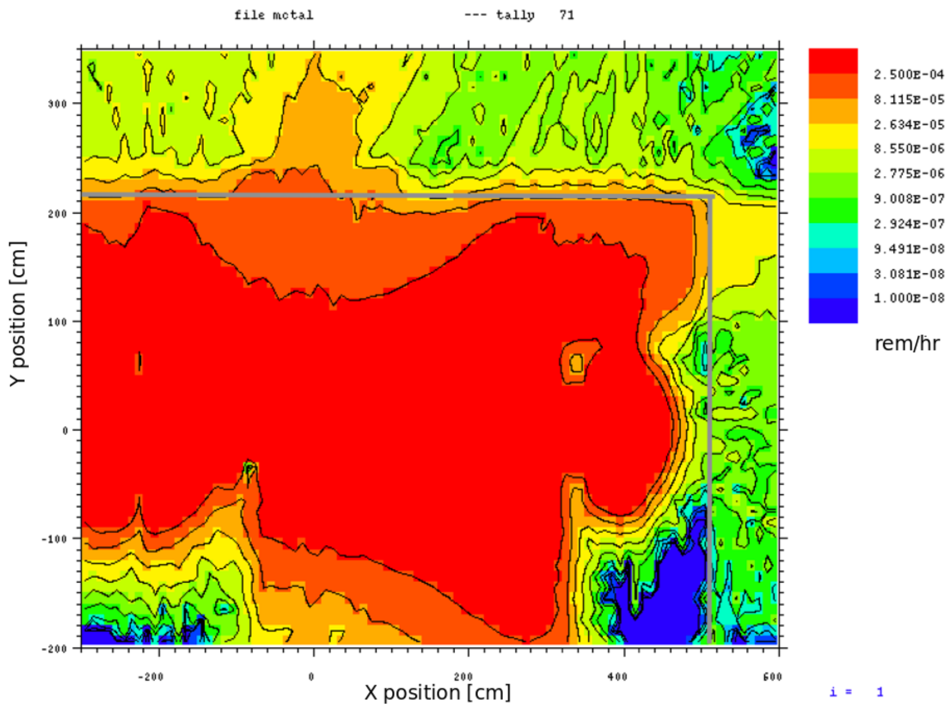

(a) Cold Gamma Dose Rate

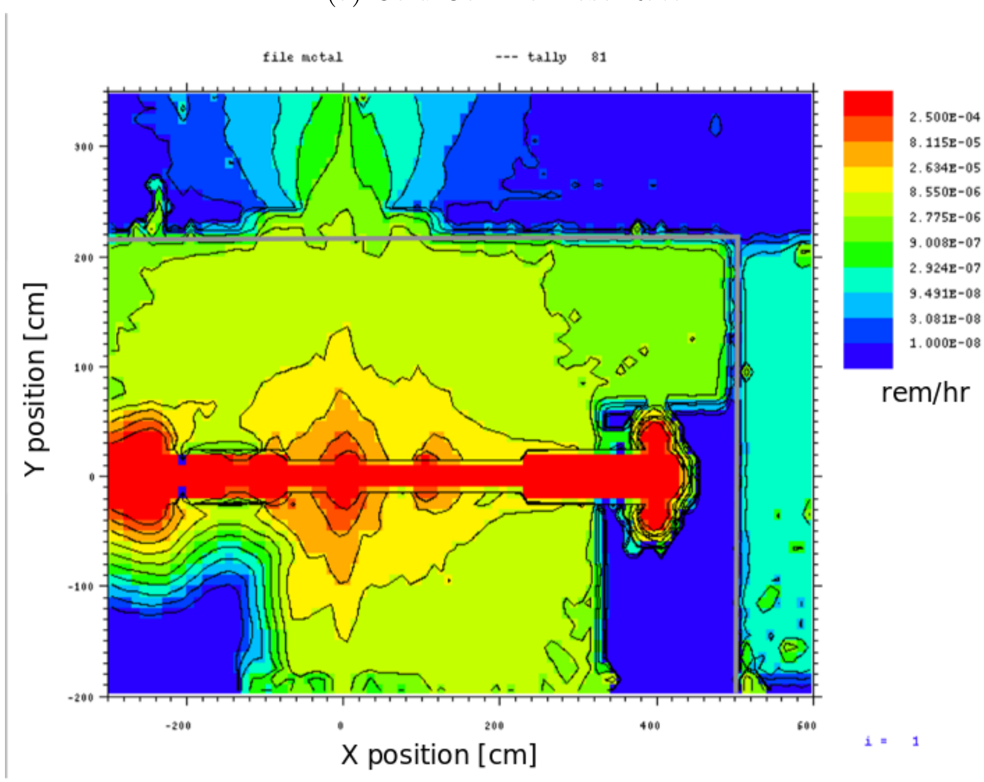

(b) Cold Neutron Dose Rate

Figure 3.8: Cold Beam Dose Rate Plots for Nab. The grey lines indicate the experimental cave boundaries. Contours describe rem/hr at a 2 MW beam. The red indicates that the dose is higher than the 0.25 mrem/hr limit required by the SNS.

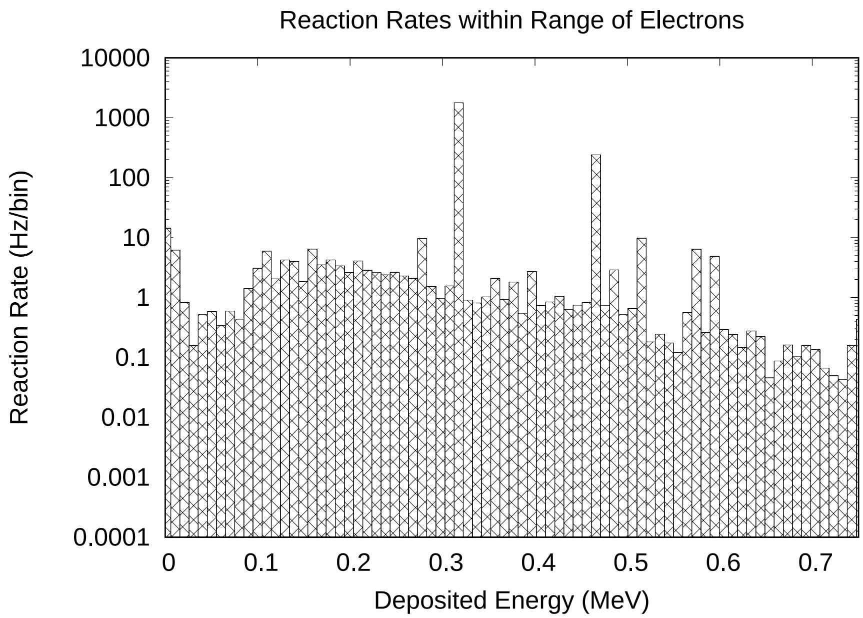

(a)

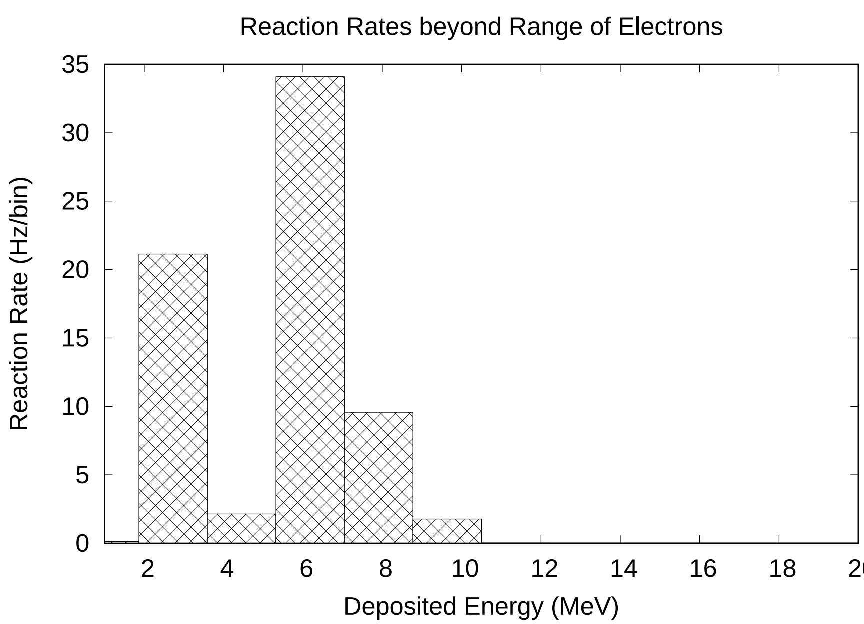

(b)

Figure 3.9: Detector backgrounds a) within the range of the electron energies binned by 10 keV, and b) outside of the range of electron energies binned by 1.7 MeV.

Chapter 4

Mapping the Nab Spectrometer Field

4.1 The Nab Spectrometer

As discussed in chapter 2, the Nab spectrometer has a complex magnetic field design consisting of a decay region, a sharp increase in magnetic field called the "filter", and a long time of flight region at low field. With this designed field, the observed proton time of flight is related to the initial decay proton momentum, p_0, by

$$t_p^2 = \frac{m_p^2 L^2}{p_\parallel^2} = \frac{m_p^2 L^2}{p_0^2 - \frac{p_0^2}{T_0} e(V - V_0) - \frac{B}{B_0} p_0^2 \sin^2\theta_0} = \frac{m_p^2}{p_0^2} \left[\int \frac{dl}{\sqrt{1 - \frac{e(V-V_0)}{T_0} - \frac{B}{B_0}\sin^2\theta_0}} \right]^2 \quad (4.1)$$

This is written as a square due to the squared proton momentum dependent yield that is the basis of the analysis, see Equation 2.5. The presence of the $\frac{B}{B_0}$ term indicates that a detailed understanding of the magnetic field along the proton flight path is critical. As seen in Table 2.1, the significant uncertainties arise with the curvature of the filter peak "pinch" and the ratios of the field at the filter peak with respect to the time of flight region and the decay volume. Furthermore, the flight path of a proton depends on the initial position of the neutron decay and the initial direction of the proton momentum. For example, a proton that decays in the center of the decay volume will follow a shorter path length than that of a proton that starts near the decay volume edge. A complete mapping of the magnetic field must cover the entire range of possible proton flight paths.

4.2 Challenges in Mapping the Magnetic Field

With these requirements, a careful mapping of the magnetic field is needed to reach the goal of measuring a to 10^{-3} uncertainty. However, some design features of the magnet create difficulties in accessing the field for measurement, as can be seen in Figure 4.1. The unique design and large range of field strengths requires that the magnet be a series of superconducting solenoids, kept at cryogenic temperatures. The bore containing the flight path for the decay particles must also be kept under vacuum, and runs at a temperature of about 70 K. The coil forming the filter peak of the field constricts the size of the inner bore to a diameter of about 4 cm, and the time of flight region gives the magnet a length of about 7 m. This design results in a long, thin cold mapping region under vacuum in which the field strength must be known to 10^{-3} uncertainty and the field position must be known within tens of microns. The wide range of field strength is measured using a transverse Hall probe, which has an operating temperature range of 0 °C to 50 °C. This creates an issue in measuring the magnetic field. To accurately map the field, the mapping must take place with the spectrometer in the same state as when performing the a measurement. Yet the Hall probe must be at room temperature and at atmospheric pressure to operate.

4.2.1 Accessing the Magnetic Field

This was solved by creating an *inverted vacuum dewar*. An aluminum tube wrapped in mylar superinsulation was inserted into the bore and sealed at both ends. This creates a room temperature port open to atmosphere while the magnet itself is under vacuum. This design can be seen in figure Figure 4.2b. The filter pinch is accommodated by forming the dewar out of two aluminum tubes, one 15 cm in diameter and one 4 cm in diameter, that are joined by an indium vacuum seal.

4.2.2 Precise Measurement of Field and Position

The field strength in the Nab spectrometer ranges from 0.001 - 4.2 Tesla and the critical fields arise in small, hard to access regions (specifically, the filter pinch is space-restricted to about 2 inches in diameter). A Hall effect probe was used to measure the magnetic field. This has two advantages over other sensors such as flux gates: the sensor can be calibrated over a large range of field strength, and the sensor can be small and flat. This type of probe is ideal for measuring a wide range of fields in a constrained space.

The Hall probe must first be calibrated before mapping. This has been done by to an uncertainty of 10^{-4} using an NMR probe and 5 Tesla magnet at Jefferson Laboratory. The Hall sensor and NMR probe are placed in a rigid structure with a known offset inside the

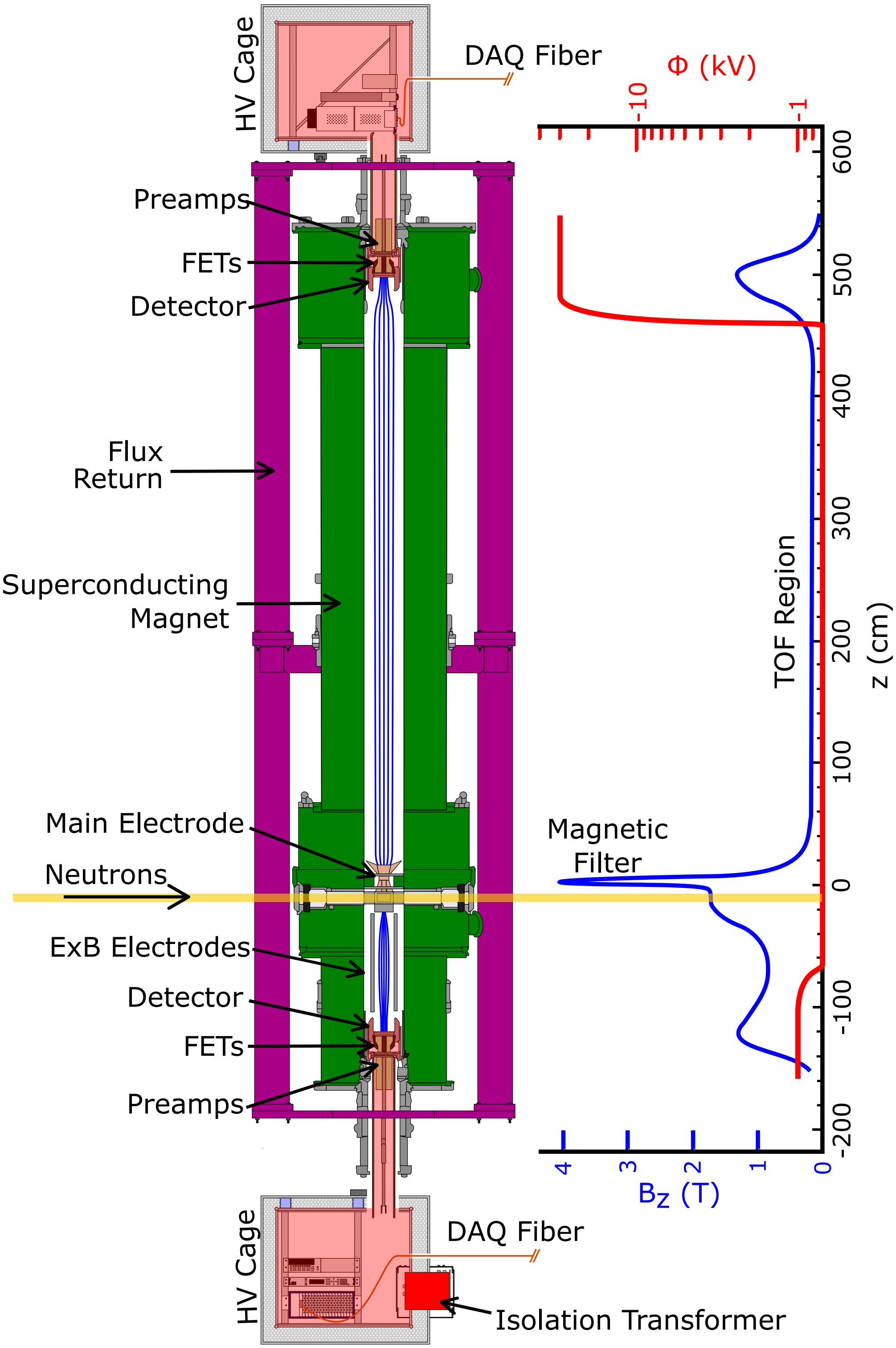

Figure 4.1: Diagram of the Nab Spectrometer, courtesy of A. Jezghani

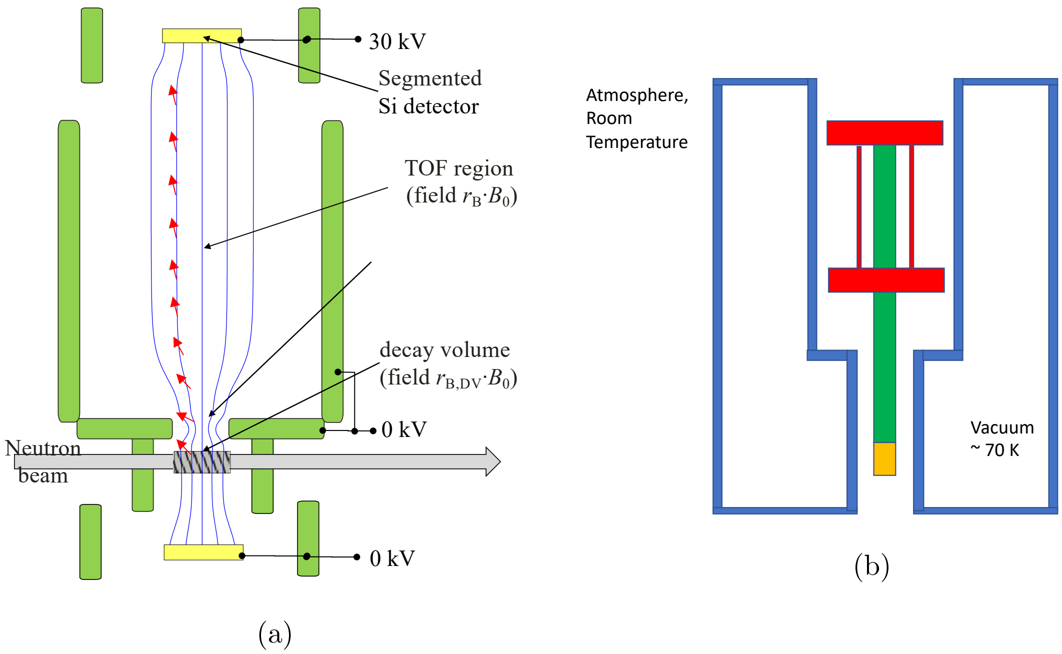

Figure 4.2: a) A cartoon showing the field and proton longitudinalization with respect to the neutron beam. b) A diagram showing the dewar situated inside the magnet with the access trolley that holds the Hall probe inside it.

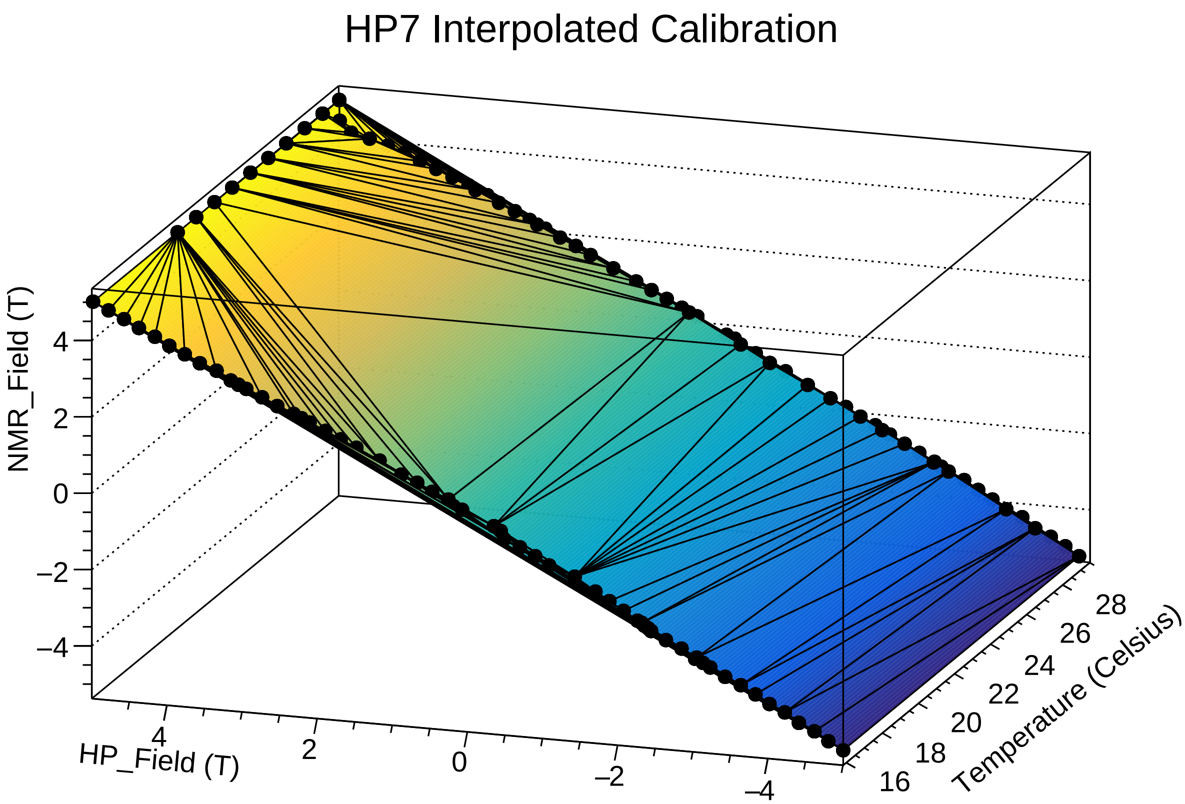

Figure 4.3: Interpolated calibration curve for a Hall probe. This was done over a range of -5 to 5 Tesla and a range of 15 C to 28 C in temperature.

5 Tesla magnet, which is uniform. By measuring the field in both probes over a range of strengths and temperature, a calibration curve can be created, as seen in Figure 4.3.

The main difficulty in the Nab field calibration lies in the accurate determination of the position of the sensor. The volume accessible via the dewar is long and thin and difficult to navigate, yet the position must be known to tens of microns. This measurement is achieved by using a Leica AT401 Absolute Tracker.

The principle use of a laser tracker is to map three dimensional coordinates by using a tracking laser on a target. The target itself is a spherically mounted retroreflector (SMR);

this has a reflective "corner" inset placed such that any light reflection from any angle will have a path length that corresponds to the center of the sphere. The tracker then uses either laser interferometry or absolute distance measurement (ADM) to precisely measure the distance to the center of the SMR, and two angle encoders measure the azimuthal and elevation angles.

The AT401 uses ADM instead of interferometry, meaning that the emitted laser light is reflected from the SMR back to the tracker and the distance is calculated from the time taken to reflect. In contrast, a laser interferometer measures the distance by splitting the laser into two paths; one to the SMR and one to the tracker itself. The advantage of using an ADM tracker is that the beam sight can be broken and reconnected without having to re-home the SMR on the tracker. With this tracker, the positions of the SMR can be found and measured as long as there is a direct line of sight. This measurement is accurate to tens of microns. Additionally, the tracker includes a precision azimuth and zenith angle encoder. Thus tracker data can give the position of the SMR in three dimensional coordinates.

The next step is to create a structure that connects the Hall probe sensor and the SMR, while allowing the Hall probe to be placed in the crucial measurement areas. This is done by constructing a trolley that can be raised and lowered throughout the dewar. As can be seen in Figure 4.2b, the trolley consists of two plates with wheels that rigidly hold a long aluminum tube or nose that can fit into the smaller section of the dewar along the dewar axis. The Hall probe is placed in a 3D printed structure attached to the end of the nose. The entire structure can be raised and lowered throughout the dewar, with different sections accessed by interchangeable *noses*.

Four SMRs are placed at various points on the top plate of the trolley and a single SMR is placed on the bottom. By using two laser trackers, one aimed from above and the other aimed from below, the trolley height, clocking, and tilt can be entirely characterized. The offset between the SMR probe centers and the position of the Hall probe sensor is measured each time the rigid structure is made via a laser tracker bench measurement.

4.2.3 Aligning the Probe to the Field

A final difficulty arises in aligning the Hall probe to the field. As will be discussed in the next chapter, a full expansion of the field only requires measuring the magnitude of the field, not the components. However, that is not an insignificant challenge. While for low fields, a three axis Hall probe would easily give both magnitude and direction of the field, higher field strengths give rise to the planar Hall effect.

The planar Hall effect occurs when the magnetic field is not perpendicular to the plane of the probe. An error appears that is proportional to the square of the field parallel to the probe and maximizes at an angle of 45°. This effect is negligible for low fields, but as both the field strength and angle of the probe increase, the error becomes significant, as can be seen in Figure 4.4.

To avoid this error, the Hall probe is made to align with the magnetic field before taking a measurement. This is done by taking advantage of the cylindrical symmetry of the solenoids. Say the field is described in cylindrical components, B_Z, B_ρ and B_ϕ, where the z axis is aligned with the magnet axis. On axis, where $\rho = 0$, the field is entirely within the z component.

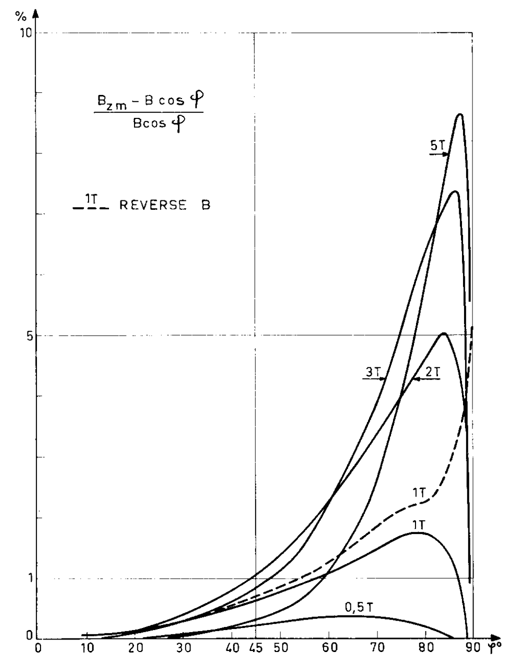

Figure 4.4: Error in perpendicular component of field due to the planar Hall effect [49]. Components of fields with magnitudes greater than 1 Tesla cannot be precisely measured.

For on axis measurements, the probe can be placed flat and perpendicular to the magnet axis to directly measure the field magnitude.

This changes if taking data off axis. Assuming cylindrical symmetry allows that $B_\phi = 0$, so the entirety of the fields off axis are in B_Z and B_ρ. By tilting the probe radially until the field is maximized, the magnitude of the field can be found, but this must be done over a distance up to 4 meters.

This problem is solved by designing a *tilt table*, which can be maneuvered over a distance of 6 meters. As seen in Figure 4.5, this structure holds the probe sensor at a rotational axis at some radius ρ. The table holding the sensor is tilted radially from a distance using two Kevlar strings inside Teflon tubing. By alternating the string tension, the table can be tilted in a range of 20° about the perpendicular plane. The controller for the Hall probe can hold a peak field, so by slowly tilting the table one can maximize the field and find the magnitude. This particular design is the result of many 3D printed test iterations.

4.3 Measurements

The full mapping of the Nab spectrometer field consists of five types of measurements:

1. **On axis scans**: performed by placing the Hall probe in a stationary probe holder that is raised and lowered via the trolley along the axis. This type of scan is performed along the entire length of the magnet and repeated with the trolley rotated at several orientations in ϕ.

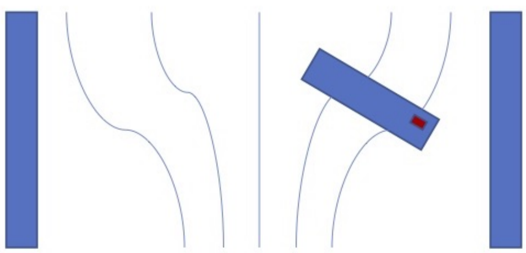

(a)

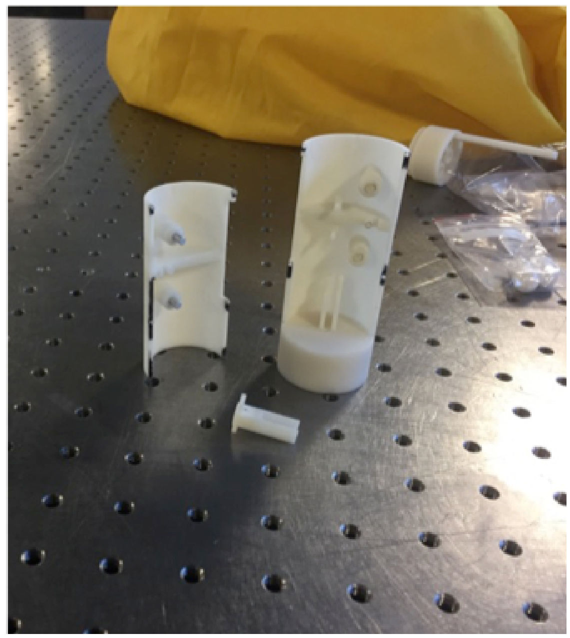

(b)

Figure 4.5: a) Diagram showing the principle of the tilt table for a cylindrically symmetric field. The red box is the sensor of the probe. b) Off Axis Hall probe holder, version 15. Rapid prototyping via 3D printing allows for fast optimization of the tilt table design.

2. **Near off axis scans**: performed by using the *tilt table* holder at the end of the nose. These measurements are taken at a 2 cm radius and the scans are performed at several different ϕ orientations along the entire magnet.

3. **Far off axis scans** performed by placing the *tilt table* holder at a radius of 10 cm on the trolley and performing scans at different ϕ orientations in the time of flight region of the magnet.

4. **Tilted far off axis scans** performed by using a modified version of the *tilt table* holder where the Hall probe was rotated by 10° in ϕ. This is done to compare to the normal far off axis scans and check for B_ϕ fields.

5. ϕ **scans** performed by setting the near off axis set up at constant z and ρ and taking multiple points in ϕ. This is done about the filter peak, the decay volume, detector peaks, and time of flight region and is used for checking cylindrical symmetry.

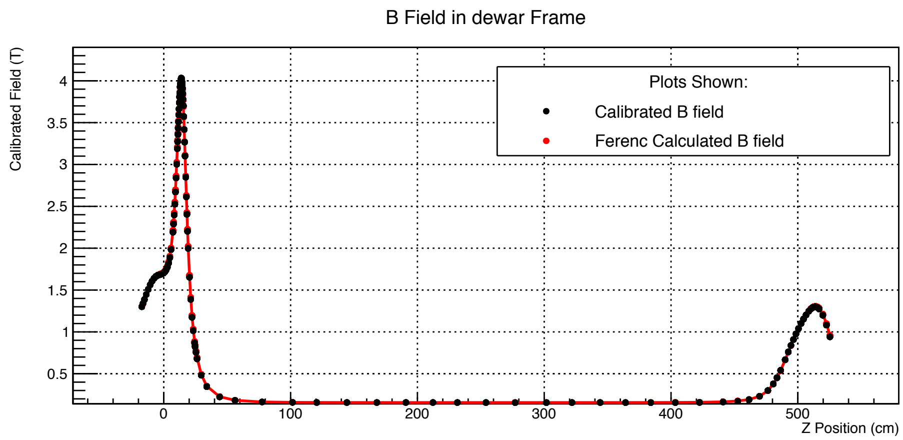

(a) All on axis points measured, compared to theoretical design of field, called Ference field.

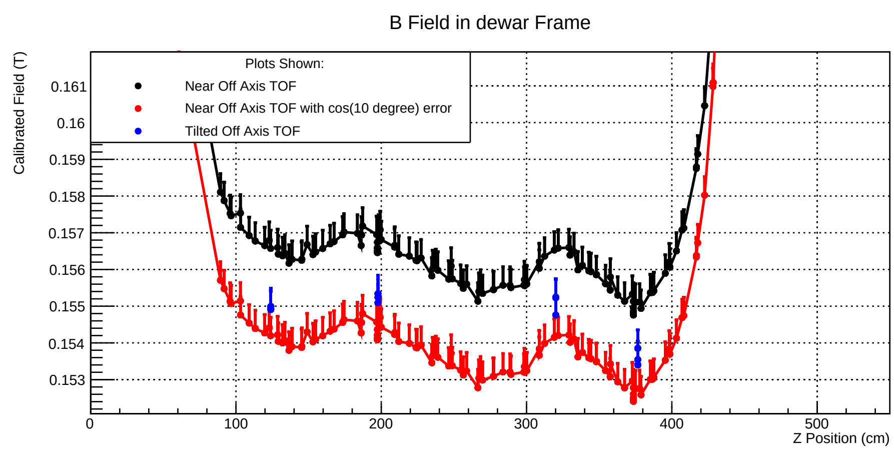

(b) Comparison of normal off axis scan to tilted off axis scan. Indicates that there is little to no B_ϕ field present in the time of flight region. This is important because non cylindrically symmetric fields will be most evident in the TOF region.

Figure 4.6

Chapter 5

Magnetometry Analysis

The mapping techniques used in chapter 4 can only access the region of the spectrometer intersected by the dewar insert, therefore a thorough analysis of the data must be performed in order to create an expansion of the magnetic field over the entire flight path region. Since the spectrometer consists of a series of solenoids and can be assumed to be cylindrically symmetric, the mapping of the on-axis field contains all information needed for such an expansion. The most direct method utilizes a radial series expansion of the on-axis field, where

$$B_z(\rho, z) = B_z(\rho = 0, z) - \frac{1}{4}\rho^2 \frac{\partial^2 B_{0,z}}{\partial z^2}\bigg|_{(\rho=0,z)} + ... \tag{5.1}$$

$$B_\rho(\rho, z) = -\frac{1}{2}\rho \frac{\partial B_{0,z}}{\partial z}\bigg|_{(\rho=0,z)} + \frac{1}{16}\rho^3 \frac{\partial^3 B_{0,z}}{\partial z^3}\bigg|_{(\rho=0,z)} + ... \tag{5.2}$$

This expansion is complete, but requires a mapping detailed enough to calculate up to the third derivative of the on-axis field. In contrast, this chapter will discuss a method that uses the modified Bessel functions as the basis functions. The advantage of this is that all information of the derivatives from the radial expansion is included in the modified Bessel function, as will be shown in subsection 5.1.2.

5.1 Modified Bessel Function Expansion

Maxwell's equations in a space free of current (such as the interior vacuum of the spectrometer) describe the scalar magnetic potential, which can be written as a solution to Laplace's equation

$$\vec{H} = -\nabla\Phi \rightarrow \nabla^2\Phi = 0 \tag{5.3}$$

By writing the Laplace operator in cylindrical coordinates and assuming cylindrical symmetry, this equation reduces to

$$\frac{1}{\rho}\frac{\partial}{\partial\rho}(\rho\frac{\partial\Phi}{\partial\rho}) + \frac{\partial^2\Phi}{\partial z^2} = 0 \tag{5.4}$$

A separation of variables gives rise to two independent differential equations, connected through some constant k, treated as a wavenumber. Thus their solutions at each value of k follow as

$$\frac{\partial^2 Z}{\partial z^2} = -k^2 Z \quad \rightarrow \quad Z(z) = a_1\sin(kz) + a_2\cos(kz) \tag{5.5}$$

$$\rho^2\frac{\partial^2 R}{\partial\rho^2} + \rho\frac{\partial R}{\partial\rho} - k^2\rho^2 R = 0 \quad \rightarrow \quad R(\rho) = b_1 I_0(k\rho) + b_2 K_0(k\rho) \tag{5.6}$$

Since in the modified Bessel function of the second kind, $K_0(\rho)$ blows up as $\rho \to 0$, the constant b_2 is set to zero to remain physical. Summing over all possible solutions, k, and combining coefficients, Φ becomes

$$\Phi(\rho, z) = \sum_{k=-\infty}^{\infty} I_0(k\rho)\Big[c_k \sin(kz) + d_k \cos(kz)\Big] = \sum_{k=-\infty}^{\infty} I_0(k\rho) f_k e^{ikz} \tag{5.7}$$

$$f_k = \begin{cases} \frac{1}{2}(c_k - id_k) & k > 0 \\ \frac{1}{2}c_0 & k = 0 \\ \frac{1}{2}(c_k + id_k) & k < 0 \end{cases} \tag{5.8}$$

and the fields are subsequently

$$B_z(\rho, z) = \frac{\delta\Phi}{\delta z} = \sum_{k=-\infty}^{\infty} ikI_0(k\rho) f_k e^{ikz} \tag{5.9}$$

$$B_\rho(\rho, z) = \frac{\delta\Phi}{\delta\rho} = \sum_{k=-\infty}^{\infty} kI_1(k\rho) f_k e^{ikz} \tag{5.10}$$

The advantage of using this expansion is how the field simplifies on the magnetic axis. Setting $\rho = 0$ for an on-axis field, the modified bessel functions reduce to $I_0(0) = 1$ and $I_1(0) = 0$ and the on-axis magnetic field becomes

$$B_z(\rho = 0, z) = \sum_{k=-\infty}^{\infty} ik f_k e^{ikz} = \sum_{k=-\infty}^{\infty} F_k e^{ikz} \tag{5.11}$$

$$B_\rho(\rho = 0, z) = 0 \tag{5.12}$$

The Fourier coefficients present in the on-axis expansion, F_k, are the same found in the off-axis B_z and B_ρ fields. In essence, the off-axis fields can be written in terms of the on-axis Fourier coefficients and modified Bessel functions, i.e.

$$B_z(\rho, z) = \sum_{k=-\infty}^{\infty} I_0(k\rho) F_k e^{ikz} \tag{5.13}$$

$$B_\rho(\rho, z) = \sum_{k=-\infty}^{\infty} -iI_1(k\rho) F_k e^{ikz} \tag{5.14}$$

In practice, finding the Fourier coefficients is achieved via a discrete Fourier transform, where the discretized variables with integers m and n are $z = m\delta z$, $k = 2\pi n/L$, and $L = \delta z N$ for N samples, making the on-axis field and its transform become

$$B_z(\rho = 0)[m] = \sum_{n=0}^{N-1} F[n] e^{i2\pi nm\delta z/\delta zN} = \sum_{n=0}^{N-1} F[n] e^{i2\pi nm/N} \tag{5.15}$$

$$F[n] = \frac{1}{N} \sum_{m=0}^{N-1} B[m] e^{-i2\pi nm/N} \tag{5.16}$$

with the off-axis Fourier coefficients corresponding to

$$F_z[n] = I_0(\frac{2\pi n\rho}{L})F[n] \rightarrow \quad B_z[m] = \sum_{n=0}^{N-1} F_z[n]e^{i2\pi nm/N} \tag{5.17}$$

$$F_\rho[n] = -iI_1(\frac{2\pi n\rho}{L})F[n] \rightarrow \quad B_\rho[m] = \sum_{n=0}^{N-1} -F_\rho[n]e^{i2\pi nm/N} \tag{5.18}$$

5.1.1 Wavenumber Contributions to the Fourier Transform

The Nab spectrometer is a stack of solenoid coils of varying sizes. The filter coil, which contributes the majority of the filter peak of the field, is the smallest of these, with a length of D = 28.7 mm. By approximating the on-axis field of the solenoid by a box function, one can show that the length of the solenoid creates a physical limit on the wavenumber contribution to the Fourier transform.

$$\mathscr{F}\{B(z)\} = b(k) = \int_{-\infty}^{\infty} B(z)e^{-ikz}dz = \int_{D/2}^{D/2} B_z e^{-ikz}dz = B_z D\frac{\sin(kD/2)}{kD/2} \tag{5.19}$$

At $k = 0 \rightarrow n = 0$, the peak wavenumber is

$$b(0) = B_z D\,\mathrm{sinc}(0) = B_z D \tag{5.20}$$

If one does a rough error approximation comparing the magnitudes of the Fourier coefficients, the wavenumber has a limit dependent on the length used in the transform

L and the solenoid length D.

$$err = |\frac{b(k)}{b(0)}| = |\,\mathrm{sinc}(nD/L)| \approx \frac{1}{nD/L} = \frac{L}{nD} \tag{5.21}$$

$$err \leq \epsilon \rightarrow \frac{L}{nD} \leq \epsilon \tag{5.22}$$

$$n \geq \frac{L}{D\epsilon} \tag{5.23}$$

This approximation demonstrates the known concept that rapidly changing functions will have higher wavenumber contributions. With the Nab spectrometer, the scale of variation D is about the length of the smallest coil (28.7 mm). The transform length L is interpreted as the distance along the z axis that is included in the FFT. A smaller D variation for a constant L will increase the number of wavenumbers needed to precisely fit the field to a discrete Fourier series. One can increase the distance along the axis that is used (say changing from [-100:100] mm to [-1000:1000] mm) to reduce the wavenumbers needed.

5.1.2 Limits on the Radial Contribution to the Magnetic Field

Another consideration is the behavior of the high wavenumber coefficients due to the modified Bessel function multiplication. If the modified Bessel function is treated as a separate function, then the off-axis field can be considered a convolution of the on-axis field and the inverse Fourier transform of the modified Bessel function. Performing this convolution shows

$$\mathscr{F}^{-1}[I_0(k\rho)] = \sum_{k=-\infty}^{\infty}\sum_{t=0}^{\infty}(\frac{1}{4})^t\frac{(k\rho)^{2t}}{(t!)^2}e^{-ikz} = \sum_{t=0}^{\infty}(\frac{1}{4})^t\frac{(-i\rho)^{2t}\delta^{(2t)}(z)}{(t!)^2} \tag{5.24}$$

$$B_z(\rho, z) = \mathscr{F}^{-1}[I_0(k\rho)F_k] = B_z(0, z) * \mathscr{F}^{-1}[I_0(k\rho)] \tag{5.25}$$

$$B_z(\rho, z) = \sum_{t=0}^{\infty}(\frac{1}{4})^t\frac{(-i\rho)^{2t}}{(t!)^2}\int B_z(0, z')\delta^{(2t)}(z-z')dz' \tag{5.26}$$

$$B_z(\rho, z) = \sum_{t=0}^{\infty}(\frac{1}{4})^t\frac{(-i\rho)^{2t}}{(t!)^2}\frac{\partial^{(2t)}}{\partial z^{(2t)}}B_z(0, z) \tag{5.27}$$

which is the radial series expansion. The modified Bessel function expansion is the natural cylindrically symmetric basis and includes all derivatives of the magnetic field within the transform of the modified Bessel function.

For the radial series to converge, the ratio of terms requires

$$\frac{a_{t+1}}{a_t} \approx \rho^2\frac{\partial^{(2t+2)}B_z(0, z)/\partial z^{(2t+2)}}{\partial^{(2t)}B_z(0, z)/\partial z^{(2t)}} < 1 \quad \text{for} \quad t \to \infty \tag{5.28}$$

which gives a requirement for the radius as

$$\rho < \sqrt{\frac{\partial^{(2t)}B_z(0, z)/\partial z^{(2t)}}{\partial^{(2t+2)}B_z(0, z)/\partial z^{(2t+2)}}} \approx \sqrt{\frac{B/D^{2t}}{B/D^{2t+2}}} = D \tag{5.29}$$

where D is the scale of the variation of the field, similar to the D solenoid length in the previous argument.

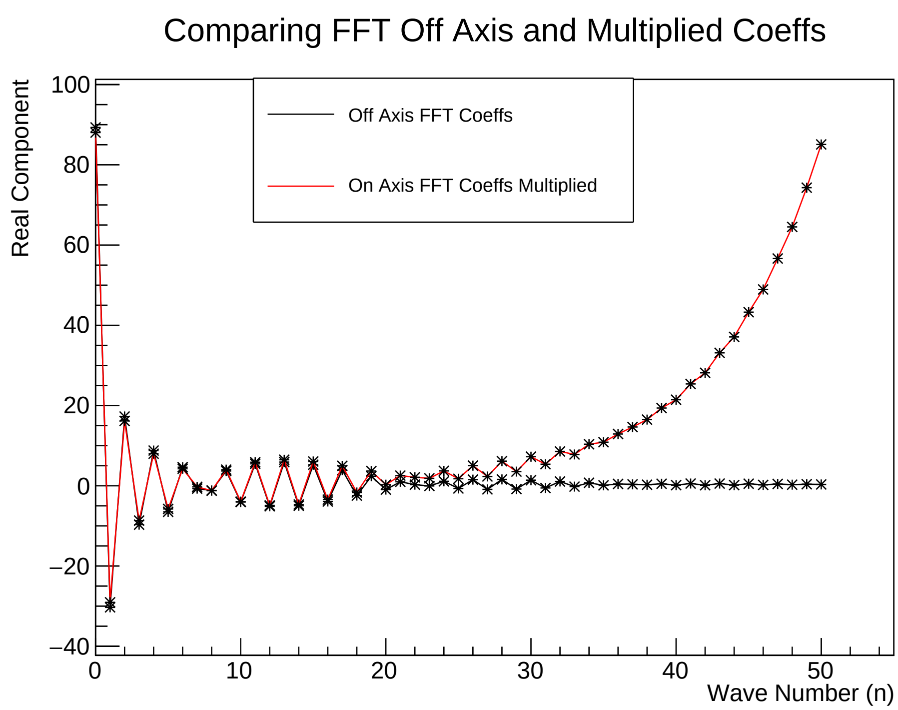

Figure 5.1: Off-axis transform high wavenumber behavior. Larger wavenumbers rapidly grow due to the modified Bessel function.

This effect can be demonstrated using a code that calculates the field based on the solenoid design. Both the on-axis and off-axis fields are found, then transformed. The on-axis Fourier coefficients are multiplied by the modified Bessel function, Equation 5.18, and compared to the directly transformed off-axis coefficients. As can be seen in Figure 5.1, the larger wavenumber coefficients diverge when multiplied by the modified Bessel function, which is dependent on ρ. This effect would be negligible for smaller ρ, but the variation change is the smallest solenoid length, $D = 28.7\,\text{mm}$, and this comparable to the largest radius needed at $\rho = 20\,\text{mm}$. Filtering the high wavenumber contributions can reduce this effect. Thus, the number of wavenumbers used must be balanced between reducing the modified Bessel function and adequately describing the field.

5.2 Fast Fourier Transforms of the Magnetic Field

All discrete Fourier transforms (DFTs) in this analysis are performed using the FFTW framework, an open source, optimized C library that allows for DFT calculations for real and imaginary multidimensional data. The magnetic field transforms are one-dimensional *real to complex* transformations when calculating the wavenumber domain, and use one-dimensional *complex to real* transformations when performing the reverse transformation. The initial analysis is performed on fake data, created via a C++ code that calculates the expected field produced by the solenoid design of the spectrometer.

A full field expansion that predicts the off-axis fields within 10^{-3} can be found using the full length of the field, as seen in Figure 5.2. This expansion, which covers a range of 11 m, has a step size of 2 mm and adds about 2 m of zero-padding to the ends of the field to mitigate aliasing effects. This expansion requires a filtering of frequencies higher than $\frac{N}{10}$, where N is the number of samples, in order to reduce effects from the modified Bessel function discussed previously.

Due to the nature of the mapping technique, a full on-axis field past the detectors is not available. Instead, the majority of the mapping data extends between the peaks of the detector fields, as seen in Figure 5.3. There is a small region between the lower detector and the decay volume where no mapping data could be taken due to the reach of our apparatus. This region is not needed to understand the spectrometer response function for proton time of flight, so the expansion can be trimmed of the lower detection field for this calculation.

By trimming the edges of the field, discontinuities are introduced. This creates a ringing effect due to the spectral leakage of the Gibb's phenomenon, as can be seen in Figure 5.4a. A Hann window, where the function is weighted as

$$w[n] = \frac{1}{2}\left[1 - \cos\left(\frac{2\pi n}{N}\right)\right] \tag{5.30}$$

can be used to smooth the function and reduce these effects, as seen in Figure 5.4b. Combining this windowing and a filter of higher wavenumbers, a transform over the trimmed data can provide an expansion good to 10^{-4}, as can be seen in Figure 5.4c.

With the high wavenumber filtering and the Hann window, the on-axis data presented in Figure 5.3 can now be used to find an expansion that predicts the off-axis field. This expansion can be compared to the real off-axis data taken from the mapping. The radius of this particular run has a mean of about 13 mm, seen in Figure 5.5a.

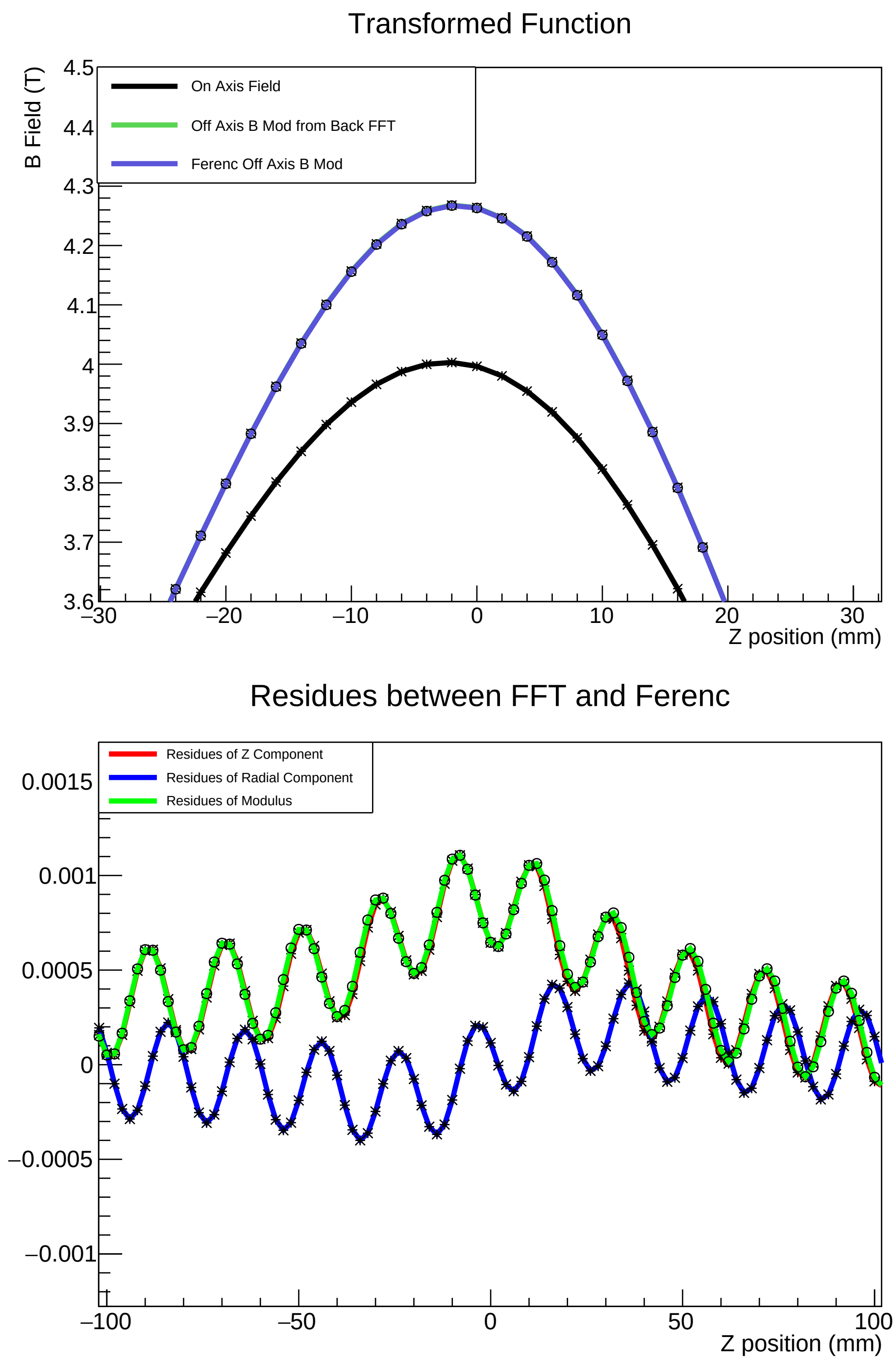

Figure 5.2: Transform and residues in the filter region for backwards FFT over full magnetic field and theoretical designed field. Oscilltions come from trimming the higher wavenumbers - there is some spectral leakage of the transform into the higher wavenumbers.

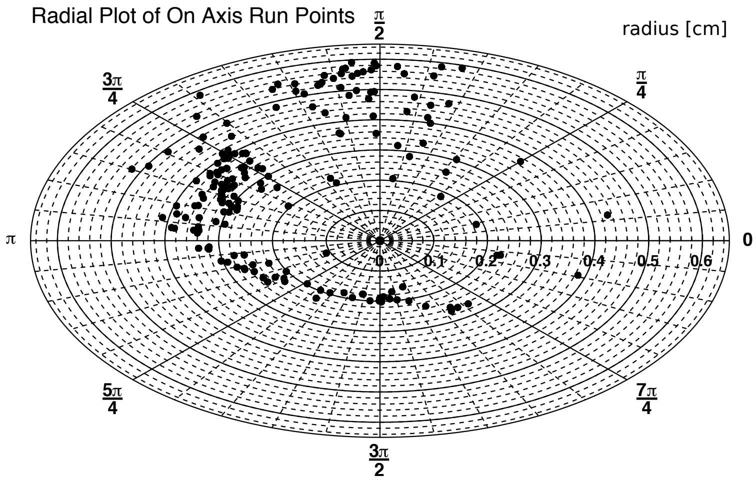

Figure 5.3: Plot of all collected on-axis data, the calibrated magnetic field vs the z position along the dewar axis.

When comparing the predicted off-axis field and the near off-axis data, it can be seen in Figure 5.6 that there is a shift in z between the two. If the predicted field is shifted by 8 mm in z, it agrees with the off-axis data within 10^{-2}. This indicates that there is likely some amount of tilt of the magnet coils with respect to the dewar axis. Thus, the on-axis data must be corrected to the frame of the magnet coil axis in order to give a true on-axis expansion.

5.2.1 Determining the Magnetic Axis

As discussed in chapter 4, there are five types of mapping measurements: on-axis scans, near off-axis scans, far off-axis scans, tilted far off-axis scans and ϕ scans. Due to complexity of the mapping, the Hall probe position can be precisely measured, but is not well controlled. This means that the data obtained is not directly on-axis; there is a small radial variation throughout the measurements, as seen in Figure 5.7. The off-axis maps behave similarly

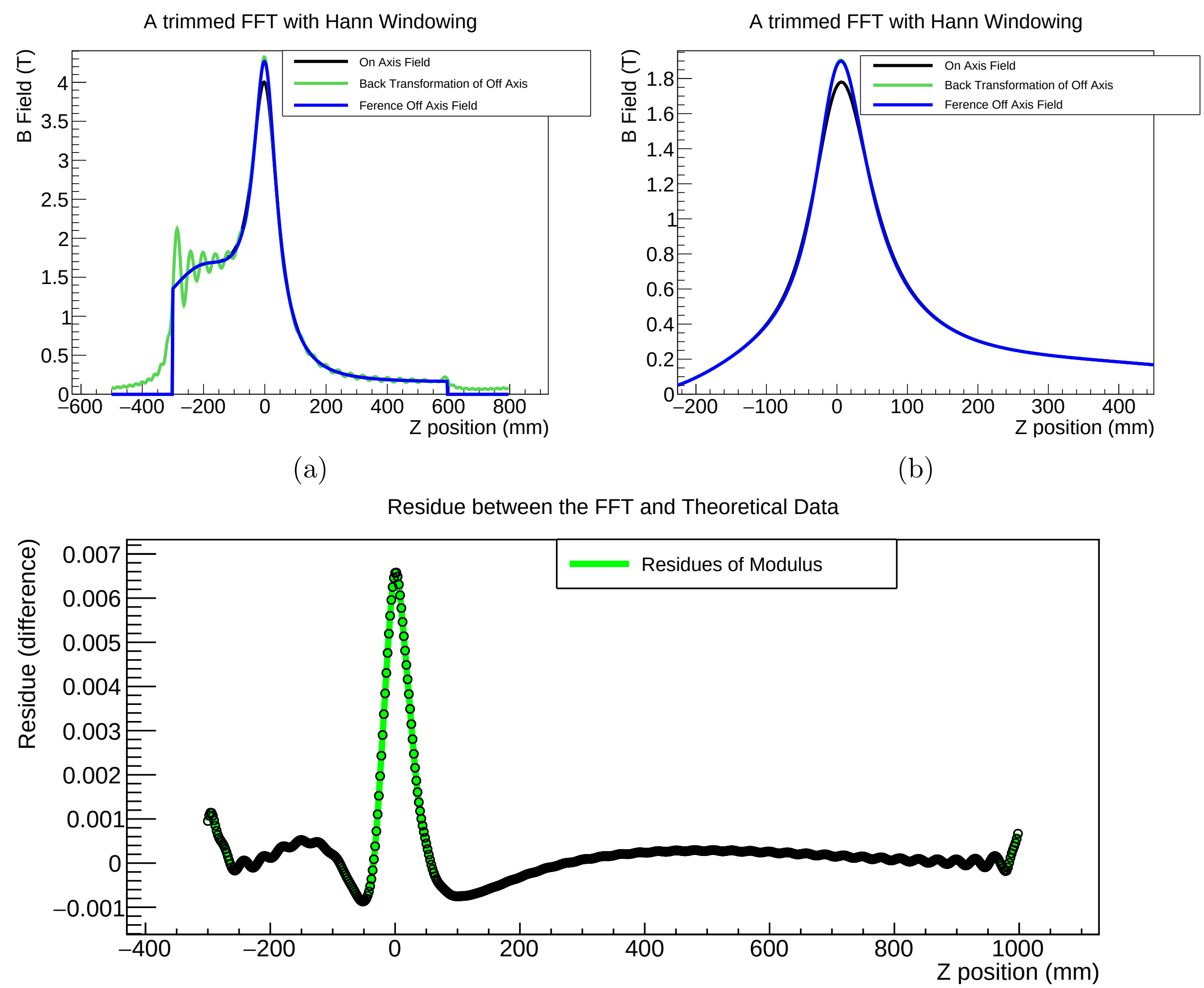

(a) (b)

(c)

Figure 5.4: Transforms of the trimmed magnetic field a) without windowing and b) with Hann windowing. The ringing at the discontinuity is eliminated. c) Shows the residues from the transform with Hann windowing. The previous oscillations seen from spectral leakage are reduced by the windowing function.

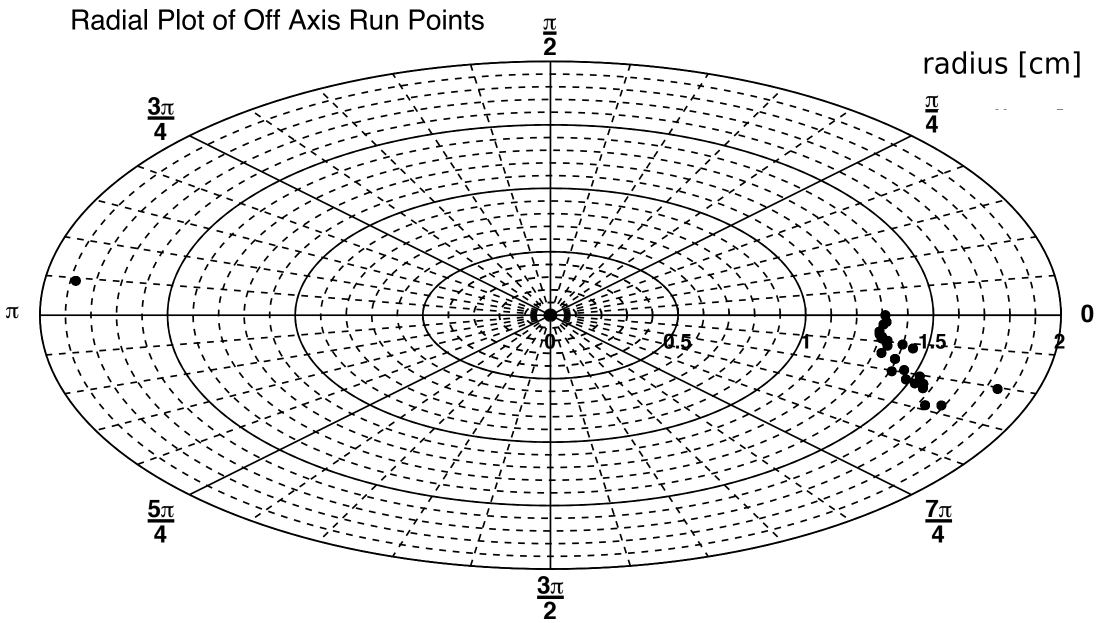

(a)

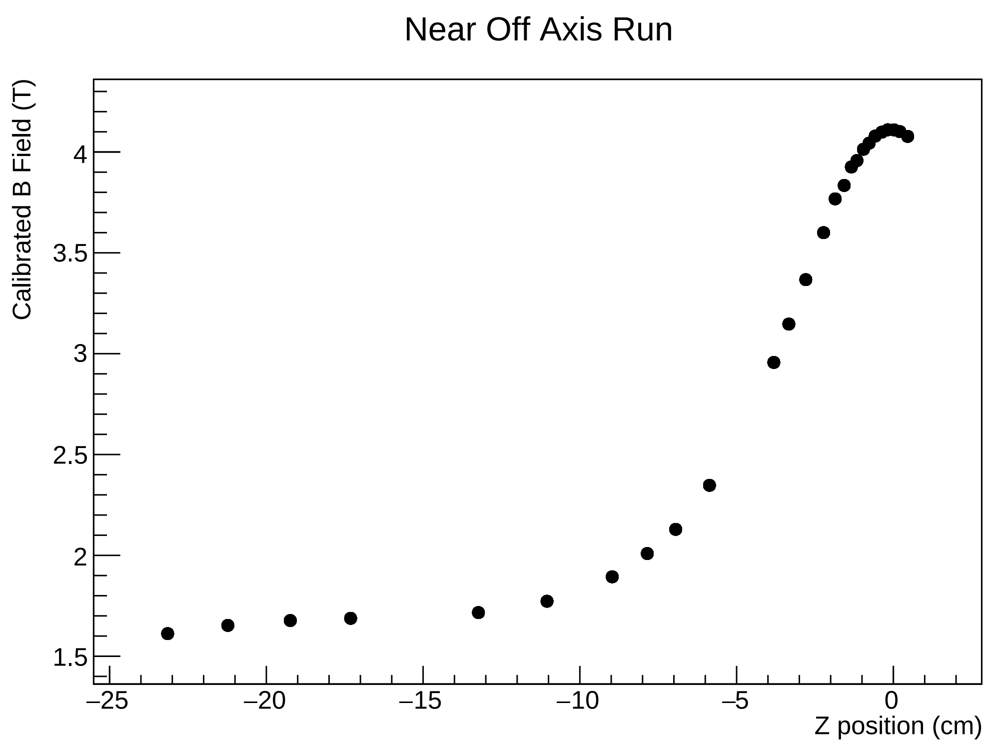

(b)

Figure 5.5: Plots of the position and the magnetic field for a single near off-axis run.

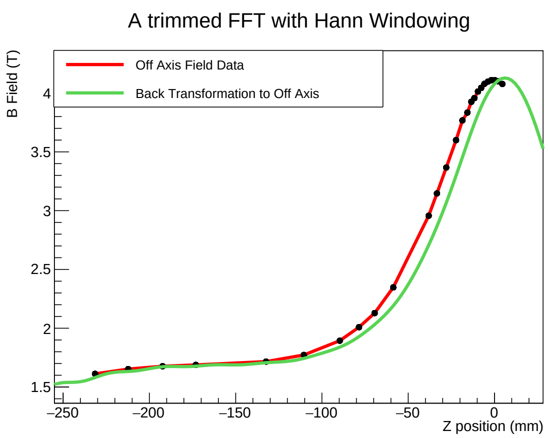

(a)

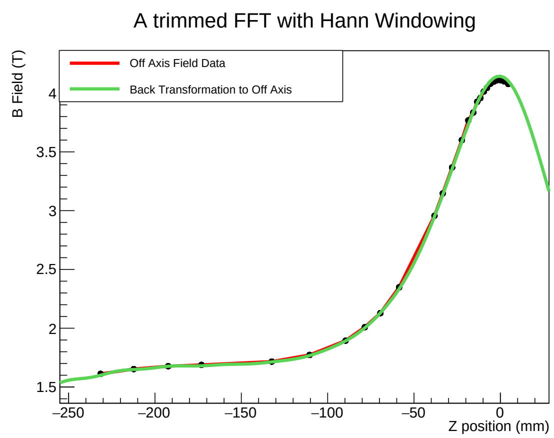

(b)

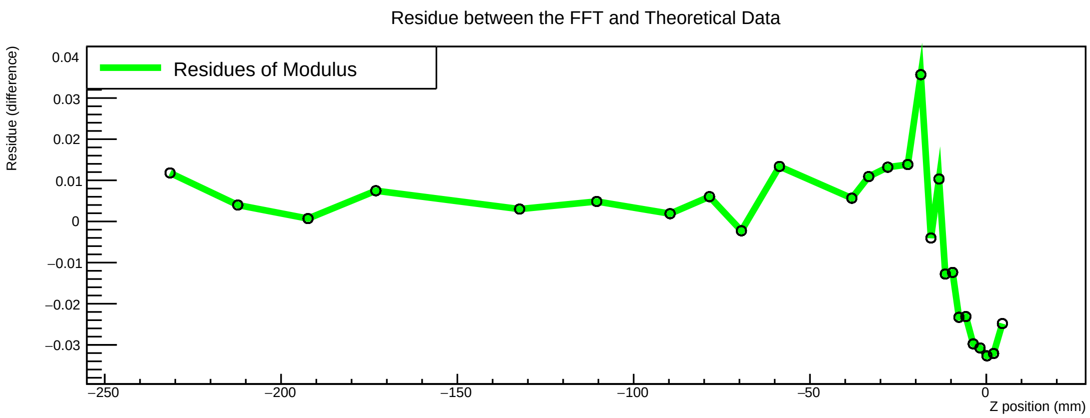

(c)

Figure 5.6: a) Direct comparison of FFT and off-axis data. b) The on-axis data is shifted by 8 mm in z before performing the FFT. c) Residues between the shifted FFT and the off-axis data.

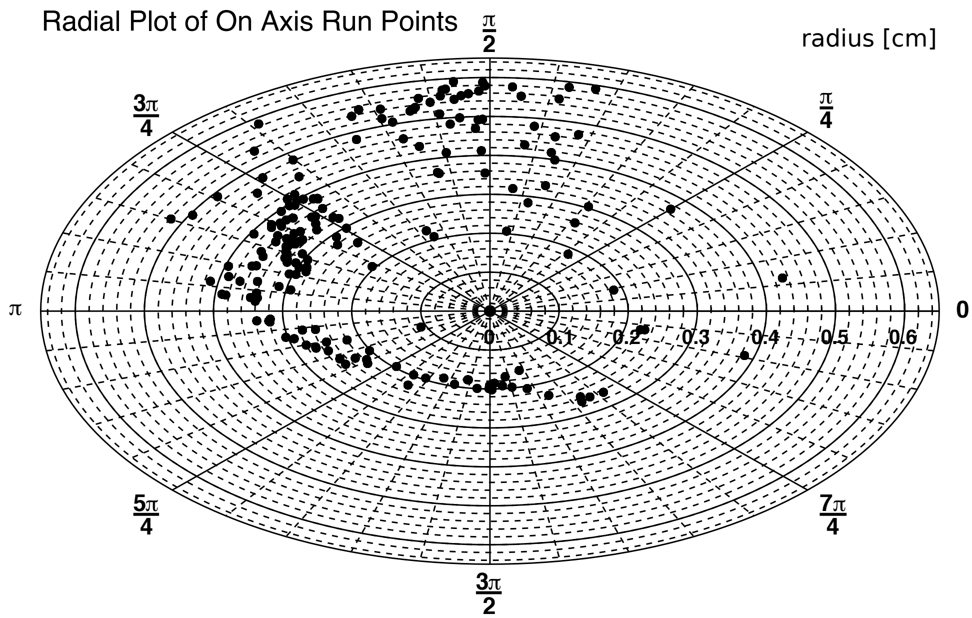

Figure 5.7: A polar plot of the on-axis run positions in the coordinate frame of the inserted dewar, in centimeters and radians. It can be seen that the hanging trolley diverges from the main axis by a maximum of 0.6 cm.

and are not contained to a single radius. Furthermore, the dewar axis is not necessarily aligned with the symmetry axis of the magnetic field; as the magnet cools to superconducting temperatures, the coils will contract and move within the vacuum casing. The data taken in the frame of the dewar axis must be corrected to the true magnetic axis frame in order to provide a true expansion.

To determine the magnetic axis, the off-axis data are fit to a version of the modified Bessel expansion, for example by taking a single off-axis ϕ scan, as described in chapter 4. This type of scan has a small change in z as it rotates in ϕ. Following the reasoning of subsection 5.1.1, a filter coil length of 28.7 mm, a variation of 2 mm in z, and a 1% error would require $n \geq \frac{2}{.01(28.7)} \approx 7$ wavenumbers to describe the field.

The fit function for the data can be described as

$$B_{mod}(z) = \sqrt{B_z^2 + B_\rho^2} \tag{5.31}$$

$$B_z(z) = \sum_{n=0}^{N} I_0(2\pi n\rho/L)\Big[C[n]\cos(2\pi nz/L) - D[n]\sin(2\pi nz/L)\Big] \tag{5.32}$$

$$B_\rho(z) = \sum_{n=0}^{N} I_1(2\pi n\rho/L)\Big[C[n]\sin(2\pi nz/L) + D[n]\cos(2\pi nz/L)\Big] \tag{5.33}$$

and has $2N$ fit parameters, if setting the length L to be a parameter. If an offset is allowed in the fit function, the radius can be written as

$$\rho = \sqrt{\rho'^2 + 2x'\delta x + 2y'\delta y + \delta x^2 + \delta y^2} \tag{5.34}$$

where $x' = x - \delta x$ and $y' = y - \delta y$ are the coordinates of the true magnetic axis, and $(\delta x, \delta y)$ are fit parameters. This brings the total number of fit parameters to $2n + 2$.

The precision of this fit can be tested by using theoretically generated data. If a false offset of (1.00,-2.00) mm is given, the generated data looks like Figure 5.8a and Figure 5.8b. Performing a fit of $n = 7$ wavenumbers, the offsets are found to be $\delta x = 1.01 \pm 0.27$ mm and $\delta y = -2.00 \pm 0.22$ mm. As can be seen in Figure 5.8c, the fit itself is correct within 10^{-3}.

This fit can be demonstrated on a single ϕ scan of data, shown in Figure 5.9. This is a fit of a scan taken at $z = 13 \pm 2$ mm. This fit gives the offsets as $\delta x = -1.86 \pm .07$ mm and $\delta y = 1.05 \pm 0.07$ mm. As a check, an independent fit using the radial series expansion gave an offset of $\delta x = -2.10 \pm 0.30$ mm and $\delta y = 1.20 \pm 0.20$ mm, as seen in Figure 5.10. These two methods give the same offset within error, indicating that there is indeed an offset of about (-2,1) mm between the magnetic field axis and the dewar frame axis at $z \approx 13$ mm.

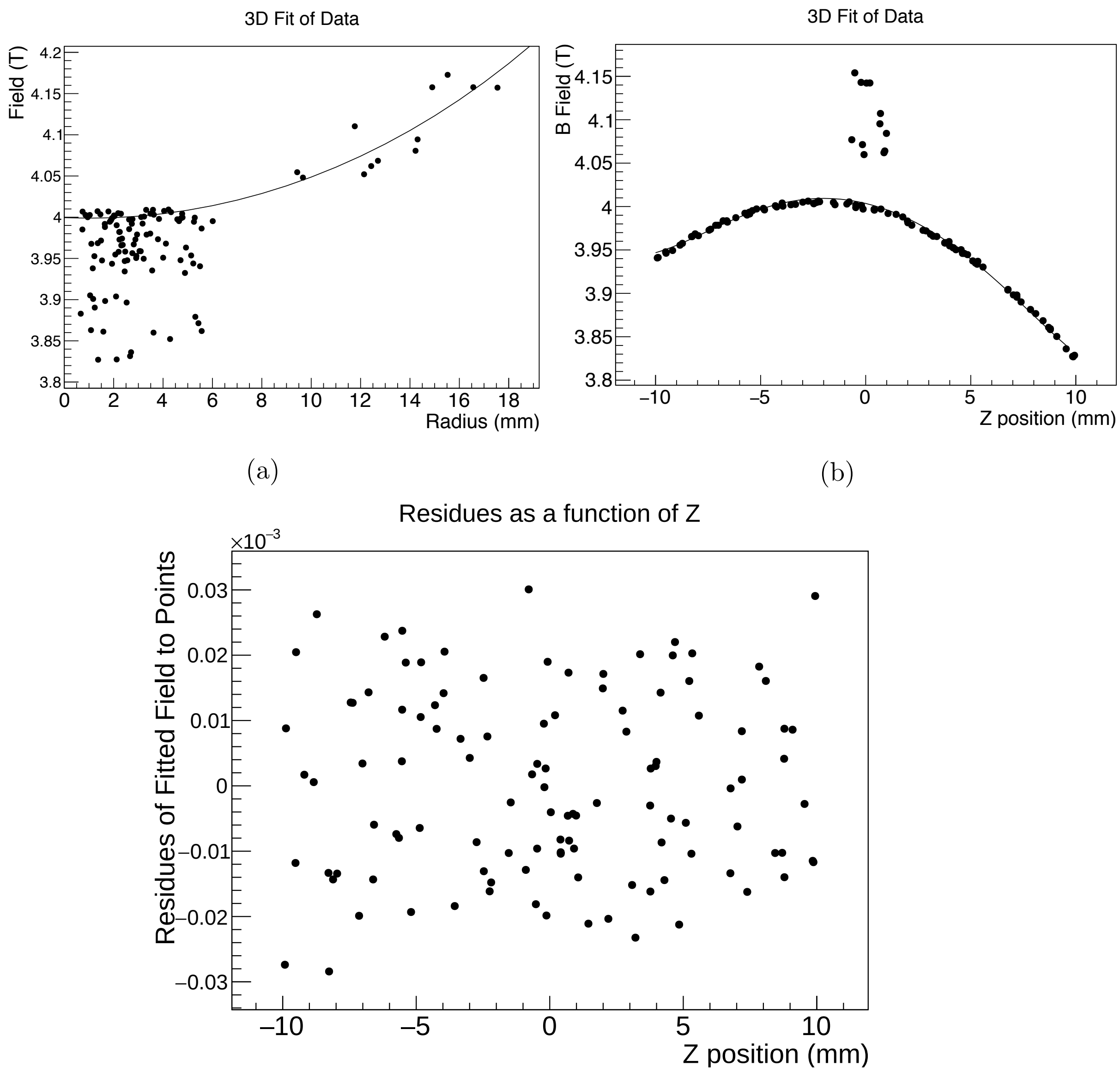

Figure 5.8: a) A generated set of data from a ϕ scan with 2.00 mm variation in r and z, and an offset of (1.00,-2.00) mm. b) Residues between the fake ϕ scan data and the fit.

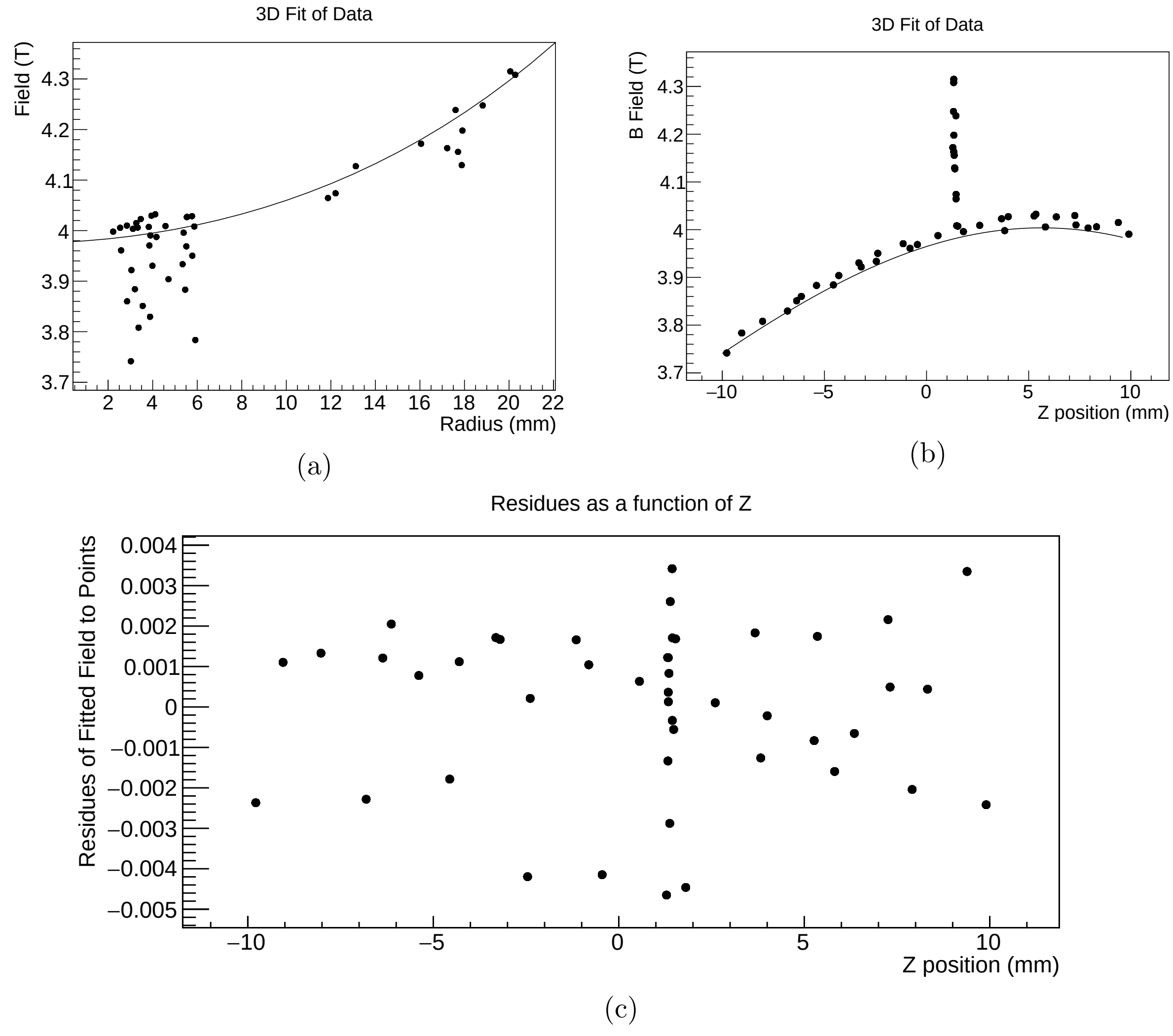

Figure 5.9: a) A fit of the ϕ scan at $z = 13 \pm 2$ mm and the on axis data, giving an offset of $(-1.86 \pm 0.07,\, 1.05 \pm 0.07)$ mm. b) Residues between the ϕ scan data and the fit.

Another modified Bessel function fit can be performed using the data taken in the region near the upper detector (approximately 5 meters above the filter peak in the field). This region is preferable because the data has similar behavior to the filter region, with a peak in the magnetic field. The fit of this data can be seen in Figure 5.11, giving an offset of $\delta x = 0.30 \pm 1.79\,\mathrm{mm}$ and $\delta y = -2.67 \pm 2.17\,\mathrm{mm}$. Though the fit itself converges, the error on the offset parameters is much too large to make any physical sense. This is likely because the quality and amount of data taken in this region was much less than that of the filter region.

In short, fitting the field to a modified Bessel function is sufficient to both find the magnetic field axis and perform an expansion of the field using an FFT of the data on-axis, but the mapping data taken needs to augmented. The current data allows an expansion good to 10^{-2} in the filter region, but all the data must be corrected to the magnetic field axis frame. The data shows that the axis has shifted by (-2,1) mm in the filter region, but is not sufficient to determine the zenithal tilt. A second, more detailed mapping of the magnetic field should be taken.

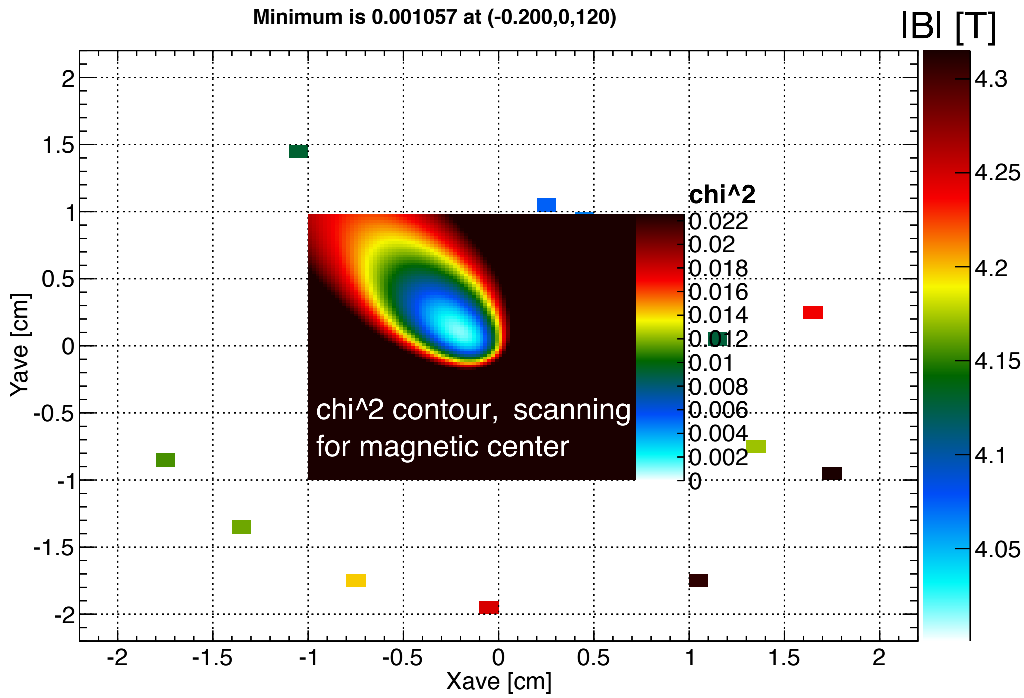

(a)

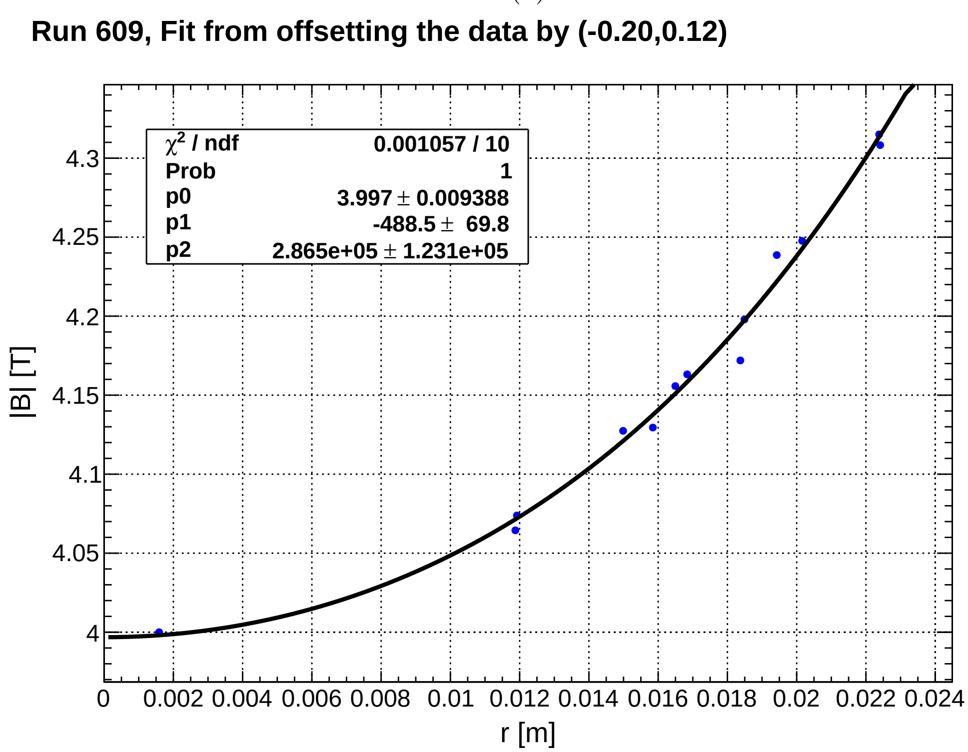

(b)

Figure 5.10: An independent radial series fit of the same ϕ scan. This found an offset of $\delta x = -2.0 \pm 0.3\,\mathrm{mm}$ and $\delta y = 1.2 \pm 0.2\,\mathrm{mm}$. Courtesy of J. Fry

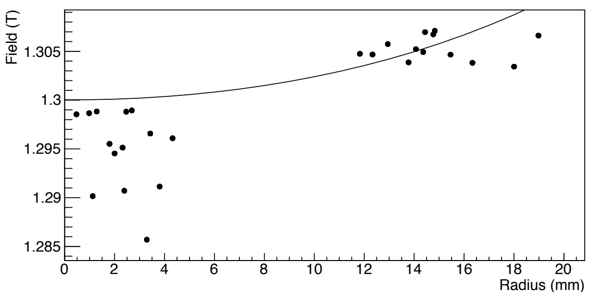

(a)

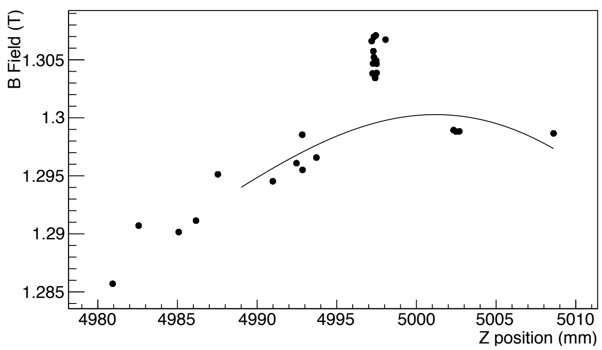

(b)

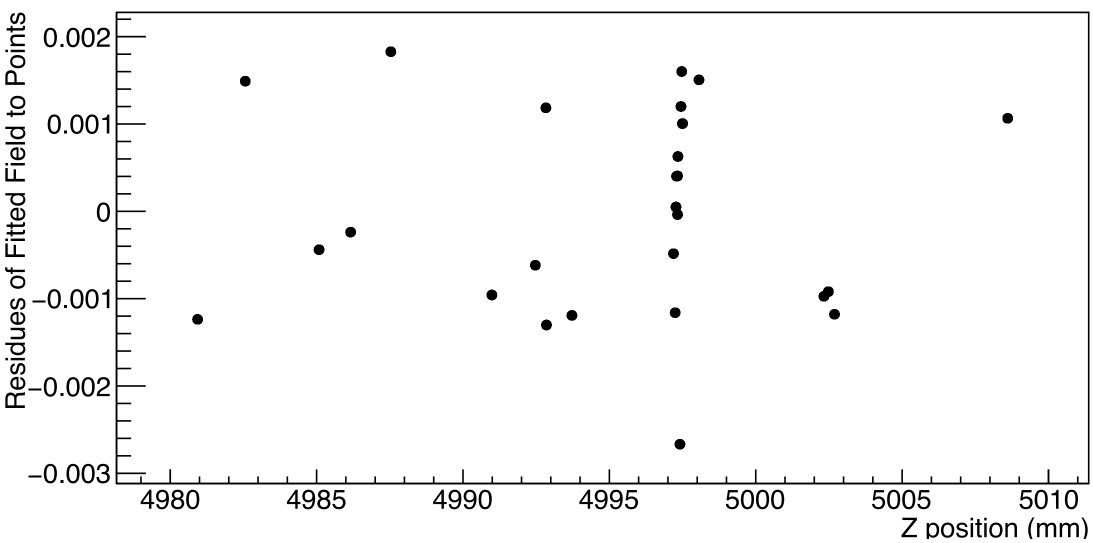

(c)

Figure 5.11: a) A fit of the ϕ scan at $z = 4998 \pm 2$ mm and the on axis data, giving an offset of $(0.30 \pm 1.79, -2.67 \pm 2.17)$ mm. b) Residues between the ϕ scan data and the fit..

Chapter 6

Conclusion

In summary, Nab aims to measure the electron-antineutrino correlation parameter, a, to a relative uncertainty of 10^{-3}. This measurement will give an independent and competitive determination of $\lambda = G_A/G_V$, the ratio of the axial-vector to vector coupling constants present in weak interactions. As can be seen in Equation 6.1, this measurement coupled with a measurement of the neutron lifetime allows for an extraction of V_{ud}, the up-down matrix element of the Cabibbo-Kobayashi-Maskawa matrix. This is an independent determination of V_{ud}, free of the radiative corrections present in nuclear beta decays.

$$\Gamma = \frac{1}{\tau_n} = \frac{f^R m_e^5 c^4}{2\pi^3 \hbar^7} |V_{ud}|^2 G_F^2 \big(1 + 3|\lambda|^2\big) \tag{6.1}$$

The parameter a is the correlation strength of the opening angle between the electron and antineutrino, see Equation 6.2. This angle is extracted using conservation of momentum and measuring the electron energy and proton momentum spectra. As can be seen in

Equation 6.3, the parameter a can be extracted from the slope of the p_p^2 spectrum at constant E_e.

$$\Gamma = f(E_e)\left[1 + a\frac{\vec{p_e} \cdot \vec{p_\nu}}{E_e E_\nu}\right] = f(E_e)\left[1 + a\beta_e cos\theta_{e\nu}\right] \tag{6.2}$$

$$P_p(p_p^2) = \begin{cases} 1 + a\beta_e \frac{p_p^2 + p_e^2 + p_\nu^2}{2p_e p_\nu} & for \left|\frac{p_p^2 + p_e^2 + p_\nu^2}{2p_e p_\nu}\right| < 1 \\ 0 & \text{otherwise} \end{cases} \tag{6.3}$$

Due to the low endpoint energy of the proton spectrum, proton energy detection is traditionally the largest source of systematic uncertainty in neutron beta decay correlation measurements. Nab mitigates this by using a novel spectrometer to convert the proton momentum into a time of flight measurement. Since a is theoretically extracted from the slope of the p_p^2 yield spectrum, the observed spectrum must be the square of the inverse time of flight, $1/t_p^2$. The observed $1/t_p^2$ depends on the magnetic field of the spectrometer as

$$t_p^2 = \frac{m_p^2}{p_0^2}\left[\int \frac{dl}{\sqrt{1 - \frac{e(V(l) - V_0)}{T_0} - \frac{B(l)}{B_0}\sin^2\theta_0}}\right]^2 \tag{6.4}$$

Since the observed data is the spectrum of $1/t_p^2$, the response function must be known within 10^{-3} relative uncertainty in order to sufficiently correct for the effects of the spectrometer. To achieve this, the magnetic field has been mapped to a 10^{-3} uncertainty using a transverse Hall probe and two laser trackers. However, since this mapping cannot cover all regions of the proton flight path, the data must be fit to some expansion of the field.

This work explores one such expansion in terms of modified Bessel functions, which are naturally cylindrically symmetric basis functions. In this method, the off axis fields can be written as

$$B_z(\rho, z) = \sum_{k=-\infty}^{\infty} I_0(k\rho) F_k e^{ikz} \tag{6.5}$$

$$B_\rho(\rho, z) = \sum_{k=-\infty}^{\infty} -iI_1(k\rho) F_k e^{ikz} \tag{6.6}$$

where F_k are the Fourier coefficients found by transforming the on axis field,

$$F_k = \int_L B_z(\rho = 0, z) e^{-ikz} dz \tag{6.7}$$

This dissertation has investigated the effectiveness of the modified Bessel function expansion. As discussed in chapter 5, the expansion is sufficient for small radii ($\approx 20\,\text{mm}$) to 10^{-4}. When used over mapping data, it becomes clear that there is a discrepancy between the data frame of reference and the cylindrically symmetric frame. The data must be corrected to this *magnetic axis frame* and a true "on axis" field must be found before applying the Fourier transform.

There is now an ongoing effort to correct to the magnetic axis frame. This is done by fitting a two dimensional slice of data to a modified Bessel function expansion. This fit can determine an offset of the magnetic axis within 0.2 mm when tested with generated field data. A fit of the field using the modified bessel function expansion gives an offset of $(-1.86 \pm 0.07,\ 1.05 \pm 0.07)$ mm, which agrees with an independent fit of the same data using the radial series expansion. However, this only gives a single data point for how the axis has shifted. At least one more offset must be determined to understand the zenithal tilt of the magnetic field. A second fit of data taken at the peak of the upper detector field results in an offset of $(0.30 \pm 1.79,\ -2.67 \pm 2.17)$ mm. This error of this result makes this offset physically meaningless. A second mapping of the upper detector will provide better data such that the offset can be found.

In summary, the modified Bessel function expansion of the on axis data agrees with the off axis data within 10^{-2}, as shown in Figure 5.6, when the magnetic field axis is tilted with respect to the dewar axis. When the magnetic field data is finished being fitted to a cylindrically symmetric frame of reference, this expansion method will allow a full determination of the magnetic field throughout the proton flight path, a calculation of the spectrometer response function to 10^{-3} relative uncertainty, and a final uncertainty in a on the order of 10^{-3}.

Bibliography

Bibliography

[1] R. Alarcon, L. Alonzi, S. Baeßler, S. Balascuta, J. Bowman, M. Bychkov, J. Byrne, J. Calarco, T. Cianciolo, C. Crawford, E. Frlez, M. Gericke, F. Glück, G. Greene, R. Grzywacz, V. Gudkov, F. Hersman, A. Klein, M. Lehman, J. Martin, S. McGovern, S. Page, A. Palladino, S. Penttilä, D. Počanić, K. Rykaczewski, W. Wilburn, and A. Young. Precise Measurement of $\lambda = G_v/G_a$ and Search for Non- V-A Weak Interaction Terms in Neutron Decay. *Proposal*, 2010. xiii, 22

[2] M. Aleksa, F. Bergsma, P. A. Giudici, A. Kehrli, M. Losasso, X. Pons, H. Sandaker, P. S. Miyagawa, S. W. Snow, J. C. Hart, and L. Chevalier. Measurement of the ATLAS solenoid magnetic field. *Journal of Instrumentation*, 3(04):P04003–P04003, April 2008.

[3] M. Bargiotti et al. Present knowledge of the Cabibbo-Kobayashi-Maskawa matrix. *Riv. Nuovo Cim.*, 23N3:1, 2000. 7

[4] L. J. Broussard, R. Alarcon, S. Baeßler, L. Barrón Palos, N. Birge, T. Bode, J. D. Bowman, T. Brunst, J. R. Calarco, J. Caylor, T. Chupp, V. Cianciolo, C. Crawford, G. W. Dodson, J. DuBois, W. Fan, W. Farrar, N. Fomin, E. Frlez, J. Fry, M. T. Gericke, F. Glück, G. L. Greene, R. K. Grzywacz, V. Gudkov, C. Hendrus, F. W. Hersman, T. Ito, H. Li, N. Macsai, M. F. Makela, J. Mammei, R. Mammei, J. Martin,

M. Martinez, P. L. McGaughey, S. Mertens, J. Mirabal-Martinez, P. Mueller, S. A. Page, S. I. Penttilä, R. Picker, B. Plaster, D. Počanić, D. C. Radford, J. Ramsey, K. P. Rykaczewski, A. Salas-Bacci, E. M. Scott, S. K. L. Sjue, A. Smith, E. Smith, A. Sprow, E. Stevens, J. Wexler, R. Whitehead, W. S. Wilburn, A. R. Young, and B. A. Zeck. Neutron decay correlations in the Nab experiment. *J. Phys.: Conf. Ser.*, 2017.

[5] L. J. Broussard, B. A. Zeck, E. R. Adamek, S. Baeßler, N. Birge, M. Blatnik, J. D. Bowman, A. E. Brandt, M. Brown, J. Burkhart, N. B. Callahan, S. M. Clayton, C. Crawford, C. Cude-Woods, S. Currie, E. B. Dees, X. Ding, N. Fomin, E. Frlez, J. Fry, F. E. Gray, S. Hasan, K. P. Hickerson, J. Hoagland, A. T. Holley, T. M. Ito, A. Klein, H. Li, C. Y. Liu, M. F. Makela, P. L. McGaughey, J. Mirabal-Martinez, C. L. Morris, J. D. Ortiz, R. W. Pattie Jr, S. I. Penttilä, B. Plaster, J. C. Ramsey, A. Salas-Bacci, D. J. Salvat, A. Saunders, S. J. Seestrom, S. K. L. Sjue, A. P. Sprow, Z. Tang, R. B. Vogelaar, B. Vorndick, Z. Wang, W. Wei, J. Wexler, W. S. Wilburn, T. L. Womack, and A. R. Young. Detection System for Neutron β Decay Correlations in the UCNB and Nab experiments. *arXiv*, 2016. xiv, 27

[6] M. A. P. Brown, E. B. Dees, E. Adamek, B. Allgeier, M. Blatnik, T. J. Bowles, L. J. Broussard, R. Carr, S. Clayton, C. Cude-Woods, S. Currie, X. Ding, B. W. Filippone, A. Garcia, P. Geltenbort, S. Hasan, K. P. Hickerson, J. Hoagland, R. Hong, G. E. Hogan, A. T. Holley, T. M. Ito, A. Knecht, C. Y. Liu, J. Liu, M. Makela, J. W. Martin, D. Melconian, M. P. Mendenhall, S. D. Moore, C. L. Morris, S. Nepal, N. Nouri, J. R W Pattie, A. P. Galván, I. I. D G Phillips, R. Picker, M. L. Pitt, B. Plaster, J. C. Ramsey, R. Rios, D. J. Salvat, A. Saunders, W. Sondheim, S. J. Seestrom, S. Sjue,

S. Slutsky, X. Sun, C. Swank, G. Swift, E. Tatar, R. B. Vogelaar, B. Vorndick, Z. Wang, J. Wexler, T. Womack, C. Wrede, A. R. Young, and B. A. Zeck. New result for the neutron β-asymmetry parameter A_0 from UCNA. *Phys. Rev. C*, 2018. xii, 12, 13

[7] J. Chadwick and M. Goldhaber. A nuclear photo-effect - disintegration of the diplon by gamma rays. *Nature*, 134:237–238, 1934. 2

[8] J. Chadwick and M. Goldhaber. The nuclear photoelectric effect. *Proceedings of the Royal Society of London. Series A, Mathematical and Physical Sciences*, 151(873):479–493, 1935. 2

[9] V. Cirgiliano, A. Garcia, D. Gazit, O. Naviliat-Cuncic, G. Savard, and A. Young. Precision Beta Decay as a Probe of New Physics. *arXiv*, 2019.

[10] A. Czarnecki, W. J. Marciano, and A. Sirlin. Pion Beta Decay and CKM Unitarity. 2019.

[11] A. Czarnecki, W. J. Marciano, and A. Sirlin. Radiative corrections to neutron and nuclear beta decays revisited. *Phys. Rev. D*, 100:073008, Oct 2019.

[12] A. Das. V-Atheory: A view from the outside. *J. Phys.: Conf. Ser.*, 2009.

[13] E. D.B. Pelowitz. Mcnpx users manual version 2.7.0. LA-CP-11-00438, 2011. 40

[14] P. Duhamel and M. Vetterli. Fast fourier transforms: A tutorial review and a state of the art. *Signal Processing*, 1990.

[15] N. Fomin, G. Greene, R. Allen, V. Cianciolo, C. Crawford, T. Tito, P. Huffman, E. Iverson, R. Mahurin, and W. Snow. Fundamental neutron physics beamline at the

spallation neutron source at ornl. *Nuclear Instruments and Methods in Physics Research Section A: Accelerators, Spectrometers, Detectors and Associated Equipment*, 773:45 – 51, 2015. xiv, 42, 43, 44

[16] H. Frauenfelder, R. Bobone, E. Von Goeler, N. Levine, H. R. Lewis, R. N. Peacock, A. Rossi, and G. De Pasquali. Parity and the Polarization of Electrons from Co60. *Phys. Rev. C*, 1957. 5

[17] M. Goldhaber, L. Grodzins, and A. W. Sunyar. Helicity of Neutrinos. *Phys. Rev. C*, 1958. 6

[18] J. E. Gomez-Correa, S. E. Balderas-Mata, V. Coello, N. P. Puente, J. Rogel-Salazar, and S. Chavez-Cerda. On the physics of propagating Bessel modes in cylindrical waveguides. *arXiv*, 2016.

[19] K. B. Grammer, R. Alarcon, L. Barrón Palos, D. Blyth, J. D. Bowman, J. Calarco, C. Crawford, K. Craycraft, D. Evans, N. Fomin, J. Fry, M. Gericke, R. C. Gillis, G. L. Greene, J. Hamblen, C. Hayes, S. Kucuker, R. Mahurin, M. Maldonado-Velázquez, E. Martin, M. McCrea, P. E. Mueller, M. Musgrave, H. Nann, S. I. Penttilä, W. M. Snow, Z. Tang, and W. S. Wilburn. Measurement of the scattering cross section of slow neutrons on liquid parahydrogen from neutron transmission. *Phys. Rev. B*, 2015.

[20] K. B. Grammer and J. D. Bowman. Monte Carlo calculation of the average neutron depolarization for the NPDGamma experiment. *Nuclear Inst. and Methods in Physics Research, A*, 2019.

[21] J. C. Hardy and I. S. Towner. Nuclear beta decays and CKM unitarity. *arXiv*, 2018. xii, 8, 11

[22] A. T. Holley, L. J. Broussard, J. L. Davis, K. Hickerson, T. M. Ito, C. Y. Liu, J. T. M. Lyles, M. Makela, R. R. Mammei, M. P. Mendenhall, C. L. Morris, R. Mortensen, R. W. Pattie, R. Rios, A. Saunders, and A. R. Young. A high-field adiabatic fast passage ultracold neutron spin flipper for the UCNA experiment. *Review of Scientific Instruments*, 2012.

[23] R. Hong, M. G. Sternberg, and A. Garcia. Helicity and nuclear β decay correlations. *Am. J. Phys.*, 2017.

[24] J. D. Jackson, S. B. Treiman, and H. W. Wyld. Possible Tests of Time Reversal Invariance in Beta Decay. *Phys. Rev. C*, 1957. 9, 19

[25] K. Kim. Neutrino and Parity Violation in Weak Interaction. *arXiv*, 1998.

[26] L. E. Kirsch, M. Devlin, S. M. Mosby, and J. A. Gomez. A New Measurement of the 6Li(n,α)t Cross Section at MeV Energies Using a Fission Chamber and 6Li Scintillators. *arXiv*, 2017.

[27] Y. Kuno and Y. Okada. Muon Decay and Physics Beyond the Standard Model. *arXiv*, 1999.

[28] T. D. Lee and C. N. Yang. Parity Nonconservation and a Two-Component Theory of the Neutrino. *Phys. Rev. C*, 1957. 2

[29] K. Lefmann and K. Nielsen. Mcstas, a general software package for neutron ray-tracing simulations. *Neutron News*, 10(3):20–23, 1999. 40

[30] L. Maiani. Universality of the Weak Interactions, Cabibbo theory and where they led us. *Riv. Nuovo Cim.*, 34:679–692, 2011.

[31] R. Maisonobe et al. Electron-antineutrino angular correlation coefficient a measurement in neutron beta-decay with the spectrometer aSPECT. *PoS*, EPS-HEP2015:595, 2015. xiii, 16, 17

[32] W. J. Marciano and A. Sirlin. Improved calculation of electroweak radiative corrections and the value of V_{ud}. *Phys. Rev. Lett.*, 96:032002, Jan 2006. 12

[33] E. Marsch. On Charge Conjugation, Chirality and Helicity of the Dirac and Majorana Equation for Massive Leptons. *Symmetry*, 2015.

[34] R. Munoz Horta. *First measurements of the aSPECT spectrometer*. PhD thesis, Mainz U., Inst. Phys., 2011.

[35] V. Nesvizhevsky and J. Villain. The discovery of the neutron and its consequences (1930–1940). *Comptes Rendus Physique*, 2018.

[36] J. S. Nico. Neutron beta decay. *J. Phys. G: Nucl. Part. Phys.*, 2009. xii, 11, 18

[37] W. Pauli. Dear Radioactive Ladies and Gentlemen. 1930. 2

[38] B. Plaster, E. Adamek, B. Allgeier, J. Anaya, H. O. Back, Y. Bagdasarova, D. B. Berguno, M. Blatnik, J. G. Boissevain, T. J. Bowles, L. J. Broussard, M. A. P. Brown, R. Carr, D. J. Clark, S. Clayton, C. Cude-Woods, S. Currie, E. B. Dees, X. Ding, S. Du,

B. W. Filippone, A. Garcia, P. Geltenbort, S. Hasan, A. Hawari, K. P. Hickerson, R. Hill, M. Hino, J. Hoagland, S. A. Hoedl, G. E. Hogan, B. Hona, R. Hong, A. T. Holley, T. M. Ito, T. Kawai, K. Kirch, S. Kitagaki, A. Knecht, S. K. Lamoreaux, C. Y. Liu, J. Liu, M. Makela, R. R. Mammei, J. W. Martin, N. Meier, D. Melconian, M. P. Mendenhall, S. D. Moore, C. L. Morris, R. Mortensen, S. Nepal, N. Nouri, R. W. Pattie, A. P. Galván, D. G. Phillips, A. Pichlmaier, R. Picker, M. L. Pitt, J. C. Ramsey, R. Rios, R. Russell, K. Sabourov, A. L. Sallaska, D. J. Salvat, A. Saunders, R. Schmid, S. J. Seestrom, C. Servicky, E. I. Sharapov, S. K. L. Sjue, S. Slutsky, D. Smith, W. E. Sondheim, X. Sun, C. Swank, G. Swift, E. Tatar, W. Teasdale, C. Terai, B. Tipton, M. Utsuro, R. B. Vogelaar, B. Vorndick, Z. Wang, B. Wehring, J. Wexler, T. Womack, C. Wrede, Y. P. Xu, H. Yan, A. R. Young, J. Yuan, and B. A. Zeck. Final results for the neutron β-asymmetry parameter A_0 from the UCNA experiment. *arXiv*, 2019. xii, 12, 13

[39] G. Rajasekaran. Fermi and the Theory of Weak Interactions. *arXiv*, 2014. 2

[40] J. Robson. The radioactive decay of the neutron. *Phys. Rev. Lett.*, 1951. 3

[41] E. Rutherford. Nuclear Constitution of Atoms1. 1920. 1

[42] V. Santoro, D. D. DiJulio, and P. M. Bentley. MeV Neutron Production from Thermal Neutron Capture in 6Li Simulated With Geant4. *J. Phys.: Conf. Ser.*, 2016.

[43] V. Santoro, D. D. DiJulio, and P. M. Bentley. MeV Neutron Production from Thermal Neutron Capture in 6Li Simulated With Geant4. *J. Phys.: Conf. Ser.*, 2016.

[44] H. Saul, C. Roick, H. Abele, H. Mest, M. Klopf, A. Petukhov, T. Soldner, X. Wang, D. Werder, and B. Märkisch. Limit on the Fierz Interference Term b from a Measurement of the Beta Asymmetry in Neutron Decay. 2019.

[45] C.-Y. Seng, M. Gorchtein, and M. J. Ramsey-Musolf. Dispersive evaluation of the inner radiative correction in neutron and nuclear β decay. *Phys. Rev. D*, 100:013001, Jul 2019. xiii, 12, 14

[46] A. Snell and L. Miller. On the Decay of the Neutron. *Phys. Rev.*, 74(1217), 1948. 3

[47] M. Tanabashi et al. Review of Particle Physics. *Phys. Rev.*, D98(3):030001, 2018. xiii, 14, 15

[48] A. A. Taskin, H. F. Legg, F. Yang, S. Sasaki, Y. Kanai, K. Matsumoto, A. Rosch, and Y. Ando. Planar Hall effect from the surface of topological insulators. *arXiv*, 2017.

[49] B. Turck. Measurements in an inhomogeneous field with a rectangular hall plate: Errors introduced by size effects on the perpendicular component. *Nuclear Instruments and Methods*, 1971. xvi, 64

[50] T. G. Walker. Fundamentals of Spin-Exchange Optical Pumping. *J. Phys.: Conf. Ser.*, 2011.

[51] H. Wenninger, J. Stiewe, and H. Leutz. The 22na positon spectrum. *Nuclear Physics A*, 109(3):561 – 576, 1968. 19

[52] P. Wiacek, M. Chudyba, T. Fiutowski, and W. Dabrowski. Limitations on energy resolution of segmented silicon detectors. *Journal of Instrumentation*, 13(04):P04003–P04003, Apr 2018.

[53] F. E. Wietfeldt, W. A. Byron, G. Darius, C. R. DeAngelis, M. T. Hassan, M. S. Dewey, M. P. Mendenhall, J. S. Nico, B. Collett, G. L. Jones, A. Komives, and E. J. Stephenson. Measurement of the electron-antineutrino correlation in neutron beta decay: aCORN experiment. *arXiv*, 2018. xiii, 17, 18, 23

[54] F. E. Wietfeldt and G. L. Greene. Colloquium: The neutron lifetime. *Rev. Mod. Phys.*, 2011. 3

[55] P. Willendrup, E. Farhi, E. Knudsen, U. Filges, K. Lefmann, R. Dtu, and R. Denmark. Mcstas: Past, present and future. *Journal of Neutron Research*, 17, 04 2013. 40

[56] P. Willendrup, E. Farhi, and K. Lefmann. Mcstas 1.7 - a new version of the flexible monte carlo neutron scattering package. volume 350, pages e735–e737. Elsevier, 2004. 40

[57] P. Willendrup and K. Lefmann. Mcstas (i): Introduction, use, and basic principles for ray-tracing simulations. *Journal of Neutron Research*, pages 1–16, 06 2019. 40

[58] F. L. Wilson. Fermi's Theory of Beta Decay. *Am. J. Phys.*, 1968. 2

[59] A. G. Wunderle. *Precision measurement of the* β *-* $\bar{\nu}_e$ *angular correlation coefficient a in free neutron decay.* PhD thesis, Mainz U., 2017.

[60] P. Žugec, D. Bosnar, N. Colonna, and F. Gunsing. An improved method for estimating the neutron background in measurements of neutron capture reactions. *Nucl. Instrum. Meth.*, A826:80–89, 2016.

Vita

Elizabeth Mae Scott was born in Low Moore, Virginia in 1991. She graduated with the class of 2009 from Greenbrier East High School in Lewisburg, West Virginia and subsequently attended Tulane University in New Orleans, Louisiana. In 2013, she graduated *summa cum laude* with a Bachelor of Science in Mathematics and Physics with a minor in Spanish. The following fall, she joined the Department of Physics and Astronomy at the University of Tennessee, Knoxville and began her work on her doctorate.